

Infragravity Wave Motions in the Scheldt Region

Teun Grandiek

Delft University of Technology, Rijkswaterstaat

Infragravity Wave Motions in the Scheldt Region

Student Name	Student number
Teun Grandiek	4564588

Supervisors: Dr. Ir. A.J.H.M. Reniers (Chair, Daily supervisor) Technical University Delft
Dr. M.F.S. Tissier Technical University Delft
Dr. Ir. B. Hofland Technical University Delft
Ir. G. Akrish Technical University Delft
Ir. R. Slomp (Daily supervisor) Rijkswaterstaat

Cover: Copernicus Sentinel data (2020), processed by ESA, CC BY-SA
3.0 IGO (Adapted)

Style: TU Delft Report Style, with modifications by Daan Zwaneveld



Rijkswaterstaat
Ministerie van Infrastructuur en Milieu

Abstract

This study focuses on the infragravity (IG) waves at 5 measurement sites (Brouwershavense Gat 2 (BG2), Oosterschelde 4 (OS4), Cadzand, Hansweert and Bath) in the Scheldt region, examining their characteristics in these waters as well as to what extent they can be modelled using SWAN (Simulating WAVes Nearshore). To facilitate this, data collected during the occurrence of four storms (Corrie, Dudley, Eunice and Franklin) that traversed the North Sea in January and February 2022 has been used.

A spectral analysis has been used to provide insight into the IG and sea-swell (SS) wave field. To this extent, H_{m0} for the IG (0.005 Hz to 0.04 Hz) and SS (0.04 Hz to 0.33 Hz) frequency bands have been derived, in addition to the storm averaged wave period (T_{m-10}). Measurement device BG2 documented the largest storm averaged $H_{m0,IG}$ and $H_{m0,SS}$ values (0.256 m and 3.46 m during storm Corrie, respectively). The measurement device with the smallest storm averaged H_{m0} values was Hansweert, which measured 0.024 m and 0.217 m for the IG and SS wave frequencies, also during storm Corrie. Most of the wave energy for the measurement devices in the Western Scheldt, Hansweert and Bath, can be attributed to waves with frequency values larger than the upper boundary for SS waves ($T < 3$ s). The fraction of the total wave energy contained within the IG and SS frequency bands ranged from 0.1 to 0.56 for these two measurement devices. Conversely, the IG and SS frequency bands contain 0.81 to 0.96 of the total wave energy for measurement device Cadzand, BG2 and OS4. The correlation between $H_{m0,SS}$ and $H_{m0,IG}$ is mostly strong for the BG2, OS4 and Cadzand measurement devices (0.657 to 0.956) and generally moderate for Hansweert and Bath (0.474 to 0.87, with one outlier equivalent to 0.128). A bispectral analysis was used to offer more insight regarding the components contributing to the total IG wave field. The results at Bath proved to be erroneous for all storms except Corrie, as the derived free IG (FIG) contribution was negative. The origin remains unclear, although it appears to be related to unexplained spurious bursts in the wave elevation signal. The bispectral analysis for the remainder of the locations lead to maximum TIG wave heights ranging from 0.05 m to 0.12 m for Hansweert, 0.15 m to 0.39 m for BG2, 0.11 m to 0.35 m for OS4 and 0.21 m to 0.34 m for Cadzand for the 4 storms. The contribution of the bound IG (BIG) and FIG energy at Bath and Hansweert appears to fluctuate heavily, undergoing rapid changes on an hourly basis. For BG2, OS4 and Cadzand, the FIG energy contribution is strongly dominant as it generally amounted to > 0.75 of the TIG energy.

The capabilities of the SWAN model were evaluated by simulating FIG waves in the North Sea basin. The model relates incident SS wave energy to reflected FIG wave energy with FIG source lines based on the reflection parametrization of [Ardhuin, Rawat, and Aucan \(2014\)](#). The hourly SS wave inputs, H_{m0} and T_{m-10} , were provided by [European Union-Copernicus Marine Service \(2019\)](#). The predictive skill was used to qualitatively assess to what extent the model is able to reproduce FIG waves in the Scheldt region. The model was unable to correctly predict the FIG waves Hansweert and Bath, where the predictive skill values for all storms ranged from 0.0003 to 0.0009 for Hansweert, and were 0 for Bath. Better predictive skill values were obtained for BG2 (0.5044 to 0.6565), OS4 (0.3327 to 0.4293) and Cadzand (0.6466 to 0.7510), but there is still room for improvement. The lacking skill values can be attributed to not enough FIG wave energy being able to penetrate the estuarine waters. Reflective lines were implemented along the coastline of the Western Scheldt in an attempt to force more FIG energy into the estuary. This only led to a minor increase for the predictive skill values ($\mathcal{O}(0.002)$ for Hansweert, 0 for Bath and $\mathcal{O}(0.0001)$ for BG2, OS4 and Cadzand) but from a spatial standpoint, it appears that there are locations in the estuary where the absolute increase was $\mathcal{O}(0.02$ cm), which is significant as there are areas in the estuary where $H_{m0,FIG}$ has doubled as a consequence of the implementation of the reflective lines.

Preface

Before you lies the MSc thesis titled "Infragravity Wave Motions in the Scheldt Region", marking the culmination of my master's degree in Hydraulic Engineering at the Technical University of Delft. The fulfillment of this degree would not have been possible without the help of a variety of people, whom I would like to thank.

First, I would like express my gratitude to my graduation committee from the Technical University of Delft for the time and effort they have put into guiding me through my research endeavors. Special thanks to Ad and Gal. Ad, as my daily supervisor you helped me many times whenever I was unsure about subsequent course of action, or simply with explaining the complex matter required for my research. Gal, I am indebted to you for the numerous times you helped me regarding the modelling aspect of this thesis. Marion and Bas, I am appreciative for the useful feedback during the progress meetings throughout my research.

Additionally, I am indebted to my graduation committee from Rijkswaterstaat. They have provided me with the utilities required to complete this research. In particular the access to raw data, that allowed for the separation of BIG waves was unique until now for these measurement locations. Robert and Robert, thanks for getting me in touch with the right people whenever that was needed, for the constructive feedback whenever requested and for allowing me to discover what it is like on the work floor of an organisation such as Rijkswaterstaat.

Finally, I would like to thank my family, especially my parents and step father for always supporting me. Thanks to my friends from the faculty of Civil Engineering and Geosciences for the many hours spent studying together and unwinding in the off-hours. The latter I also owe to my friends from my hometown, Castricum. I doubt I would have a healthy "work-life" balance without them. Lastly, special thanks to Lotte, for always being there for me.

T. Grandiek
Utrecht, February 2024

Contents

Abstract	i
Preface	ii
1 Introduction	1
1.1 Context	1
1.2 Problem Analysis	1
1.3 Objective	2
1.4 Outline	2
2 Literature Study	3
2.1 Generation of IG waves	3
2.1.1 Bound wave	3
2.1.2 Time-varying breakpoint	4
2.1.3 Bore merging	4
2.1.4 Wind gusts	4
2.2 Dissipation of IG waves	5
2.2.1 IG wave breaking	5
2.2.2 Bottom friction	5
2.3 Energy transfer of SS and IG waves	5
2.4 IG waves in tidal inlets	6
2.5 IG wave energy estimation	8
2.6 FIG wave parametrization	10
3 Methodology	11
3.1 Study area	11
3.1.1 Western Scheldt	11
3.1.2 Eastern Scheldt	12
3.1.3 Site conditions	12
3.2 Data Analysis	12
3.2.1 Measuring Devices	12
3.2.2 Storm Description	13
3.2.3 Storm tracks	14
3.2.4 Measuring Period	15
3.2.5 Data Processing	15
3.2.6 Spectral Analysis	18
3.3 SWAN Modelling	19
3.3.1 SWAN file Setup	19
3.3.2 Computational domain	22
3.3.3 FIG Source Lines	22
4 Results	25
4.1 Spectral analyses results	25
4.1.1 Spectral analysis	25
4.1.2 Bispectral analysis	29
4.1.3 Relative contribution	36
4.2 SWAN results	38
4.2.1 Devices	38
4.2.2 Spatial	40
5 Discussion	44
5.1 Model limitations	44
5.1.1 α_1 value	44

5.1.2	Friction coefficient	44
5.1.3	Reflection lines	44
5.1.4	Other FIG sources	44
5.1.5	Positioning of Cadzand	45
5.2	Measurement limitations	45
5.2.1	Locations of measurement devices	45
5.2.2	Bispectral analysis	45
6	Conclusion	46
6.1	IG wave characteristics in the Scheldt region	46
6.2	FIG wave modelling in the Scheldt region	47
7	Recommendations	48
A	Data selection	50
A.1	Storm selection	50
A.2	Measurement errors	52
A.2.1	Corrie	52
A.2.2	Eunice	54
A.2.3	Franklin	55
B	Default SWAN file	57
C	Number of Iterations	58
D	Grid generation enhancements	59
D.1	Modification of the GSHHS data	59
D.2	Modifications on the EMODnet data	60
E	SWAN Assessment	63
E.1	Default	63
E.2	Comparison of the inclusion and exclusion of the reflective lines (Absolute)	66
F	Western Scheldt Reflection Lines	69
F.1	Corrie	69
F.2	Dudley	70
F.3	Eunice	71
F.4	Franklin	72
	References	73

List of Figures

2.1	Comparison between the IG harmonics energy transfers. The left panel depict a steep beach and the right panel depicts a gently sloping beach (de Bakker, Tissier, & Ruessink, 2016).	6
2.2	$u-h$ plot for $L = 25$ m and $T = 6$ s according to the dispersion relation adjusted for Doppler shift	7
3.1	Villages lost to inundation. Depicted is an estimation of the land border in 1573 (Kuipers et al., 2004)	11
3.2	20-minute averaged H_{m0} values at Cadzand of the 2021-2022 storm season	12
3.3	20-minute averaged H_{m0} values at OS4 of the 2021-2022 storm season	12
3.4	ID values of the measurement devices in the Scheldt region.	13
3.5	Trajectory of storm Corrie, Dudley, Eunice and Franklin	14
3.6	H_S plot during storm Corrie	15
3.7	Water level elevation at 031 during storm Corrie	16
3.8	Water level elevation on 01-02-2022 from 09:00 to 11:00 at 011	16
3.9	Water level elevation on 01-02-2022 from 09:54 to 10:18 at 081	17
3.10	Water level elevation during the 7 th hour of storm Corrie at measurement device 011	17
3.11	FIG source lines configuration surrounding the North Sea basin	23
3.12	Bathymetry Zeeland	23
4.1	Storm averaged variance density spectra at all measurement devices during all storms	26
4.2	$H_{m0,IG}$ and $H_{m0,SS}$ at each measurement device during all storms	28
4.3	Hourly $H_{m0,TIG}$, $H_{m0,BIG}$ and $H_{m0,FIG}$ measurements at 011 during all storms	29
4.4	Upper left: hourly $H_{m0,TIG}$, $H_{m0,BIG}$ and $H_{m0,FIG}$ values at 011 during storm Eunice. Upper right: water elevation plot of the 19 th of February, 2022 at 10:00 CET. Lower left: wave spectrum of the 19 th of February, 2022 at 10:00 CET. Upper right: bispectrum of the 19 th of February, 2022 at 10:00 CET	30
4.5	Upper left: hourly $H_{m0,TIG}$, $H_{m0,BIG}$ and $H_{m0,FIG}$ values at 011 during storm Eunice. Upper right: water elevation plot of the 19 th of February, 2022 at 00:00 CET. Lower left: wave spectrum of the 19 th of February, 2022 at 00:00 CET. Upper right: bispectrum of the 19 th of February, 2022 at 00:00 CET	31
4.6	Upper left: hourly $H_{m0,TIG}$, $H_{m0,BIG}$ and $H_{m0,FIG}$ values at 011 during storm Eunice. Upper right: water elevation plot of the 19 th of February, 2022 at 19:00 CET. Lower left: wave spectrum of the 19 th of February, 2022 at 19:00 CET. Upper right: bispectrum of the 19 th of February, 2022 at 19:00 CET	32
4.7	Hourly $H_{m0,TIG}$, $H_{m0,BIG}$ and $H_{m0,FIG}$ measurements at 081 during all storms	33
4.8	Hourly $H_{m0,TIG}$, $H_{m0,BIG}$ and $H_{m0,FIG}$ measurements at 031 during all storms	34
4.9	Hourly $H_{m0,TIG}$, $H_{m0,BIG}$ and $H_{m0,FIG}$ measurements at 141 during all storms	35
4.10	Hourly $H_{m0,TIG}$, $H_{m0,BIG}$ and $H_{m0,FIG}$ measurements at 051 during all storms	36
4.11	R_{FIG}^2 for each measurement during all storms, where T_0 is defined as the first hour of a storm.	37
4.12	Modelling and measuring results during storm Corrie of the default run	38
4.13	Reflective lines configuration in the Western Scheldt	39
4.14	Snapshot of the hour where the largest $\Delta H_{m0,FIG}$ value is found during storm Corrie	40
4.15	Snapshot of the hour where the largest $\Delta H_{m0,FIG}$ value is found during storm Dudley	40
4.16	Snapshot of the hour where the largest $\Delta H_{m0,FIG}$ value is found during storm Eunice	41
4.17	Snapshot of the hour where the largest $\Delta H_{m0,FIG}$ value is found during storm Franklin	41
4.18	Snapshot of the relative change of the hour where the largest $\Delta H_{m0,FIG}$ value is found during storm Corrie	42

4.19	Snapshot of the relative change of the hour where the largest $\Delta H_{m0,FIG}$ value is found during storm Dudley	42
4.20	Snapshot of the relative change of the hour where the largest $\Delta H_{m0,FIG}$ value is found during storm Eunice	42
4.21	Snapshot of the relative change of the hour where the largest $\Delta H_{m0,FIG}$ value is found during storm Franklin	43
A.1	Significant wave height plot during storm Corrie	50
A.2	Significant wave height plot during storm Dudley	51
A.3	Significant wave height plot during storm Eunice	51
A.4	Significant wave height plot during storm Franklin	52
A.5	Water level elevation during storm Corrie at 011 that are labeled as erroneous	52
A.6	Water level elevation during storm Corrie at 011 that are labeled as erroneous	53
A.7	Water level elevation during storm Corrie at 081 that are labeled as erroneous	53
A.8	Water level elevation during storm Corrie at 081 that are labeled as erroneous	54
A.9	Water level elevation during storm Eunice at 011 that are labeled as erroneous	54
A.10	Water level elevation during storm Eunice at 081 that are labeled as erroneous	55
A.11	Water level elevation during storm Franklin at 011 that are labeled as erroneous	55
A.12	Water level elevation during storm Franklin at 081 that are labeled as erroneous	56
D.1	Default GSHHS shapefile near Hansweert	59
D.2	Adapted GSHHS shapefile near Hansweert	59
D.3	North Sea basin with the Oceanmesh2D grid. Green values are marked grid points that are associated with NaN values in computational domain.	60
D.4	Western Scheldt near Bath of EMODnet netCDF4 file prior to adaptations	61
D.5	Western Scheldt near Bath with a mismatch in bottom elevation	61
D.6	Western Scheldt near Bath with a fixed bottom elevation transition	61
D.7	A fictional location in a triangular grid	62
E.1	Modelling and measuring results during storm Corrie	63
E.2	Modelling and measuring results during storm Dudley	64
E.3	Modelling and measuring results during storm Eunice	64
E.4	Modelling and measuring results during storm Franklin	65
E.5	Absolute difference between SWAN simulations including and excluding the reflection lines during storm Corrie	66
E.6	Absolute difference between SWAN simulations including and excluding the reflection lines during storm Dudley	67
E.7	Absolute difference between SWAN simulations including and excluding the reflection lines during storm Eunice	67
E.8	Absolute difference between SWAN simulations including and excluding the reflection lines during storm Franklin	68
F.1	Maximum $H_{m0,FIG}$ during storm Corrie without the reflective lines	69
F.2	Maximum $H_{m0,FIG}$ during storm Corrie with the reflective lines	69
F.3	Maximum $H_{m0,FIG}$ during storm Dudley without the reflective lines	70
F.4	Maximum $H_{m0,FIG}$ during storm Dudley with the reflective lines	70
F.5	Maximum $H_{m0,FIG}$ during storm Eunice without the reflective lines	71
F.6	Maximum $H_{m0,FIG}$ during storm Eunice with the reflective lines	71
F.7	Maximum $H_{m0,FIG}$ during storm Franklin without the reflective lines	72
F.8	Maximum $H_{m0,FIG}$ during storm Franklin with the reflective lines	72

List of Tables

3.1	Summary of the measurement devices. F_s and r_v resemble the sampling frequency and vertical resolution, respectively.	13
3.2	Start and end time for the storms in storm season 2021-2022	15
3.3	Hours with dry running sensors	17
3.4	Number of hourly periods that include a burst during storm hours	18
4.1	H_{m0} for SS waves	25
4.2	H_{m0} for IG waves	25
4.3	Fraction of the total wave energy that can be attributed to frequencies larger than $f_{SS,upper} = 0.33\text{ Hz}$	27
4.4	Storm averaged $T_{m-1,0}$ for the entire frequency band	27
4.5	Storm averaged T_p	27
4.6	Pierson correlation coefficients between the IG and SS significant wave heights	28
4.7	Predictive skill values during different storms for different output locations excluding the reflection lines	39
4.8	Predictive skill values during different storms for different output locations including the reflection lines	39
4.9	Summary of $\Delta H_{m0,FIG}$ values	41
C.1	Iterations required before the accuracy is sufficient in 99.5% of the wet grid points	58

1

Introduction

1.1. Context

Long waves owe their name to their length. Their frequency is lower compared to the frequency of short sea-swell waves. The frequency value commonly used in literature which separates long and short waves is 0.04 Hz, but it should be noted that values close to this value are also used in various papers regarding the topic. The upper region of the long wave spectrum contains infragravity (IG) waves. The earlier mentioned 0.04 Hz forms the upper boundary and the lower boundary is generally in the region of 0.004 Hz. Contrary to sea swell (SS) waves, IG waves are not known to be directly generated by constant wind forcing. There are various mechanisms known for the energy transfer from SS frequencies to IG frequencies. They can be forced by wave groups (Longuet-Higgins & Stewart, 1962), which were distantly generated. The wave groups lose their groupiness due to individual wave breaking once the wave groups propagate into shallower waters. The bound IG waves then gets released as a free IG wave. The time-varying breakpoint mechanism (Symonds, Huntley, & Bowen, 1982) is an additional mechanism responsible for the generation of IG waves. Due to the temporal variability of the breakpoint, free IG waves are released in both seaward and landward direction. The bore merging mechanism (Bradshaw, 1980) occurs when one bore overtakes another. This nonlinear process leads to an increase of the wave period, thus to an energy transfer from short wave frequencies to long wave frequencies (Bertin et al., 2018). Long waves may have a large influence on various processes in the coastal area, such as sediment transport, dune erosion, dune breaching and dike failure (Bertin et al., 2018). For that reason, they have the potential to cause severe damages to the coastal communities located on or near the Dutch coast.

Numerous reports have firmly established the significance of IG waves in the context of runup. This is particularly the case on mildly sloping beaches and under energetic wave conditions. Wave runup on dissipative beaches is mainly influenced by IG waves, which occurs as a consequence of short-wave incidents saturating in the surf zone and IG waves dominate at the seaward edge of the swash zone. Even on less ideal beaches, such as reflective sandy beaches or gravel beaches, IG motions may contribute a significant amount to wave runup (Bertin et al., 2018). This relates overtopping to IG wave activity, as overtopping is related to wave runup.

1.2. Problem Analysis

The run-up and overtopping formulas in TAW (2002) have been key elements in the Dutch safety assessment for the overtopping failure mechanism. It does not explicitly include IG waves and Rijkswaterstaat is interested in the consequences. It could develop a new safety assessment where IG waves are included, but the question remains if that would lead to significantly better results. Recent studies suggest that the exclusion of IG waves leads to an underestimation of wave runup (Smits, 2023; Plouvier, 2022). Comparable outcomes may be anticipated within the Scheldt region, but this should be investigated before any conclusions are drawn. Little research has been done on IG waves in estuarine environments. Therefore, a study on this subject in the Scheldt region is warranted. Certain parts of Zeeland and surrounding provinces are situated at altitudes lower than sea level. The potential dike failure due to the underestimation of the run up calculated with TAW (2002) could therefore result in a catastrophe. A dike failure or dune breach is more likely to occur if the currently used method of TAW (2002) for overtopping is found to systematically result in an underestimation of the run up height. This, com-

bined with the lack of research on IG wave propagation in estuaries, poses a possible threat to the Netherlands. With this study, more insight will be obtained regarding IG waves in estuaries.

1.3. Objective

The main objective of this study is to investigate the effect of IG waves on the coastal safety in the Scheldt region. To that end, an attempt will be made to characterize the IG wave climate in the Scheldt region as thoroughly as possible. Conversely, it will not go into depth regarding hydraulic loads or wave run up on dikes, as the focus will primarily be on wave dynamics. The main objective has led to the formulation of the following research questions:

- What are the IG wave characteristics in the Scheldt region?
- Can FIG waves in the Scheldt region be modelled with SWAN?

Spectral and bispectral analyses will be used to obtain the IG wave characteristics in the Scheldt region. SWAN will be used to perform the FIG modelling.

1.4. Outline

This study will contain several chapters. The first chapter provides an introduction into the research. In this chapter, the context, problem analysis and the objective will be elaborated on. The second chapter provides the reader with a literature review on IG waves. The third chapter contains the methodology used to obtain the findings of the study. Chapter fourth describes the results of the study. The discussion, conclusion, and recommendations will finalize this report in chapters five, six, and seven.

2

Literature Study

The infragravity (IG) wave frequency bands are typically defined ranging from approximately 0.004 Hz to 0.04 Hz. The accompanying wavelength is longer, compared to sea swell (SS) waves. SS waves are easy to observe when looking at the sea with the naked eye. IG waves are harder to spot due to the length and the relatively low amplitude of an IG wave. Nevertheless, the contribution of IG waves towards the surface elevation should not be neglected, as it could be the difference between a sea defence failing and remaining intact. The literature review will contain sections regarding the generation and dissipation of IG waves. In addition, energy transfer between SS and IG waves, IG wave in tidal inlets, IG wave energy estimation and the FIG parametrization by [Ardhuin, Rawat, and Aucan \(2014\)](#) will be elaborated on.

2.1. Generation of IG waves

There are various mechanisms known that are responsible for the generation of IG waves. Getting a good understanding of the generation is crucial for the validity of models. Some of the known mechanisms will be elaborated on below.

2.1.1. Bound wave

A bound long wave may be forced by a short wave group ([Longuet-Higgins & Stewart, 1962](#)) in deep water. The frequency of the bound long wave is similar to the frequency of the wave group. In a bichromatic wave field this is equal to the difference between the frequencies of the short wave components. In general, the frequency of the bound long wave is approximately one magnitude lower compared to the frequencies of the short wave components ([Bertin et al., 2018](#)). The waves force a slight modulation to the mean sea level through second-order Stokes interactions. This leads to a slight set-down where the amplification of short wave components occurs and a set-up where the cancellation of short wave components takes place. Locations where short wave components amplify each other are locations where more momentum is present compared to their lower counterparts. This can be explained by the radiation stress, which is a concept introduced by [Longuet-Higgins and Stewart \(1960\)](#). It is defined as the depth-integrated and wave-averaged momentum flux due to waves ([Bosboom & Stive, 2023](#)). As Equation 2.1 shows, it combines the energy of short waves with the ratio of the group celerity and the individual celerity. Due to their efforts in [Longuet-Higgins and Stewart \(1962\)](#), it was possible to link the energy in short waves to the bound wave amplitude with Equation 2.2.

$$S_{xx} = E \left(\frac{2c_g}{c} - \frac{1}{2} \right) \quad (2.1)$$

$$\eta(x, t) = \frac{-S_{xx}(x, t)}{\rho(gh - c_g^2)} + C \quad (2.2)$$

In which:

S_{xx}	(N/m)	=	Radiation stress
E	(J/s ²)	=	Mean wave energy per unit area
c_g	(m/s)	=	Group celerity
c	(m/s)	=	Short wave celerity
η	(m)	=	Water level
ρ	(kg/m ³)	=	Water density
h	(m)	=	Water depth
C	(m)	=	Integration constant

The set-up and set-down is bound to the wave group and resembles a wave pattern, hence its name. In reality, the short wave field is not bichromatic, as it contains a large number of short wave components. The interactions of all the short wave components leads to a large variety of bound long waves of various magnitudes and directions.

2.1.2. Time-varying breakpoint

An additional mechanism that is responsible for the generation of IG waves is the moving breakpoint mechanism, firstly described by [Symonds, Huntley, and Bowen \(1982\)](#). This mechanism is based on the physics of a short wave breaking once its height is a fraction of the water depth. Generally, this occurs once the height of a short wave is approximately 40% of the water depth ([Symonds, Huntley, & Bowen, 1982](#)). The incident wave groups contains waves of varying amplitudes, per wave group. Therefore, the location where the wave groups lose their groupiness differs per wave group. Once the groupiness vanishes, two FIG waves are emitted both in the shoreward and the seaward direction. The shoreward propagating FIG wave has a chance to reflect on the coast, which leads to the reflected FIG wave now propagating into the same direction as the FIG wave that was seaward directed immediately after the release. The amplitude of the resultant outgoing wave depends on the phase difference between the reflected IG wave and the initially seaward propagating IG. Therefore, the energy leaked is dependent on the phase relationship between the initially shoreward and seaward directed propagating free waves.

2.1.3. Bore merging

The breaking of short waves results in the remainder of the wave reorganizing into bores. Similar to short waves, the velocity of a bore is dependent on its amplitude. Bore merging occurs, as the name suggest, once a bore overtakes another bore. As has been hinted at, this occurs when a bore with a bigger amplitude overtakes a bore with a smaller amplitude, due to its velocity being related to the amplitude. If the velocity difference is less significant but the slope of the beach is mild, bore merging could still occur as the bore with a larger amplitude has more time to overtake the bore with a smaller amplitude. This process leads to an increase of the wave period in the surf zone, which is by definition a contribution of the energy transfer from higher to lower frequencies ([Bertin et al., 2018](#)).

2.1.4. Wind gusts

[Vrećica, Soffer, and Toledo \(2019\)](#) described how wind gusts can be responsible for the generation of IG waves in deep water. Deep water surface waves propagate according to the dispersion relation, which can be observed in Equation 2.3. It is impossible for three wave interactions to resonate both in the spatial ($k_1 \pm k_2 = k_3$) and temporal ($f_1 \pm f_2 = f_3$) domain due to the nature of the dispersion relationship. To resonate in both domains, a closure is needed. This can be achieved with the Bragg resonance condition through: $k_1 \pm k_2 + k_b = k_3$. The additional term, k_b , resembles an inhomogeneity. Examples of such inhomogeneities in a wave field are ripples in the bed or a varying wind field. This results in the generation of IG waves.

$$\omega^2 = gk \tanh(kh) \quad (2.3)$$

In which:

ω	(1/s)	=	Angular frequency
g	(m/s ²)	=	Gravitational acceleration
k	(1/m)	=	Wave number

Generally, models average the wind over long distances. This could result in inaccurate results, as this leads to the omission of wind gusts, thus for the closing component in the Bragg resonance condition. The wavelength of the wind gusts oscillations required for the closing is in the order of 1 km and the periods capable of closing are between 1 min to 3 min if assumed that the gusts propagate with the mean wind speed (Vrećica, Soffer, & Toledo, 2019). This is only possible if the wind pattern is inhomogeneous, thus the wind should not be averaged for an accurate solution.

2.2. Dissipation of IG waves

There are various dissipation processes that lead to a decrease of IG wave energy. Two of them can be quantified with the use of the normalized bed slope parameter, β . The bed slope parameter can be used to derive whether IG wave breaking or dissipation through bed friction is dominant.

Equation 2.4 and Equation 2.5 describe how the normalized bed slope parameter (β) and subsequently the reflection coefficient (R) can be obtained. Steeper slopes (large β values) are able to reflect more wave energy compared to milder slopes (small β values). van Dongeren et al. (2007b) formulated $\beta < 0.25$ as a mild slope regime and $\beta > 1$ as a steep slope regime. In addition, almost full reflection occurs for IG waves if $\beta > 1.25$.

$$\beta_H = \frac{h_x T}{2\pi} \sqrt{\frac{g}{H}} \quad (2.4)$$

$$R = 2\pi\beta_H^2 \quad (2.5)$$

In which:

β_H	(-)	=	Normalized bed slope parameter
R	(-)	=	Reflection coefficient
h_x	(-)	=	Bed slope
T	(s)	=	IG wave period
g	(m/s ²)	=	Gravitational acceleration
H	(m)	=	Relevant wave height

It should be noted that a bed slope appears steeper for a lower frequency waves, compared to higher frequency waves (de Bakker, Tissier, & Ruessink, 2014).

2.2.1. IG wave breaking

The dominant dissipation mechanism for IG waves in the mild-slope regime is wave breaking, as they propagate with the short waves towards the shoreline (van Dongeren et al., 2007a). On the Dutch coast, at Ameland and Egmond, it has been observed that a large part of the IG wave dissipation takes place in very shallow water (0.65 m to 0.75 m) (de Bakker, Tissier, & Ruessink, 2014). This hints that IG wave breaking is the dominant dissipation mechanism at these locations. The small range in which the wave dissipation takes place is a sign that the cross-shore distance over which the dissipation occurs is limited. Generally, dissipation by bottom friction requires a significant distance over which the shear induced by the bottom friction can act on the propagating waves. It can therefore be concluded that the IG wave dissipation by wave breaking is dominant at the two previously mentioned locations.

2.2.2. Bottom friction

The bottom friction on sandy beaches is generally too low to account for the large IG wave energy losses that are observed. In this case, the bottom friction is considered as a secondary dissipation mechanism. Bottom friction can be primary dissipation at other locations if the friction is significant, such as coasts in the tropics that contain coral reefs (Pomeroy et al., 2015; Inch et al., 2017).

2.3. Energy transfer of SS and IG waves

The energy transaction between IG waves and SS waves is dependent on various properties of the environment it is propagating in. On steep beaches or on the outside of the surf zone of mild sloping beaches, the interaction is mainly with the SS waves. On mild sloping beaches, the energy transaction

is mainly with itself, creating higher IG harmonics. This is visualized in Figure 2.1. This is a plot of the imaginary part of the bispectrum, which describes the relative energy transfers between phase-coupled frequencies.

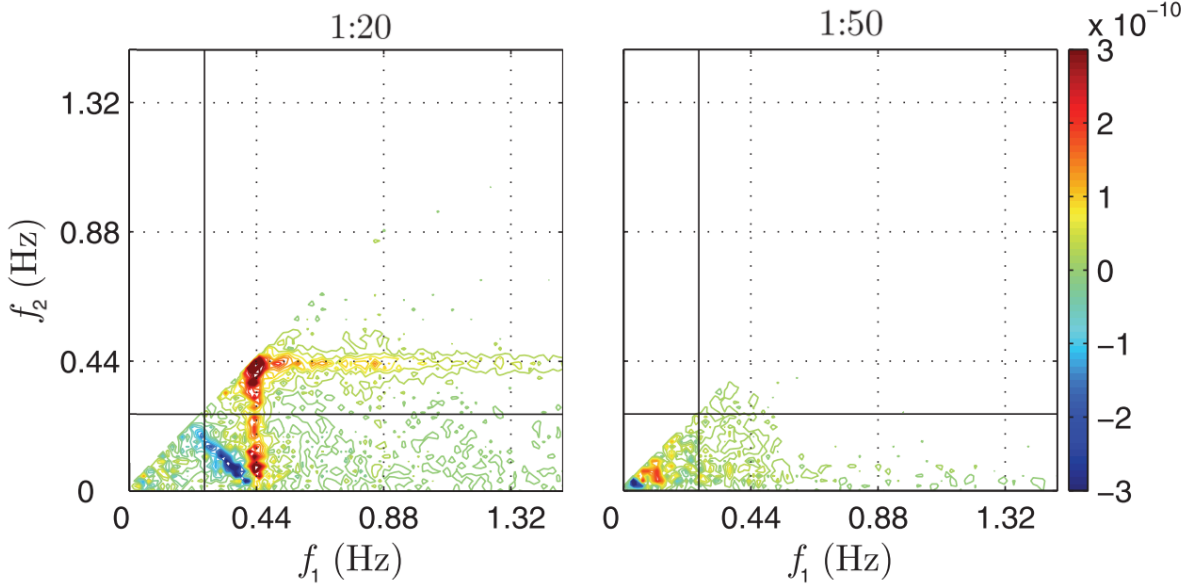


Figure 2.1: Comparison between the IG harmonics energy transfers. The left panel depicts a steep beach and the right panel depicts a gently sloping beach (de Bakker, Tissier, & Ruessink, 2016).

The presence of more intense colors in the plot of the steep sloping beach conclude that the energy interactions between the IG harmonics are more severe. Positive values (red) indicate energy transfer from f_1 and f_2 to f_3 , where $f_1 + f_2 = f_3$. Similarly, negative values (blue) indicate energy transfer from f_3 to f_1 and f_2 .

The direction in which swell propagates is expected to drive IG waves into the same direction. It should be noted, however, that swell is able to have a significant IG response in the opposing direction as well (Herbers, Elgar, & Guza, 1995). This could be the result of the varying breakpoint mechanism.

2.4. IG waves in tidal inlets

Little is known about the propagation of IG waves in tidal inlets and estuaries. Bertin and Olabarrieta (2016) studied the relevance of IG waves in the Albufeira Lagoon Inlet, which is wave dominated. It has been observed that both the bound wave mechanism and the breakpoint mechanism were of importance for the IG wave generation in the area. The bound long wave mechanism was responsible for 40% to 70% of the IG energy variance outside of the surf zone and up to the middle of the surf-zone. The breakpoint mechanism accounts for 50% to 90% of the IG energy variance from the inner part of the surf-zone up to the shoreline and the mouth of the inlet during low tide. This effect decreases during high tide, which could be due to less intense breaking.

It showed that the maximum of the IG wave height variance was always located at the ebb-tidal delta, throughout the entire tidal phase. Model results indicate that the maximum IG wave height remained on the outer edges of the ebb tidal delta during maximum ebb and low tide. For mid-flood and high tide, however, the IG wave energy was able to propagate through the ebb-tidal delta until the mouth of the inlet, due to blocking. Blocking is the phenomenon of a wave being unable to propagate further due to an opposing current. This mechanism is applicable to IG waves (Bertin & Olabarrieta, 2016). The result is the wave breaking without being reflected. This occurs when the relative group celerity is smaller than the velocity of the opposing current, in other words, when the absolute wave group celerity becomes negative. Equation 2.6 shows this condition in a formula. When full wave blocking occurs, no wave energy is able to propagate into the direction it was propagating to.

$$C_{g,a} = C_{g,r} + U \cos \alpha \quad (2.6)$$

In which:

$C_{g,a}$	(m/s)	=	Absolute wave group celerity
$C_{g,r}$	(m/s)	=	Relative wave group celerity
U	(m/s)	=	Current velocity
α	(-)	=	Angle between the wave and current

The wave dispersion relation shown in Equation 2.3 can be used to calculate the velocity of the opposing current for which a maximum period is blocked. Equation 2.7 shows this adapted version.

$$\omega^2 = (\omega_a - kU \cos \alpha)^2 = gk \tanh(kh) \quad (2.7)$$

In which:

ω_a	(1/s)	=	Absolute frequency
------------	-------	---	--------------------

From this equation follows that stronger opposing current speed are required to block waves with a longer period. It was observed that a theoretical, opposing current velocity of 2.4 m/s was required to block waves of any frequency in a water depth of 1 m. For a water depth of 0.5 m, the required current velocity decreased to a value of 1.7 m/s (Bertin & Olabarrieta, 2016). A theoretical situation has been plotted for $L = 25$ m and $T = 6$ s and can be observed in Figure 2.2. It can be seen that initially, a larger water depth results in a larger opposing current velocity requirement for which all waves are blocked. Eventually, it plateaus starting from a water depth of 13.85 m and for an opposing current velocity of 2.08 m/s, all waves are blocked.

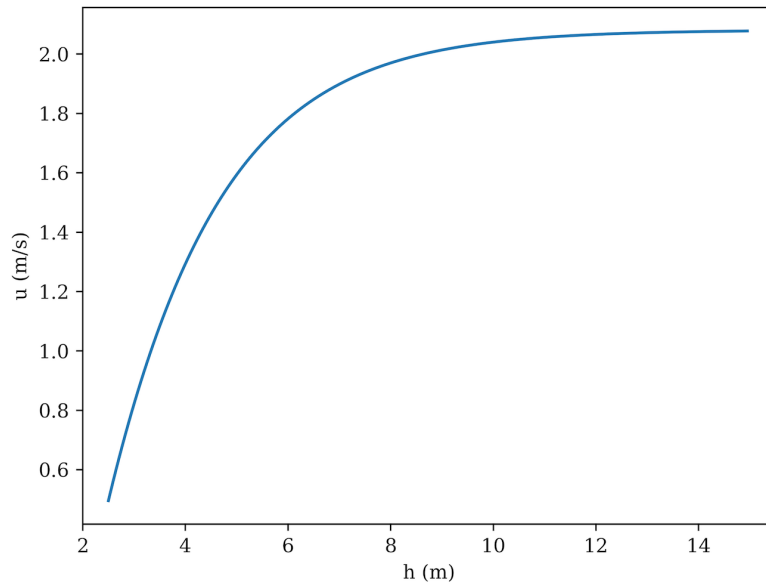


Figure 2.2: u - h plot for $L = 25$ m and $T = 6$ s according to the dispersion relation adjusted for Doppler shift

In reality, the phenomenon of wave blocking is more complex. The size of the Western Scheldt and the shipping channels it contains to guarantee the connection between the port of Antwerp and the North Sea results in the Western Scheldt having a large spatial variation in its bathymetry. van Dijk et al. (2019) used the NeVla-Delft3D model to study the effects of shoal margin collapses on the morphodynamics in the Western Scheldt. The NeVla model is a state-of-the-art model which is optimized

for hydrodynamics and morphology, and its domain is the Flemish part of the Scheldt up to Gent, the Western Scheldt and part of the North Sea (Weisscher et al., 2022). It is, however, possible to reduce the domain in order to speed up the computational time, which has been done in van Dijk et al. (2019), with the result solely containing results in the Western Scheldt.

The model results show ebb and flood flow velocities ranging from approximately 2 m/s in certain parts of the fairways and over 0.5 m/s on most parts of the intertidal flats. Kuijper (2013) contains measurements of the bathymetry of the Western Scheldt up to 2008. The height of the tidal flat is relative to NAP -2 m, which is approximately the low water value in the Western Scheldt. In this year, the shallowest intertidal flat, located between Hansweert and Bath, reads $\mathcal{O}(2\text{ m})$, which is equivalent to NAP 0 m. The deepest channel segment was the segment between Flushing and Terneuzen, which is $\mathcal{O}(15\text{ m})$, where no reference point has been mentioned.

Comparing the relevant figures from van Dijk et al. (2019) (not shown here) it can be concluded that generally, the larger flow velocities occur in the deeper sections of the Western Scheldt and the smaller flow velocities occur in shallower waters. Judging from this and taking the theoretic values from Bertin and Olabarrieta (2016) into account, it appears that total wave blocking will not occur in the Western Scheldt. However, some wave blocking can occur especially during ebb, when the mean flow velocity is directed in the opposing direction of the waves.

2.5. IG wave energy estimation

Herbers, Elgar, and Guza (1994) described IG motions on the continental shelf. A method was used to estimate the IG energy qualitatively from single-point measurements using integrals of the bispectrum. They measured the pressure on the seafloor in 13 m depth, 2 km offshore. The location is exposed to a wide range of propagation directions of approximately 180° and the mean cross-shore slope is approximately 0.005. An energy density spectrum was derived from the resulting data. The significant wave height, defined as $4\sqrt{E_\eta}$ where E_η is the surface elevation variance in the frequency range 0.06 Hz to 0.24 Hz, spanned 0.3 m to 3.3 m. As can be deduced from the mentioned frequency range, the field experiment measured solely the primary sea swell waves. The derived mean frequencies lie within the 0.10 Hz to 0.17 Hz range.

Hasselmann (1962) concluded with a perturbation expansion analysis that the interaction between two surface gravity waves (for example, two SS waves) with a small difference in frequency, Δf , excite a secondary wave with the frequency difference as a frequency (BIG wave). The spectrum $E_{forced}(\Delta f)$ of secondary pressure at the seafloor is shown in Equation 2.8.

$$E_{forced}(\Delta f) = 2 \int_{\Delta f}^{\infty} df \int_0^{2\pi} d\theta_1 \int_0^{2\pi} d\theta_2 D^2(f + \Delta f, -f, \Delta\theta + \pi) E(f + \Delta f, \theta_1) E(f, \theta_2) \quad (2.8)$$

In which:

$$\begin{aligned} E(f, \theta) &= \text{Frequency-directional spectrum of primary seafloor pressure} \\ D(f + \Delta f, -f, \Delta\theta + \pi) &= \text{Difference-interaction coefficient for two primary waves with} \\ &\quad \text{frequencies } f \text{ and } f + \Delta f \text{ and } \Delta\theta = |\theta_1 - \theta_2| \end{aligned}$$

$E(f, \theta)$ was estimated from the measurements and, along with the theoretical interaction coefficient D , inserted into Equation 2.8. The errors from the predicted E_{forced} can be attributed to the exclusion of primary waves with frequencies that lie out of the earlier mentioned bounds of 0.06 Hz to 0.24 Hz. These errors are, however, expected to be small.

A bispectral analysis can be used to isolate the forced wave component of the IG motions. The definition of the bispectrum can be observed in Equation 2.9.

$$B(f_1, f_2)df_1df_2 = 2E\{dP(f_1) dP(f_2) dP(-f_1 - f_2)\} \quad (2.9)$$

In which:

$E\{X\}$ = Expected value of X
 $dP(f)$ = Fourier-Stieltjes representation of the pressure time series $p(t)$, which can be seen in Equation 2.10

$$p(t) = \int_{-\infty}^{\infty} dP(f) \exp(2\pi i f t) \quad (2.10)$$

$B(f_1, f_2)$ vanishes for a linear wave field. As IG waves are secondary order waves, $B(f_1, f_2)$ is by definition non-zero and it results from the phase-coupled triads. The phase-coupled triads consist of two primary waves with frequencies f_1 and f_2 and a forced secondary wave with frequency $f_1 + f_2$. The biphaser, Equation 2.11, can be used to obtain a relative measure of the non-linear phase coupling between the two primary and the singular secondary waves.

$$b(f_1, f_2) = \frac{B(f_1, f_2)}{\sqrt{E(f_1) E(f_2) E(f_1 + f_2)}} \quad (2.11)$$

When swell-sea energy levels are high, non-linearities are relatively strong and the real part of $b(f_1, f_2)$ is nonzero over a wide range of frequencies. Difference-frequency interactions dominate the negative values of the biphaser for f_1 close to the spectral peak and f_2 in the IG frequency band. The positive values of $b(f_1, f_2)$ resemble the sum-interactions and are both close to the spectral peak. It has to be noted that weak forced waves cannot be detected with a biphaser, as the statistical uncertainties of a biphaser are considerable. [Herbers, Elgar, and Guza \(1994\)](#) mentions a minimum detectable biphaser value of approximately 0.5 Hz^{-1} .

The forced wave spectral density $E_{forced}(f)$ can be estimated by integrating the bispectrum, $B(f, \Delta f)$, over all wave pairs with difference-frequency Δf . The result can be seen in Equation 2.12.

$$b_i(\Delta f) = \frac{2 \int_{\Delta f}^{\infty} df B(f, \Delta f)}{\sqrt{(2 \int_{\Delta f}^{\infty} df E(f) E(\Delta f) E(f + \Delta f))}} \quad (2.12)$$

The theoretical equation for the lowest-order contribution to the bispectrum can be seen in Equation 2.13. Here, Equation 2.14, Equation 2.15 and Equation 2.16 describe the sum interactions of waves with frequencies f_1 and f_2 , difference interactions of waves with frequencies f_2 and $f_1 + f_2$, and difference interactions of waves with frequencies f_1 and $f_1 + f_2$, respectively.

$$B(f_1, f_2) = \int_0^{2\pi} d\theta_1 \int_0^{2\pi} d\theta_2 [B_1 + B_2 + B_3] \quad (2.13)$$

$$B_1 = D(f_1, f_2, \Delta\theta) E(f_1, \theta_1) \times E(f_2, \theta_2) \quad (2.14)$$

$$B_2 = D(f_1 + f_2, -f_2, \Delta\theta + \pi) \times E(f_1 + f_2, \theta_1) E(f_2, \theta_2) \quad (2.15)$$

$$B_3 = D(-f_1, f_1 + f_2, \Delta\theta + \pi) \times E(f_1, \theta_1) E(f_1 + f_2, \theta_2) \quad (2.16)$$

Substitution of Equation 2.13 into Equation 2.12 and neglecting the interactions involving primary waves within the IG wave frequency band results in Equation 2.17.

$$\frac{E_{forced}(\Delta f)}{E(\Delta f)} = \alpha_i(\Delta f) |b_i(\Delta f)|^2 \quad (2.17)$$

Where:

$$\alpha_i(\Delta f) = \frac{M_2(\Delta f)}{M_1^2(\Delta f)} \quad (2.18)$$

With:

$$M_n(\Delta f) = \frac{\int_{\Delta f}^{\infty} df \int_0^{2\pi} d\theta_1 \int_0^{2\pi} d\theta_2 D^n(f + \Delta f, -f, \Delta\theta + \pi) E(f + \Delta f, \theta_1) E(f, \theta_2)}{\int_{\Delta f}^{\infty} df \int_0^{2\pi} d\theta_1 \int_0^{2\pi} d\theta_2 E(f + \Delta f, \theta_1) E(f, \theta_2)} \quad (2.19)$$

The fraction of the energy density at frequency Δf that is forced locally and non-linearly is approximately equal to $|b_i(\Delta f)|^2$. The value associated with bias, $\alpha_i(\Delta f)$, is generally small in coastal environments, which results in $\alpha_i = 1$.

The contribution of the forced waves to the total IG energy in the frequency band from Δf_{min} to Δf_{max} can be obtained by double integrating the bispectrum over all difference-frequency interactions. The result can be seen in Equation 2.20.

$$b_{ii} = \frac{2 \int_{\Delta f_{min}}^{\Delta f_{max}} d\Delta f \int_{\Delta f}^{\infty} df B(f, \Delta f)}{(2 \int_{\Delta f_{min}}^{\Delta f_{max}} d\Delta f \int_{\Delta f}^{\infty} df E(f + \Delta f)E(f) \int_{\Delta f_{min}}^{\Delta f_{max}} d\Delta f E(\Delta f))^{1/2}} \quad (2.20)$$

Substituting the theoretical expression for the bispectrum, Equation 2.13, into Equation 2.20 and neglecting primary waves within the IG wave frequency band results in Equation 2.21.

$$\frac{\int_{\Delta f_{min}}^{\Delta f_{max}} d\Delta f E_{forced}(\Delta f)}{\int_{\Delta f_{min}}^{\Delta f_{max}} d\Delta f E(\Delta f)} = \alpha_{ii}|b_{ii}|^2 \quad (2.21)$$

Where:

$$\alpha_{ii} = \frac{N_2}{N_1^2} \quad (2.22)$$

With:

$$N_n = \frac{\int_{\Delta f_{min}}^{\Delta f_{max}} d\Delta f \int_{\Delta f}^{\infty} df \int_0^{2\pi} d\theta_1 \int_0^{2\pi} d\theta_2 D^n(f + \Delta f, -f, \Delta\theta + \pi) E(f + \Delta f, \theta_1) E(f, \theta_2)}{\int_{\Delta f_{min}}^{\Delta f_{max}} d\Delta f \int_{\Delta f}^{\infty} df \int_0^{2\pi} d\theta_1 \int_0^{2\pi} d\theta_2 E(f + \Delta f, \theta_1) E(f, \theta_2)} \quad (2.23)$$

It can be observed that α_{ii} and N_n are analogous to α_i and M_n . Similar to α_i , setting $\alpha_{ii} = 1$ shows excellent agreement with theoretical predictions.

2.6. FIG wave parametrization

[Ardhuin, Rawat, and Aucan \(2014\)](#) formalized a way to schematize the FIG wave height based on wave parameters. A significant correlation was found using Equation 2.24. This means that a large part of the FIG wave energy variations is caused by the short wave energy and the local depth.

$$H_{IG} \approx \alpha_1 H_s T_{m0-2}^2 \sqrt{g/h} \quad (2.24)$$

In which:

H_{IG}	=	Infragravity wave height
α_1	=	dimensional coefficient
H_s	=	Significant wave height
T_{m0-2}	=	Mean period based on the second order moment
h	=	Water depth

Equation 2.24 was modified to account for the parametrization of the directional distribution of IG wave energy and the shoaling of the directional spectrum. The former was achieved by approximating the IG wave spectrum as isotropic. The latter was accomplished with the insertion of Equation 2.25.

$$\sqrt{\frac{g}{h}} = \frac{kg^2}{c_G 2\pi f} \quad (2.25)$$

The empirical parametrization of the FIG wave source can be seen in Equation 2.26. The last term ensures that the spectrum is constant up to 15 mHz in the shallow water limit ($kh \rightarrow 0$).

$$E_{FIG}(f) = \frac{3}{40} \alpha_1^2 \frac{kg^2}{c_G 2\pi f} \frac{(H_s T_{m0-2}^2)^2}{\Delta f} (\min(1, 0.015/f))^{1.5} \quad (2.26)$$

3

Methodology

3.1. Study area

This section will give a brief description of the Western Scheldt and the Eastern Scheldt. Figure 3.1 depicts every lost village in Zeeland due to inundation (Kuipers et al., 2004). As the number of vanished towns exceeds 100, it becomes apparent that Zeeland has struggled with inundations throughout its history.

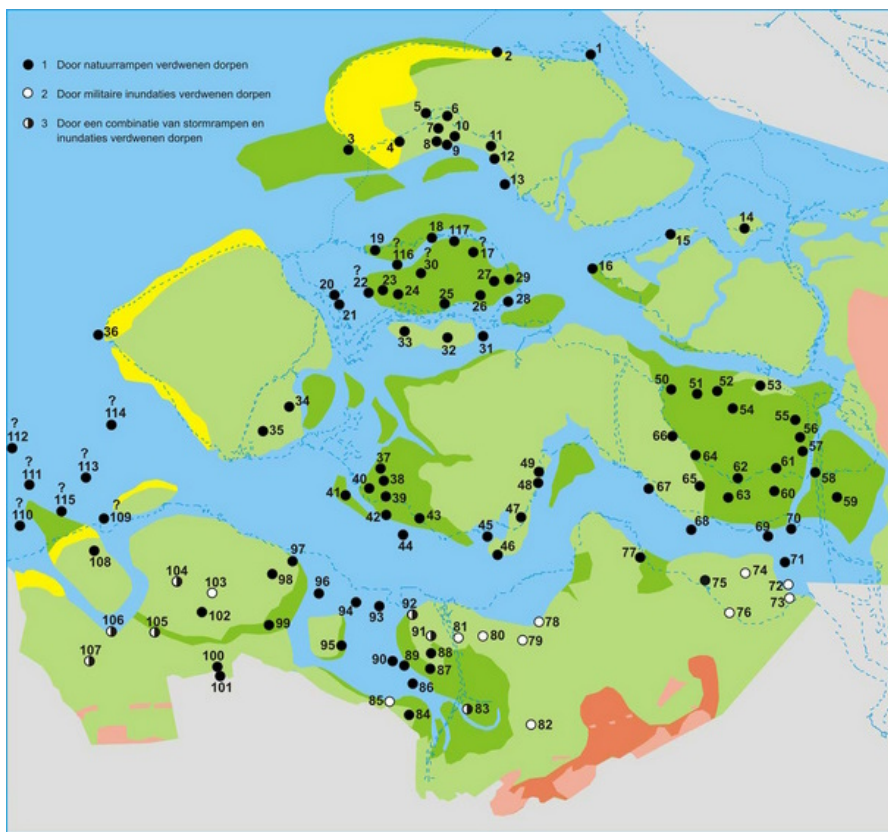


Figure 3.1: Villages lost to inundation. Depicted is an estimation of the land border in 1573 (Kuipers et al., 2004)

3.1.1. Western Scheldt

The Western Scheldt is an estuary located in the south western part of the Netherlands. Its source is the Scheldt river which flows through northern France and Belgium, before discharging into the Western Scheldt. The Western Scheldt is enclosed by Walcheren at the north west, Zuid-Beveland at the north east and Zeeuws-Vlaanderen at the south. It is a highly complex system with intertidal flats and deep intertidal channels. The Antwerp port is highly dependent on the Western Scheldt, as it connects the port to North Sea. A brackish salt water marsh is located near the mouth of the Scheldt river, called 'het Verdronken Land van Saeftinghe'. The tidal range at this location is on average 4.80m. During

spring tide and a western wind direction, this value can increase to 7 m. This makes the tidal range at 'het Verdrongen Land van Saeftinghe' the largest along the entire Dutch coast. The difference with the mouth of the Western Scheldt is relatively large, where the tidal range is 3.5 m (Jacobusse & Decleer, 2003). The entirety of the coast along the Western Scheldt exists of dikes, except near the mouth, as this segment consists of dunes.

3.1.2. Eastern Scheldt

The Eastern Scheldt is located north of the Western Scheldt, in the Dutch province of Zeeland. It is enclosed by Schouwen-Duiveland at the north west, Tholen at the north east, Noord-Beveland at the south west and Zuid-Beveland at the south east. Unlike the Western Scheldt, the Eastern Scheldt is partially disconnected from the North Sea. The Deltaplan entailed the construction of a storm surge barrier at the mouth of the Eastern Scheldt, the completion of which occurred on the 4th of October, 1986. Under normal circumstances, the gates are open and tidal activity can propagate into the Eastern Scheldt. If a water level elevation of +3 m NAP is predicted, the gates will be closed to protect the area surrounding the Eastern Scheldt. This occurs on average once a year.

3.1.3. Site conditions

The tide along the Dutch coast is semidiurnal and the tidal range at Vlissingen ranges between approximately 2.1 m to 4.8 m. Spectral analysis on wave data with records of 20 min was used to obtain the graphs shown in Figure 3.2 and Figure 3.3. These resemble the significant wave height, H_{m0} , at Cadzand and OS4. The measuring period is during the storm season of 2021 - 2022, which was from the 1st of October until the 31st of March. Cadzand is a village located south of the mouth of the Western Scheldt and OS4 is a buoy located in front of the Eastern Scheldt storm surge barrier. Both use a stepping gauge to measure the water surface elevation. The maximum spectral significant wave height during the storm season of 2021 - 2022 at both locations is approximately 3 m and 2 m, respectively.

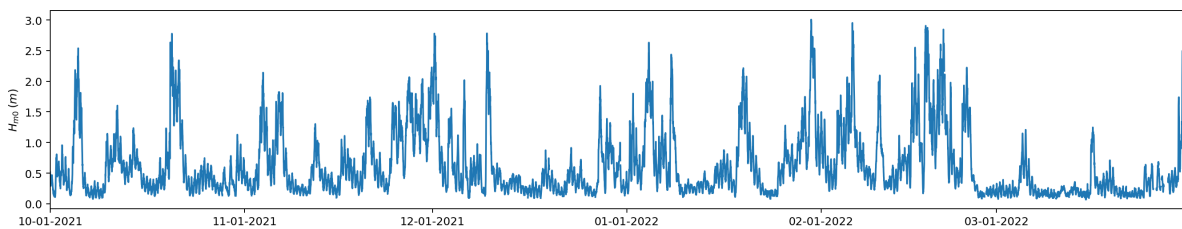


Figure 3.2: 20-minute averaged H_{m0} values at Cadzand of the 2021-2022 storm season

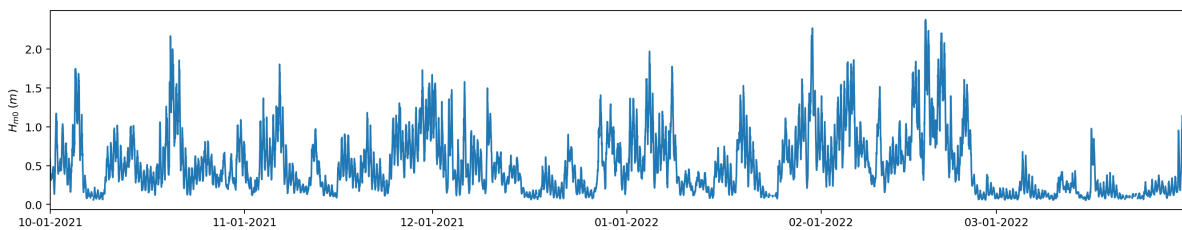


Figure 3.3: 20-minute averaged H_{m0} values at OS4 of the 2021-2022 storm season

3.2. Data Analysis

3.2.1. Measuring Devices

There are various ways to obtain wave data in the field. Rijkswaterstaat commonly employs devices like radar, stepping gauges, regular waveriders or directional waveriders. The five measuring device used in this study are shown in Table 3.1 and their locations are shown in Figure 3.4.

ID	Name	Depth	Type	F_s	r_v
011	Bath	8.5 m	Stepping Gauge	2.56 Hz	0.05 m
081	Hansweert	8.5 m	Stepping Gauge	2.56 Hz	0.05 m
031	Brouwershavense Gat 2	10.2 m	Stepping Gauge	2.56 Hz	0.05 m
141	Oosterscheldekering 4	10.2 m	Stepping Gauge	2.56 Hz	0.05 m
051	Cadzand	8.5 m	Stepping Gauge	2.56 Hz	0.05 m

Table 3.1: Summary of the measurement devices. F_s and r_v resemble the sampling frequency and vertical resolution, respectively.

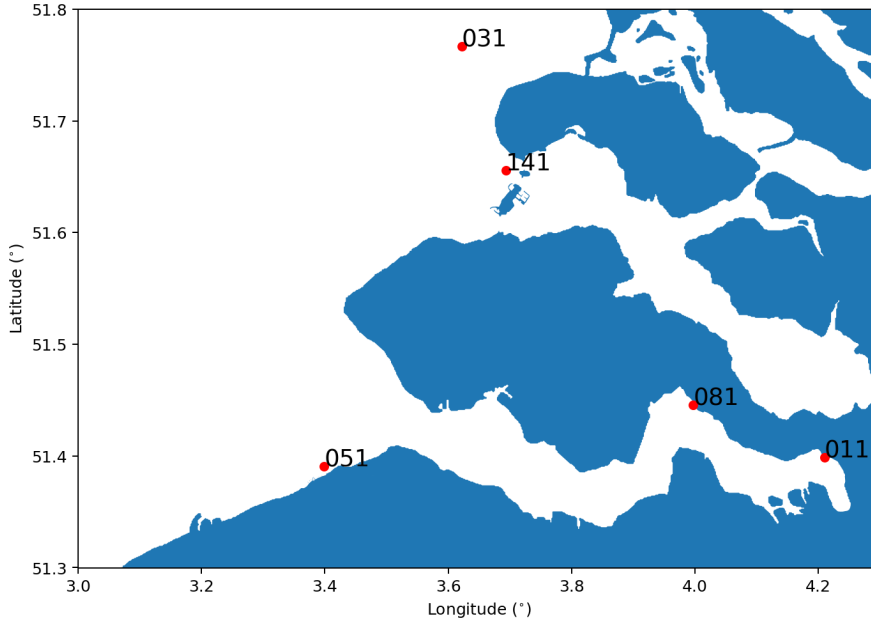


Figure 3.4: ID values of the measurement devices in the Scheldt region.

3.2.2. Storm Description

The data used in this study is provided by Rijkswaterstaat and spans the storm season of 2021 - 2022. An analysis on the entire database would be expensive in computational terms. Luckily, the time series can be reduced, as low IG wave energy values are deemed irrelevant for this study. The significant IG wave height is low ($\mathcal{O}(\text{cm})$) in periods with no storm activity in the areas of the North Sea adjacent to the Netherlands, which is the vast majority of days. Storms are named in the Netherlands. This happens before the storm season starts by the meteorological institutions of England, Ireland and the Netherlands. Once the weather conditions are sufficiently extreme, a 9 on the scale of Beaufort, it will be declared a storm and it will get one of the previously determined names. Using the storm names allows for the removal of a large section of the data. The significant wave height during these periods can be $\mathcal{O}(\text{dm})$. The days during which these storms roamed over the North Sea will be used to investigate for which days high IG wave energy values can be expected. A brief description on storm Corrie, Dudley, Eunice and Franklin will be given below.

Corrie

On January the 31st, Storm Corrie travelled from Scotland to the northern region of Germany, before continuing its course towards into the southeast direction. Simultaneously a high pressure area approached from the west. Initially, winds of Beaufort force 7 were registered and its direction was from the southwest. After the passing of the high pressure area, it changed into a northwestern storm with a Beaufort force 9. As storm Corrie passed, significant wave heights from 6 m to 7 m are recorded. This is significant in relation to the significant wave height of approximately 2 m to 3 m on the Dutch continental shelf which was measured before the passing of storm Malik. Storm Malik is not considered

in this report as did not affect the Dutch coast significantly (Zijderveld et al., 2022b).

Dudley

In the evening of February the 16th, a complex low pressure area was located north of the North Sea and the Norwegian Sea. The direction of the wind was to the east and the Beaufort force was generally 7 to 8, with outliers of 9. During the evening, it travelled in the direction of Denmark. The accompanying cold front moved into the southeastern direction, across the Netherlands. Subsequently after the passage of the cold front the wind direction rotated into the eastern direction. In the early mornings, winds with a Beaufort force of 8 to 9 were measured, with wind gusts of 10 (Zijderveld et al., 2022a).

Eunice

In the afternoon of February the 18th, the winds gained strength along the Dutch coast and the IJsselmeer region towards a Beaufort force of 9 to 10, originating from the southwestern direction. The direction of the wind changed to the east during the evening and locally, wind gusts of a Beaufort force of 11 were measured (Zijderveld et al., 2022a).

Franklin

The low pressure area named Franklin was located south of Iceland on the 20th of February. During the morning, its Beaufort force was 5 to 6, but it increased towards 8 to 9 during the evening. The disturbance moved from Scotland to the northern region of Germany on the following day. The weakened wind increased in strength again, reaching a Beaufort force of 7 to 8 and originating from the northwestern direction (Zijderveld et al., 2022a).

3.2.3. Storm tracks

Figure 3.5 shows the trajectories of the storms during their presence in the North Sea and its surrounding areas. The tracks of Dudley, Eunice and Franklin are based on Zijderveld et al. (2022a). Unfortunately, there is no trajectory included for Corrie in Zijderveld et al. (2022b). The track of Corrie is therefore based on a weather forecast from the Dutch media network RTL. Closed arrowheads depict the position at 1 am CET and open arrowheads depict the position at 1 pm CET, on their respective days. The distance between the the arrowheads is therefore the distance travelled by the storms in 12 h. Note that for storm Corrie only one arrowhead is depicted, as the data source is a projection and not a measurement.

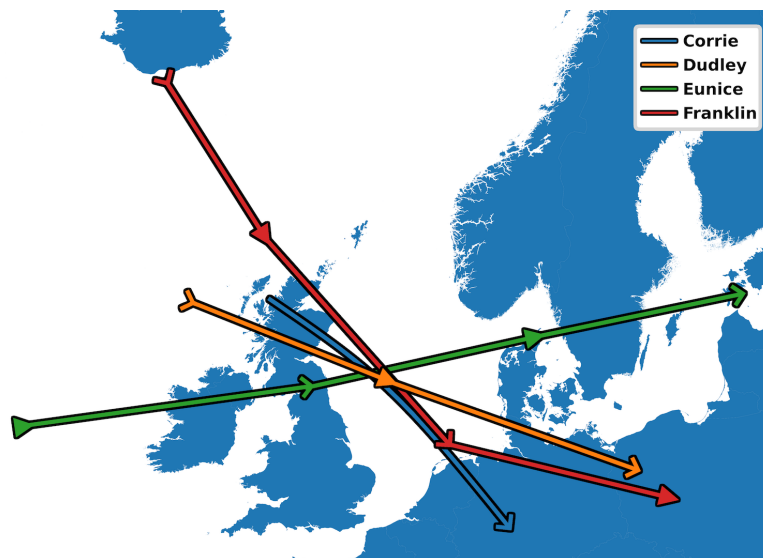


Figure 3.5: Trajectory of storm Corrie, Dudley, Eunice and Franklin

3.2.4. Measuring Period

Only selecting storm days allows for a reduction of the time series from 180 days to 12 days, considering 3 days per storm. The 72 hours per storm can be trimmed down even further, with the use of the variance of the water elevation signal according to $H_S = 4\sqrt{\sigma^2}$. This has been done by visually inspecting the hourly H_S values. Figure 3.6 shows the significant wave height, H_S , during the days where storm Corrie passed the North Sea at every measurement device. It shows that the time where an increase in the significant wave height is present at one location can be different for another, which complicates the definition of the begin and end of the storm. The procedure for determining these timestamps is by prioritizing the measurement devices with a higher significant wave heights over those with lower significant wave height values. The start and end time used for the data analysis for storm Corrie is portrayed by the red lines in Figure 3.6. The H_S plots for the other storms can be observed in Appendix A. The start and end hour found using this method can be seen in Table 3.2.

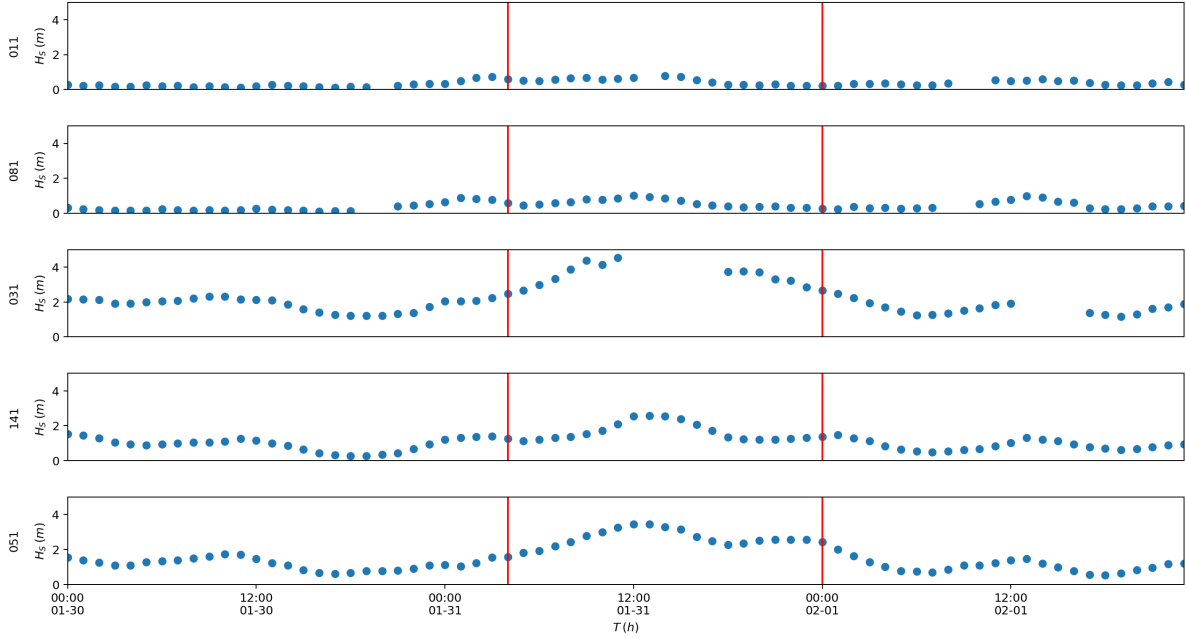


Figure 3.6: H_S plot during storm Corrie

Storm	t_{start}	t_{end}
Corrie	31-01-2022 04:00	01-02-2022 00:00
Dudley	16-02-2022 10:00	17-02-2022 18:00
Eunice	18-02-2022 12:00	19-02-2022 12:00
Franklin	20-02-2022 13:00	21-02-2022 21:00

Table 3.2: Start and end time for the storms in storm season 2021-2022

3.2.5. Data Processing

This section discusses the data description of the Rijkswaterstaat measurement records. The approach used for handling missing data will be elaborated on first, followed by the measures taken regarding erroneous data.

Missing data

It appears that data is missing during certain periods. Performing an analysis on such data leads to inaccurate results. Fortunately, it is straightforward to determine and remove these periods once the record duration is chosen. The number of data points in a record should be equivalent to the number of seconds in the record multiplied by the sampling frequency. If the number of data points is less

than the expected value, it is apparent that data points are missing. These records should be removed from the analysis if too many values are missing. If a small numbers of data points is missing, it is deemed not significant enough to discard an hourly record. Here, a threshold of 5% is selected as the maximum permissible percentage of missing data. An example of the result of this procedure can be observed in Figure 3.7. With a sampling frequency of 2.56 Hz and record duration of 1 h, 9216 values are anticipated. This leads to a period being excluded if more than 460 values is missing. The top part depicts the raw surface elevation signal. It exhibits interruptions in the sections from 37 h to 41 h and 61 h to 66 h. The bottom part shows the same signal where periods with missing values are removed.

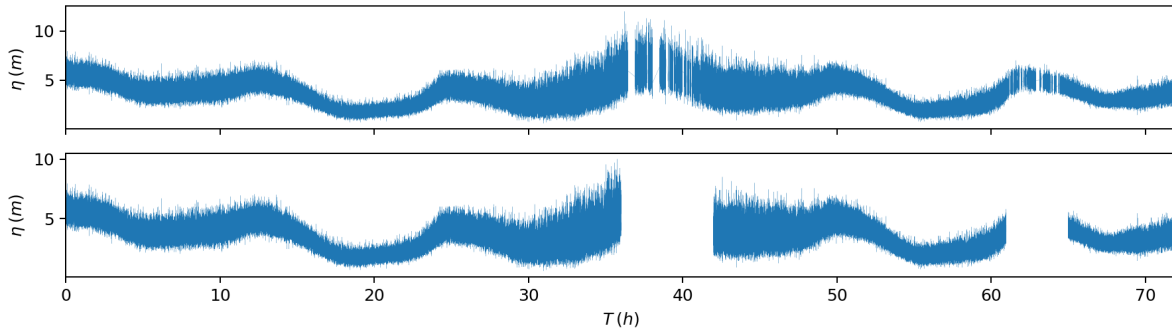


Figure 3.7: Water level elevation at 031 during storm Corrie

Measurement errors

It appears that certain measurement devices endure periods where the water level elevation is beneath the lowest sensor of the stepping gauge. This translates to a water elevation signal as depicted in Figure 3.8. A sharp cutoff can be seen at $\eta = 0$ m. There is still some wave action during this period, as there are nonzero measurements during the period where the bottom cutoff is present. Also visible in this plot is the vertical resolution of the measurement device, which is 0.05 m. This is the case for all devices. These measurements can lead to wrong conclusions, this time periods containing such measurements should be removed. This has been done by visual inspection. Table 3.3 shows the hours containing measurements with the sharp cutoff at $\eta = 0$ m.

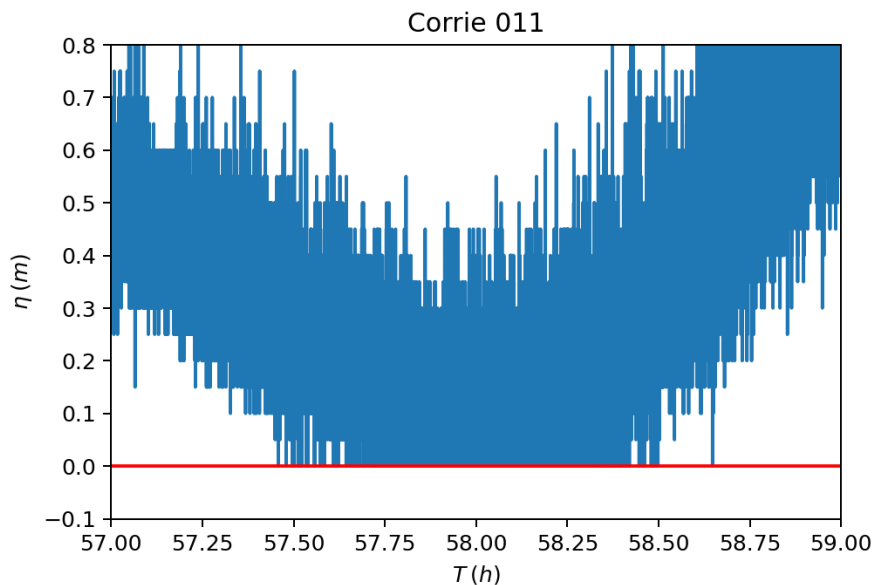


Figure 3.8: Water level elevation on 01-02-2022 from 09:00 to 11:00 at 011

	051	081	011	031	141
Corrie	-	19, 20, 56, 57	20, 57, 58	-	-
Dudley	-	-	-	-	-
Eunice	-	33, 34, 35	34, 35	-	-
Franklin	-	35, 36	36	-	-

Table 3.3: Hours with dry running sensors

For some hourly records adjacent to the removed hourly records according to Table 3.3, the same cutoff can be found. An example is shown in Figure 3.9. Visible is the water level elevation of the rejected 57th hour and the beginning of the 58th hour at 081 during storm Corrie. To reject the 58th hour is deemed unwarranted as there are only a few data points for $\eta = 0$ m and rejecting it results in the loss of useful data. Besides, some of the $\eta = 0$ m values can be accurate recordings, especially from 58.15 h onward. Here, the overall water level elevation is increasing and by visual inspection it appears that the troughs are not cut off anymore.

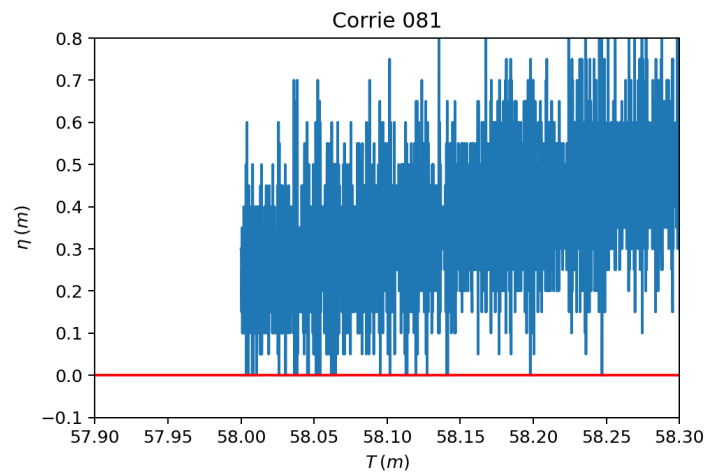


Figure 3.9: Water level elevation on 01-02-2022 from 09:54 to 10:18 at 081

Unusual Bursts in the Surface Elevation Signal

The surface elevation signal appears to contain some remarkable structures. An example can be seen in Figure 3.10, which depicts the water level elevation during the 7th hour of storm Corrie.

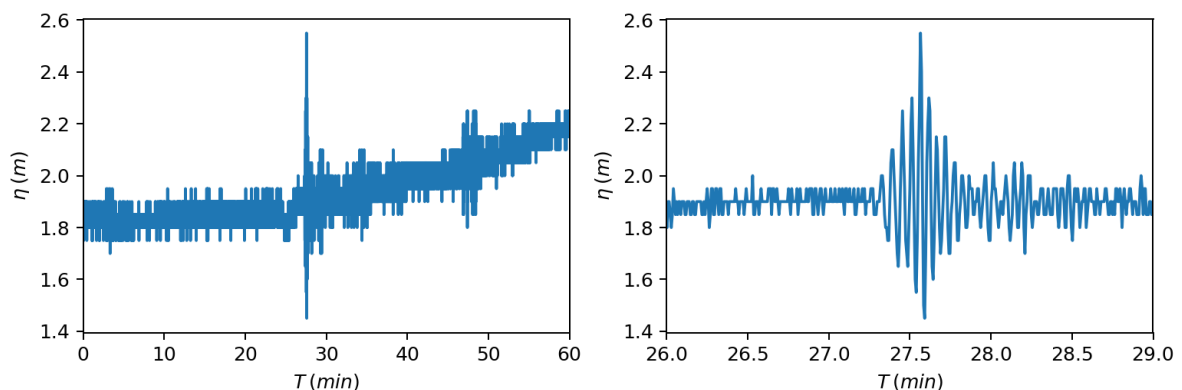


Figure 3.10: Water level elevation during the 7th hour of storm Corrie at measurement device 011

A large number of seagoing vessels navigate through the Western Scheldt. These ships generate waves that influence the water level elevation. These ship waves could exhibit a shape like the example given

in Figure 3.10. If these bursts are indeed the result of waves generated by seagoing vessels, it would be expected to see these structures in the signal more often at measurement devices 081 and 011, given their proximity to the shipping lane and the accompanying intensity of the waves. Similarly, there is a sluice located at approximately 2 km from measurement device 011. This is another structure that could influence the water elevation signal.

The first step in investigating if this applies to the data is the division of the surface elevation signal in intervals of 1 hour. The new intervals are detrended in blocks of 200s in an attempt to obtain a stationary signal. The newly detrended signal will be used to calculate the standard deviation, σ . If an hourly signal contains a value higher than 4σ and lower than -4σ , it will be registered as a signal containing a burst. The factor of 4 appears strict, but through visual inspection it proved to be fitting. Using a stricter factor results in the exclusion of periods where the burst is clearly distinguishable. If a more lenient factor is used, periods are included where no burst as seen in Figure 3.10 is distinguishable. These periods are generally during the peaks of the storms, which is expected as those periods contain more variance. The results are summarized in Table 3.4.

	051	081	011	031	141
Corrie	0	2	5	0	0
Dudley	0	3	1	0	0
Eunice	0	3	1	0	0
Franklin	0	6	3	0	2

Table 3.4: Number of hourly periods that include a burst during storm hours

Table 3.4 provides a remarkable result. The hypothesis appears to hold. Nearly all the hours that contain a burst are registered at the measurement devices in the Western Scheldt. A more in depth study should be performed to analyse if these bursts are indeed generated by ships.

3.2.6. Spectral Analysis

A spectral analysis can be used to derive wave characteristics between certain frequency bands. In addition, a bispectral analysis can be used to investigate the interactions between frequency components in a signal. This section describes the setup of the spectral analysis as well as the reasoning why a bispectral analysis is used.

Spectral analysis setup

A shortcoming of a regular spectral analysis is that finite frequency resolution has to be chosen. The resolution, denoted as Δf , removes details at a resolution equivalent to $1/D$, where D is the duration of the time series. The frequency resolution can be improved by using a time signal, however, the signal should still be considered stationary, which limits the length (Holthuijsen, 2007).

A solution is a division of the wave record into various subsections and computing the variance density for each part. With this procedure the variance density spectrum is χ^2 -distributed with $2p$ degrees of freedom and the error is reduced with \sqrt{p} , as can be seen in Equation 3.1.

$$\epsilon = \frac{1}{\sqrt{p}} \cdot 100\% \quad (3.1)$$

The reduction of this error comes with a consequence, as the new frequency interval has increased to $\delta f = p\Delta f$. The lower boundary of the IG wave spectrum that is used in this study is $f_{min} = 0.005$ Hz. This will be used as a final resolution constraint, as details at this magnitude should not be removed.

The time period selected is divided in blocks of 1 h. This value was chosen as it should be lengthy enough to contain a significant amount of IG waves. Given the sampling frequency of 2.56 Hz, this leads to 9218 data points if no data is missing. The final resolution constraint, 0.005 Hz, corresponds to a block length of 200s, which leads to 18 blocks per record. This results in $\epsilon = 24\%$ and 36 degrees of freedom. Furthermore, the boundary values for the IG and SS waves bands are: $f_{IG,lower} = 0.005$ Hz, $f_{IG,upper} = 0.04$ Hz, $f_{SS,lower} = 0.04$ Hz and $f_{SS,upper} = 0.33$ Hz.

Bispectral analysis

A regular spectral analysis is an efficient method of obtain various wave characteristics between certain frequency bands. This has been shown for SS waves and IG waves in the previous subsection. It cannot take the interactions between frequencies into account. As a consequence, a regular spectral analysis can only be used to derive wave characteristics for TIG waves. The SWAN model used in this thesis only accounts for FIG waves. This complicates a direct comparison between the measurements and the model results.

A bispectral analysis is a more complex approach for the derivation of certain wave characteristics compared to a regular spectral analysis. It focuses on quantifying the interactions between frequency pairs. This results in a longer computation time, but it allows for the separation of TIG and BIG waves in a signal. If those are known, the FIG wave significant wave height can be calculated using Equation 3.2 (Reniers et al., 2021).

$$H_{TIG} = \sqrt{H_{BIG}^2 + H_{FIG}^2} \rightarrow H_{FIG} = \sqrt{H_{TIG}^2 - H_{BIG}^2} \quad (3.2)$$

Finally, the bispectral analysis uses the same parameter values as the spectral analysis.

3.3. SWAN Modelling

SWAN is a third-generation spectral wave model for obtaining realistic estimates of wave parameters in coastal areas, lakes and estuaries from given wind, bottom and current conditions. However, SWAN can be used on any scale relevant for wind-generated surface gravity waves. The model is based on the wave action balance equation with sources and sinks.

A SWAN model that is specifically calibrated for the REFLEX measurements will be used to assess whether FIG wave can be modeled in the Scheldt region. The time step in the model is 3600s or 1 h. The 5 output locations are located in the Western Scheldt region and correspond to the locations of the measurement devices of Rijkswaterstaat. After performing model runs, the predictive skill will be calculated to quantify to which extent the calibration on the REFLEX campaign is valid for the Scheldt region.

3.3.1. SWAN file Setup

This section will provide an explanation of every line in the default SWAN input file. The entire file without comments can be observed in Appendix B. As can be seen, the file is separated by commented lines, which gives structure to the `swan`-file. Each subsection following this paragraph will use this structure as well. Each subsection starts the lines of the file that apply to the title of the subsection. The explanation for certain decisions can be found thereafter.

Start-up commands

```
1 PROJECT 'FIG_unst' 'RND'
2 SET NAUTICAL
3 MODE NONSTAT
4 COORDINATES SPHERICAL CCM
```

The first line is required and allows the user to define a number of strings to identify the SWAN run. For this run, the name is `FIG_unst` and the run identification is `RND`. The second line indicates that the nautical convention is used for the direction of wind and waves. The line of code that follows is used to force the model to run in non-stationary mode. Due to the dynamic environment of the North Sea, this is preferred over a stationary run. The final line sets the coordinate system in spherical mode, which leads to the model using the longitude and latitude instead of x and y values.

Computational grid

```
1 CGRID UNSTRUCTURED CIRCLE 72 0.005 0.04
2 READ UNSTRUCTURED
```

The first line defines that the computational grid is unstructured and that the spectral direction covers a full circle. The circle is segmented into 72 directions, which leads to a resolution of 5° . The frequency bands used in this model is from 0.005 Hz to 0.04 Hz, thus only accounting for waves in the IG range. The final line reads the unstructured grid file.

Bathymetry, current, wind, Hs, Tm

```

1 INPGRID HSS REG -4 50 0 429 888 0.030303001 0.013511658 EXC -99.0 NONSTAT
  → 20220131.030000 1. HR 20220201.000000
2 READINP HSS 1 'Hm0_Corrie.inp' 3 0 FREE
3
4 INPGRID TSS REG -4 50 0 429 888 0.030303001 0.013511658 EXC -99.0 NONSTAT
  → 20220131.030000 1. HR 20220201.000000
5 READINP TSS 1 'Tm10_Corrie.inp' 3 0 FREE

```

The first line describes the significant wave height, to be used as an input for the computations. Contrary to the computational grid, this grid is rectangular. The origin of the grid is at -4° longitude and 50° latitude. There are 429 meshes with a length of 0.030303001° in the longitudinal direction and 888 meshes with a length of 0.013511658° in the latitudinal direction. It can be calculated that the furthest point from the origin is at 9° longitude and 62° latitude. This complies with the range of the retrieved input data for H_{m0} and T_{m-10} .

The model ignores significant wave height values of -99 m. This is used to exclude meshes that represent land, as it is trivial that no wave heights are present at these locations. Finally, the model should treat the significant wave height as a non-stationary variable and it computes an hourly value from 3 AM on the 31st of January 2022 until 12 AM on the 1st of February 2022.

The second line forces the model to use the `Hm0_Corrie.inp` file for the input of the significant wave height.

Considerable similarity can be found between the first 2 and last 2 lines. The last 2 lines describes how SWAN should handle the input of the significant wave period. As can be deduced from the similarity, it treats the significant wave period the same as the significant wave height.

The data used for the boundary conditions for T_{m-10} and H_{m0} originates from [European Union-Copernicus Marine Service \(2019\)](#) and are a result of an atmospherically driven WAVEWATCH III model. [Ardhuin, Rawat, and Aucan \(2014\)](#) originally used T_{m0-2} for their parametrization, which gives more weight to the lower frequencies. Simply using another spectral wave period would lead to inaccurate results. In this case, an underestimation would be expected as T_{m0-2} values are larger than T_{m-10} values. The α_1 values used in this model, however, are calibrated on T_{m-10} values instead of T_{m0-2} values, thus justifying the use of the former.

Boundary conditions

```

1 include 'IGsource.inp'

```

The FIG generation as a result of wave group breaking will be simulated with the use of an empirical FIG wave source term proposed by [Ardhuin, Rawat, and Aucan \(2014\)](#). The parametrization of the reflected free IG wave energy contains various variables, such as the sea-swell wave height (H_{SS}) and time period (T_{m0-2}). It also includes a term which symbolizes the energy transfer from incident SS waves to reflected free IG waves, α_1 [1/s]. The FIG source lines work best at locations where no SS waves have been dissipated. The lines should therefore be placed outside of the surfzone. In reality, the α_1 variable symbolizes the rate of transfer of energy per unit time and can vary strongly in a spatial and temporal sense. If this value is set to 0, no free IG waves will be radiated, simulating a coast that where all FIG wave energy is dissipated.

The FIG source lines are specified in the `IGsource.inp` file and the line of code forces SWAN to use to contents of the file. A snippet of the contents of the `IGsource.inp` file is shown below.

```

1 $ SHET:
2 OBSTACLE FIG alpha1=0.00044721359549995795 REFL 0 LINE -7.8219331523601188e-01
  ↪ 6.0380977746795132e+01 &
3 -8.9547890136325359e-01 6.0327018370331920e+01 &
4 -9.9241438689017203e-01 6.0292680196330423e+01 &
5 -1.0344570567467706e+00 6.0228911462040742e+01 &
6 -9.8540157931406025e-01 6.0133260116000642e+01 &
7 -1.0449641505604315e+00 6.0106280382055644e+01 &
8 -1.0764964404879769e+00 6.0067037995417557e+01 &
9 -1.1500750149990506e+00 6.0071942080056637e+01 &
10 -1.1512402152269527e+00 5.9991005657596141e+01 &
11 -1.1710936388821511e+00 5.9959121308736663e+01 &
12 -1.2271526406149920e+00 5.9937046866264410e+01 &
13 -1.2435006052403095e+00 5.9853657587785918e+01 &

```

The first line of code is a string which clarifies to which coast the following values belong to. Here, SHET represents the Shetland Islands. The second line of code describes physical parameters for the FIG line. The α_1 value of the FIG source line of the Shetland Islands is 0.00044 Hz. The value after REFL is the percentage of the incident FIG wave height that should be reflected seaward. Here, this has been disabled, as the value is 0. The remaining lines of code are the coordinates of the vertices that should be connected to resemble the FIG source line.

Physics

```

1 FRIC JON 0.01
2 OFF QUAD
3 OFF BREA
4 OFF WCAP

```

The JONSWAP bottom friction variable, χ , has been set to $0.01 \text{ m}^2/\text{s}^3$, which is significantly lower than the suggested value of $0.038 \text{ m}^2/\text{s}^3$ (The SWAN Team, 2023). The bottom friction is dependent on various factors, including the wave frequency f and the depth parameter kh . This leads to different friction coefficient values for different frequency bands. Therefore, there is not one χ value in reality, but a large variety per location. The value of $0.01 \text{ m}^2/\text{s}^3$ has been chosen as it appears to give good results for the REFLEX measurements. It should be noted that this value is prone to changing as a different value could result in a higher skill for the Rijkswaterstaat measurements.

Three physical processes are deliberately turned off. The influence of the quadruplets, white capping and depth induced breaking are deemed not of significance. The quadruplets are important in deep and intermediate water. The DIA approximation used in SWAN, however, is a poor approximation for long crested waves, which leads to the exclusion of quadruplets in the model. White capping is practically steepness induced wave breaking. As the model only resolves FIG waves, this is unlikely to occur, which allows for the exclusion of this term. Wave breaking is expected to occur only very close to the shoreline. To increase efficiency of the model, this has been turned off.

Numerical parameters

```

1 PROP BSBT
2 NUM ACCUR NONSTAT mxitns=100

```

This line of code specifies that the BSBT scheme should be used. The second line of code describes that maximum number of iterations the model is allowed to perform before it goes to the next step is 100. A table describing the number of iterations it took for each timestep to obtain the accuracy requirement of 99.5% can be found in Appendix C.

Output requests

```

1 POINTS 'RIG' FILE 'NSP_IG.txt'
2 SPEC 'RIG' SPEC2D 'Corrie.spec2D' OUTP 20220131.040000 1. HR

```

The longitude and latitude of the 5 measurement devices are stored in `NSP_IG.txt`. The first line of code tells SWAN that the output points for the model can be found in this file. The second line of code specifies that the outputs of the model should be stored in a file named `Corrie.spec2D`. The result should contain a 2 dimensional frequency-direction spectra with hourly values from 4 AM on the 31st of February onward. Note that this is one hour later than the start of the computations. This is to prevent the influence of the initial state of SWAN on the model results, as this is often unreliable and erroneous ([The SWAN Team, 2023](#)).

Closing commands

```
1 COMPUTE NONSTAT 20220131.030000 1. HR 20220201.000000
2 STOP
```

The final lines of code starts and ends the computation of SWAN. It tells SWAN that a non-stationary run should be conducted from 3 AM on the 31st of January until 12 AM of the 2nd of February with time steps of 1 h.

3.3.2. Computational domain

The tool used to generate the unstructured grid is called Oceanmesh2D ([Roberts, Pringle, & Westerink, 2019](#)). Oceanmesh2D is a set of Matlab scripts that are able to generate triangular meshes. The user can specify various parameters for the generation of the grid, such as the minimum and maximum resolution in meters. Additionally, a shapefile representing the coastline and a netCDF4 file representing bathymetry values should be supplied.

The shapefile is an adapted version of the Global Self-consistent, Hierarchical, High-resolution Geography Database, or GSHHS for short ([Wessel & Smith, 1996](#)). The accuracy of the default version of the GSHHS shapefile proved to be insufficient for the requirements essential of the SWAN model. The shapefile was modified near the measurement devices to locally obtain a more accurate coastline. This has been described in Appendix D.1. The bathymetry data is an adapted version of the European Marine Observation and Data Network, or EMODnet for short ([EMODnet Bathymetry Consortium, 2018](#)). Similarly to the shapefile, the netCDF4 file proved to be inaccurate in the nearshore regions of the computational domain. This has been resolved with the use of Python, as has been explained in D.2. The grid spans from 4°W to 9°E longitude and from 50°N to 62°N latitude, which roughly corresponds to the area of the North Sea. The resolution of the input grids is 0.0303° in the longitudinal direction and 0.0135° in the latitudinal direction.

3.3.3. FIG Source Lines

The FIG source lines used in the SWAN model adhere to the notion that they should be located outside of the surfzone. The depth where the largest SS waves break has been defined at a water depth of 10 m. This results in the FIG source lines depicted in Figure 3.11.

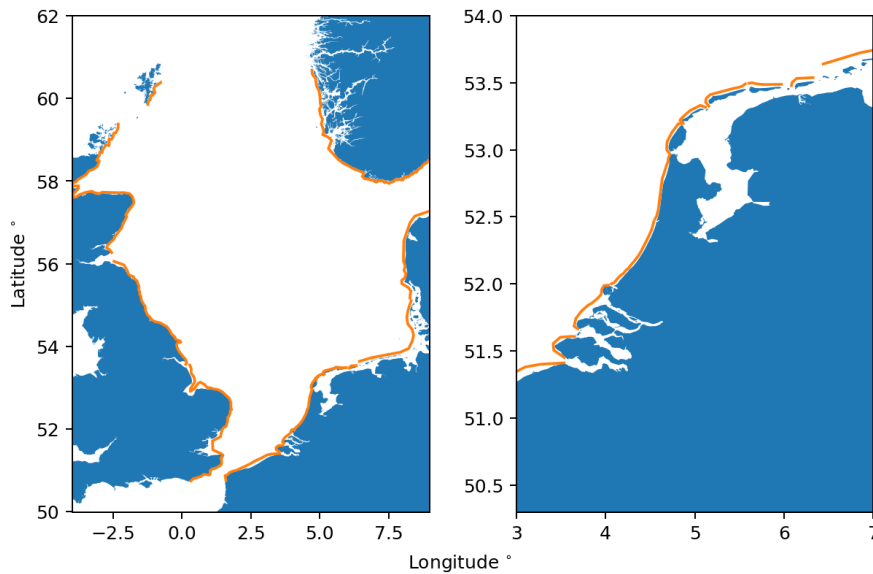


Figure 3.11: FIG source lines configuration surrounding the North Sea basin

Figure 3.12 shows the bathymetry in the Scheldt region. The red line depicts the FIG source lines in the area. As can be seen by the underlying yellow color, it is indeed located at a depth of approximately 10 m. The problem, however, is that there are shoals located seaward of certain sections of the FIG source lines. The shoals cause a decrease in wave energy reaching the FIG source lines due to wave breaking. As a result, the FIG waves that are emitted seaward from the FIG source line have less energy than would be the case if the shoals were not present. The solution would be to move the FIG source lines seaward, in such a way that they are located outside the actual surfzone. This would result in more accurate results for outputs on the seaward side of the FIG source lines, as this is the intended way for the parametrization by [Arduin, Rawat, and Aucan \(2014\)](#). Unfortunately, the FIG source lines in SWAN are non-transmissible. Modifying the FIG source lines in the aforementioned manner means that no FIG energy from the North Sea basin is able to reach the output locations.

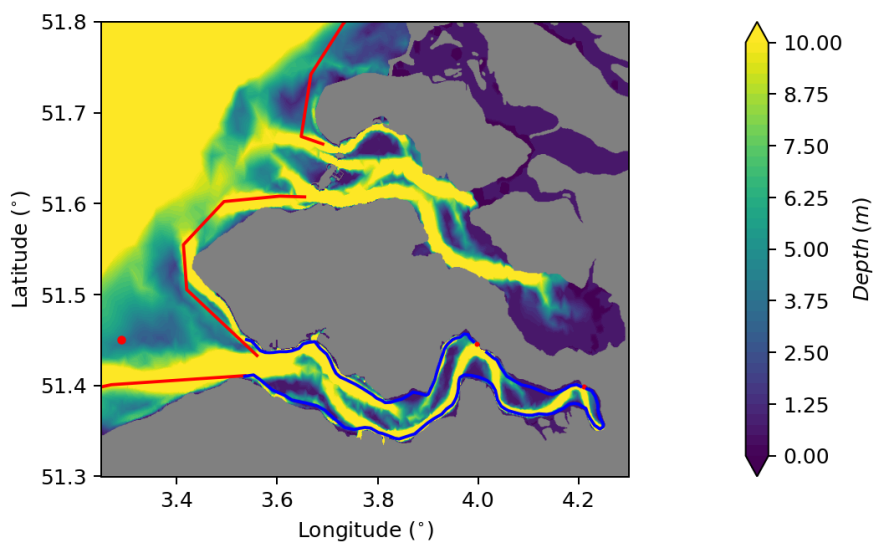


Figure 3.12: Bathymetry Zeeland

Another problem arises with the source lines being non transmissible. The measurement device near Cadzand, 051, is situated behind the FIG source line of Belgium. Thus, no FIG energy is able to reach

this output location. The last segment could be removed in order to ensure that FIG energy stemming from the North Sea basin is able to reach Cadzand. This option was waived as it is expected that this segment of the FIG source line has a significant contribution to the FIG energy measured at the other output locations, due to its proximity. Another solution will be explored, where a different location with approximately the same depth as the measurement location of Cadzand will be used. The new location can be seaward or landward of the shoal. Positioning the output location seaward of the shoal is expected to result in an overestimation compared to the bispectral analysis result for Cadzand, as the shoal is expected to lower the measured FIG energy. For this reason, the location used for Cadzand is located to a position on the shoal, where the depth is equivalent to the depth of the measurement device near Cadzand. The new location is marked with the most western red dot in Figure 3.12.

4

Results

This chapter contains the results of the spectral analyses, in addition to the results of the SWAN modelling.

4.1. Spectral analyses results

This section contains the findings of the spectral analysis and the bispectral analysis. The spectral analysis will discuss the storm averaged SS and IG wave heights. Subsequently, an assessment will be done on the storm averaged variance density spectrum. The bispectral analysis will provide insight into the relative contribution of the free and bound components of the total IG energy.

4.1.1. Spectral analysis

The storm averaged spectral analysis results for $H_{m0,SS}$, $H_{m0,IG}$, T_{m-10} and T_p can be found in Table 4.1, Table 4.2 and Table 4.4 and Table 4.5, respectively. Two remarkable features stand out for the H_{m0} tables.

1. The significant difference of magnitude between the $H_{m0,SS}$ and $H_{m0,IG}$ values encountered at measurement device 051, 031 and 141, compared to measurement device 081 and 011. It is likely that this is related to the immediate area in which the devices are located. The former are directly adjacent to the North Sea, whereas the latter are located in more sheltered areas in the Western Scheldt. This verifies the assumption that the dissipation processes at locations 081 and 011 are more developed or that SS waves are not able to penetrate the estuary due to other processes, such as reflection and refraction.
2. The wave heights at the 081 and 011. Table 4.1 shows that $H_{m0,SS}$ is similar for the two measuring devices. For $H_{m0,IG}$, however, it shows that the values at 011 are approximately twice as high compared to 081.

	011	081	031	141	051
Corrie	0.276 m	0.217 m	3.46 m	1.594 m	2.482 m
Dudley	0.477 m	0.535 m	2.156 m	1.259 m	1.504 m
Eunice	0.715 m	0.895 m	3.193 m	1.627 m	2.159 m
Franklin	0.499 m	0.495 m	2.921 m	1.553 m	2.041 m

Table 4.1: H_{m0} for SS waves

	011	081	031	141	051
Corrie	0.038 m	0.024 m	0.256 m	0.191 m	0.231 m
Dudley	0.077 m	0.042 m	0.117 m	0.082 m	0.109 m
Eunice	0.107 m	0.056 m	0.214 m	0.142 m	0.188 m
Franklin	0.077 m	0.039 m	0.171 m	0.126 m	0.161 m

Table 4.2: H_{m0} for IG waves

The values in Table 4.1 and Table 4.2 are derived from the storm averaged variance density spectra, which can be observed in Figure 4.1. The contrast between the measurement devices is also evident in this figure, especially during storm Corrie. Here, the spectral peaks of measurement device 031, 141 and 051 are approximately an order of magnitude larger than the spectral peaks of measurement device 081 and 011. The difference is even larger when solely the IG frequency range is considered, of which the upper frequency boundary has been denoted in the figure by the brown dashed line. Interestingly, measurement devices 011 and 141 have a similar value in the IG frequency range during storm Dudley and Eunice, while the former is located at a sheltered location and the latter does not. The pink dashed line represents the upper limit of the SS wave domain. It is evident that for the measurement devices in the Western Scheldt, the peak frequency does not fall within the SS wave frequency domain. In fact, it is only for storm Eunice that more energy is present in the SS wave bounds as opposed to the higher frequency, gravity wave bounds. These findings are summarized in Table 4.3, which provides the fraction of the wave energy contained by waves with a frequency larger than $f_{SS,upper} = 0.33$ Hz.

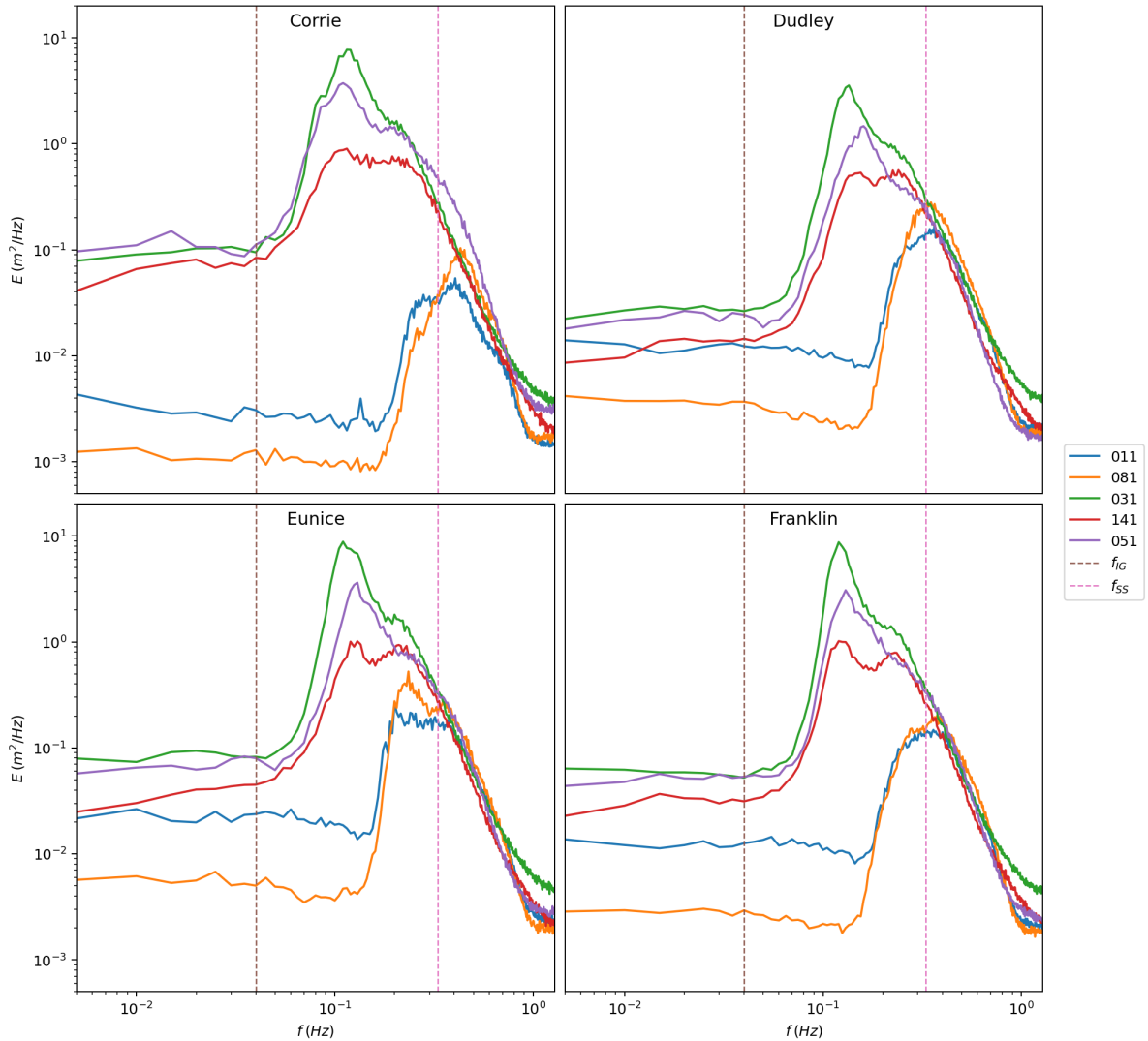


Figure 4.1: Storm averaged variance density spectra at all measurement devices during all storms

	011	081	031	141	051
Corrie	0.73	0.90	0.04	0.12	0.12
Dudley	0.66	0.69	0.10	0.19	0.15
Eunice	0.48	0.46	0.05	0.14	0.11
Franklin	0.63	0.70	0.07	0.15	0.12

Table 4.3: Fraction of the total wave energy that can be attributed to frequencies larger than $f_{SS,upper} = 0.33$ Hz

Additionally, the peak frequencies of the more sheltered measurement devices are larger than the peak frequencies of the measurement devices located in the North Sea. The same can be concluded from Table 4.4. This table shows the storm averaged spectral wave period based on the -1^{th} and the 0^{th} spectral moment, T_{m-10} , at all measurement devices during each storm. The higher peak frequencies at measurement device 011 and 081 are symbolized by the lower T_{m-10} values in Table 4.4. The actual peak periods, based on the inverse of the peak frequency, can be observed in Table 4.5.

	011	081	031	141	051
Corrie	3.082 s	2.421 s	7.781 s	6.661 s	7.135 s
Dudley	3.577 s	2.864 s	5.992 s	4.840 s	5.523 s
Eunice	4.211 s	3.417 s	7.325 s	5.692 s	6.459 s
Franklin	3.533 s	2.816 s	6.813 s	5.565 s	6.165 s

Table 4.4: Storm averaged $T_{m-1,0}$ for the entire frequency band

	011	081	031	141	051
Corrie	2.469 s	2.41 s	8.333 s	8.696 s	9.091 s
Dudley	2.740 s	2.985 s	7.407 s	4.167 s	6.25 s
Eunice	5.000 s	4.255 s	9.091 s	7.692 s	7.692 s
Franklin	2.500 s	2.740 s	8.333 s	8.333 s	7.692 s

Table 4.5: Storm averaged T_p

Correlation

The correlation can be used to investigate the relation between variables and it indicates if changes in one variable are associated with changes in another. Recent proceedings showed a strong correlation between $H_{m0,SS}$ and $H_{m0,TIG}$ in the North Sea (Naporowski, 2020). The assessment for the Scheldt region will be conducted with a normalized H_{m0} and the Pearson correlation coefficient, ρ . The normalized H_{m0} is defined as is shown in Equation 4.1. Here, $H_{m0,max}$ is defined as the largest significant wave height during a storm at a measurement device. The normalization process leads to $\overline{H_{m0}}$ values ranging between 0 to 1.

$$\overline{H_{m0}(t)} = \frac{H_{m0}(t)}{H_{m0,max}} \quad (4.1)$$

This allows for a visual inspection to give an impression of the correlation. Figure 4.2 shows the normalized significant wave height for all locations during all storms. The corresponding correlation values can be observed in Table 4.6. The table shows only one poor result, which represents the correlation during storm Corrie at measurement device 081. Judging from the graph, it appears that the $\overline{H_{m0,TIG}}$ and $\overline{H_{m0,SS}}$ values increase and decrease at the same rate, but not at the same time. Moreover, the three measurement devices located adjacent to the North Sea register very strong correlation values, where only one is below 0.8. The opposite can be said for the two measurement devices located in the Western Scheldt, as only two correlation coefficients exceed 0.8.

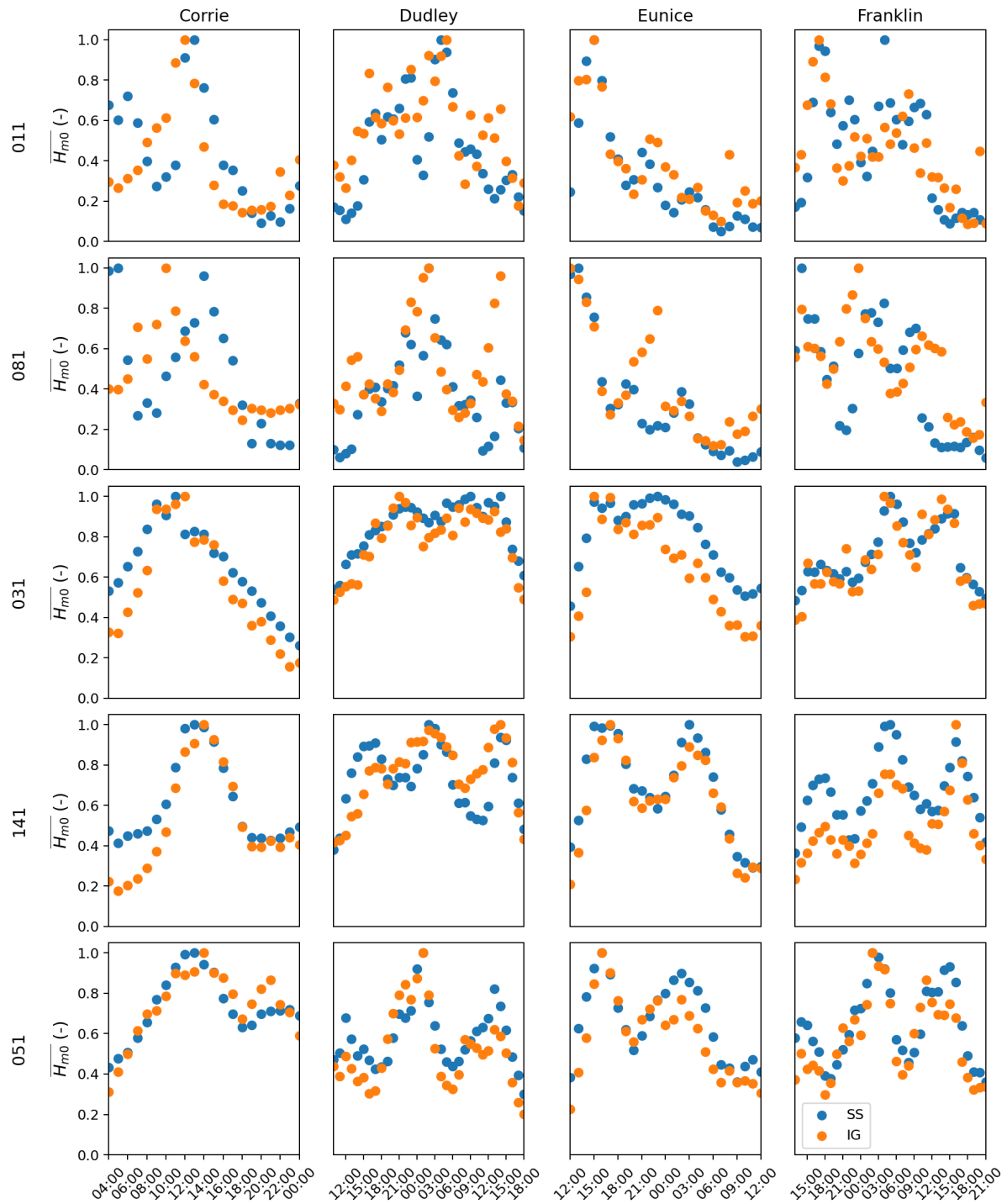


Figure 4.2: $\overline{H_{m0,IG}}$ and $\overline{H_{m0,SS}}$ at each measurement device during all storms

	Corrie	Dudley	Eunice	Franklin
011	0.523	0.734	0.87	0.715
081	0.128	0.505	0.823	0.474
031	0.938	0.923	0.934	0.932
141	0.937	0.657	0.956	0.87
051	0.886	0.866	0.89	0.888

Table 4.6: Pierson correlation coefficients between the IG and SS significant wave heights

4.1.2. Bispectral analysis

Figure 4.3, Figure 4.7, Figure 4.8, Figure 4.9 and Figure 4.10 show the hourly TIG, BIG and FIG significant wave height values during all storms, for each measurement device.

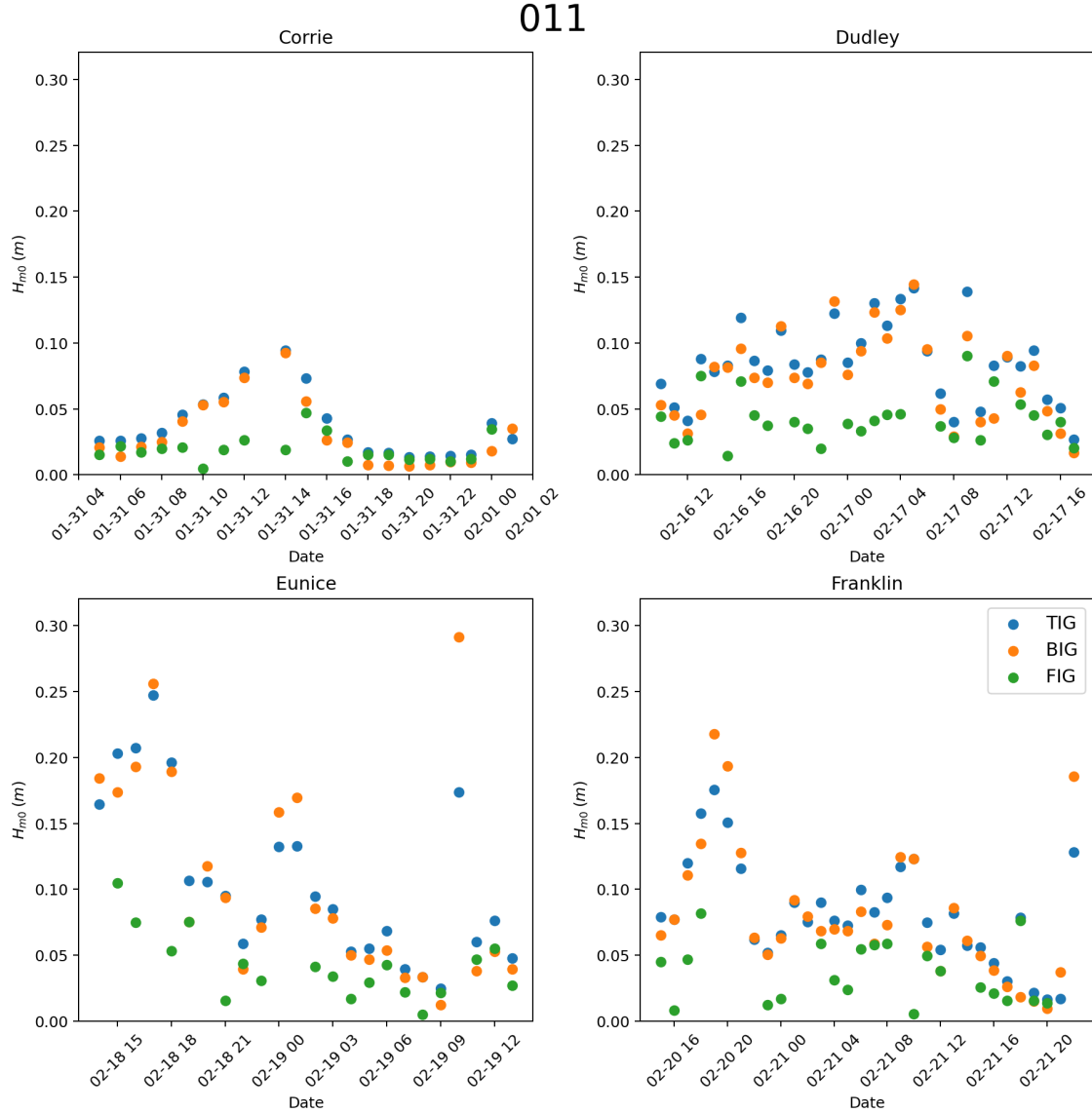


Figure 4.3: Hourly $H_{m0,TIG}$, $H_{m0,BIG}$ and $H_{m0,FIG}$ measurements at 011 during all storms

011, Bath

Figure 4.3 shows remarkable results. The measurement results during storm Corrie shows a maximum $H_{m0,TIG}$ of 0.095 m, with the BIG component being a large contribution towards the TIG significant wave height. This result is unexpected, as it appears improbable that any IG waves that far in the Western Scheldt are locally generated. The bispectral results for the other storms are considered erroneous. All three storms show inconsistencies for $H_{m0,FIG}$. This is a consequence of the quadratic nature of Equation 3.2 and follows from the bispectral analysis, as during certain hours $H_{m0,TIG} < H_{m0,BIG}$. This is physically impossible, as this would mean a negative $H_{m0,FIG}$ value. Thus, using Equation 3.2 results in 'NaN' values for $H_{m0,FIG}$, which is expressed in the figure as a discontinuity.

To investigate the cause of the excessive $H_{m0,BIG}$ value, a thorough examination will be conducted on the instance where this phenomenon appears most pronounced, which occurred on the 19th of February, at 10:00 CET. Figure 4.4 shows the $H_{m0,TIG}$, $H_{m0,BIG}$ and $H_{m0,FIG}$ values during the entire storm,

along with the water level elevation, wave spectrum and bispectrum for a certain hour. The red striped line in the H_{m0} plot indicates the specific hour to which the water elevation signal, wave spectrum, and bispectrum correspond. In this figure, it corresponds to the 19th of February, 10:00 CET.

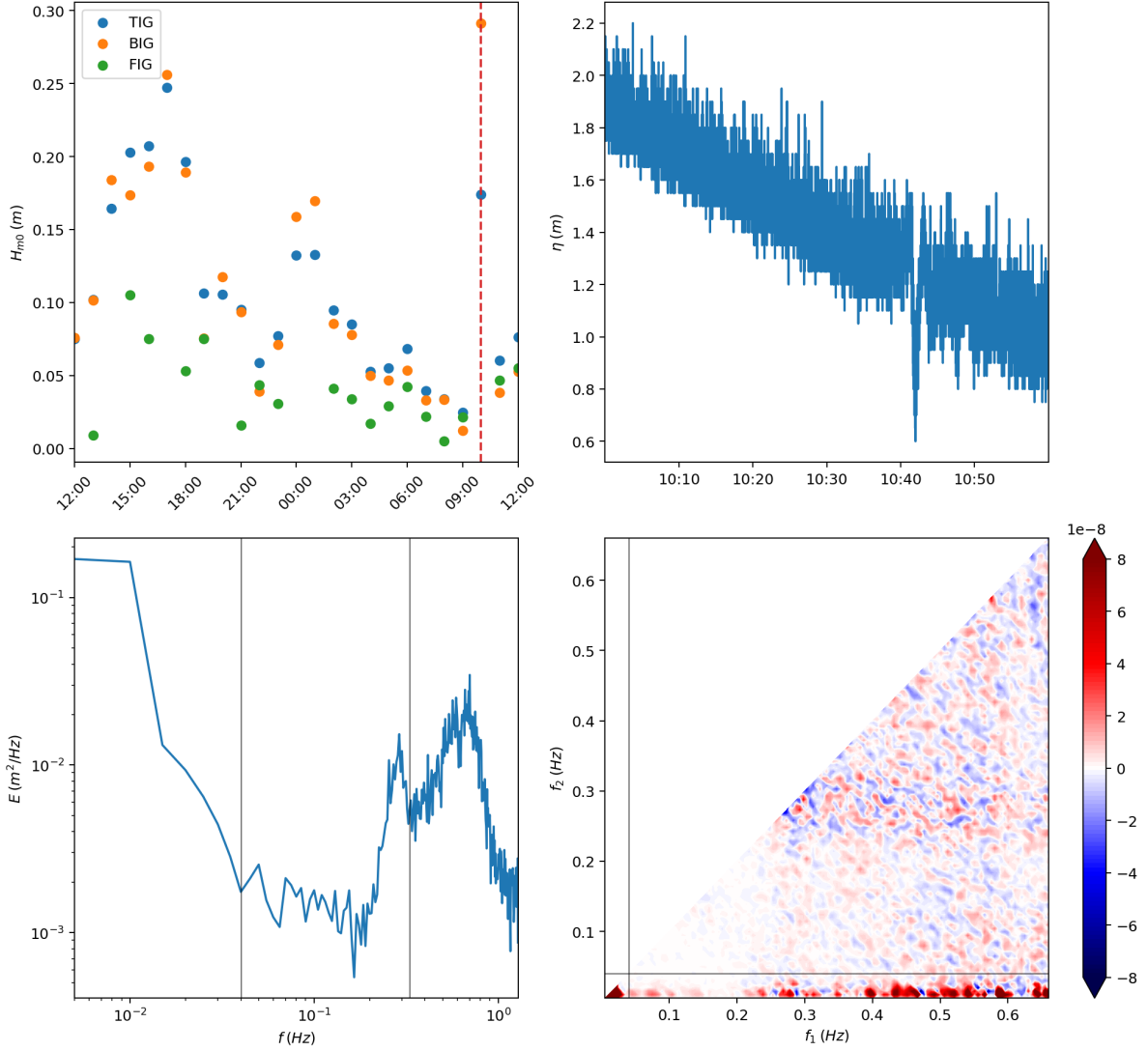


Figure 4.4: Upper left: hourly $H_{m0,TIG}$, $H_{m0,BIG}$ and $H_{m0,FIG}$ values at 011 during storm Eunice. Upper right: water elevation plot of the 19th of February, 2022 at 10:00 CET. Lower left: wave spectrum of the 19th of February, 2022 at 10:00 CET. Upper right: bispectrum of the 19th of February, 2022 at 10:00 CET

The water surface elevation plot shows a large burst shortly after 10:40. The duration of the burst is approximately 2 min, or $f = 0.008$ Hz. This corresponds to the large peak that can be seen in the plot of the wave spectrum. Interestingly, the bispectrum shows a significant energy transfer from the f_1 and f_2 to f_3 , where f_1 is the entirety of the analysed frequency band and f_2 appears to be around 0.01 Hz, or put differently, around the same frequency of the burst shown in the water elevation plot.

Unfortunately, this does not explain each instance where $H_{m0,BIG} > H_{m0,TIG}$. Figure 4.5 depicts the same type of plot for 10 hours earlier. This is another instance where $H_{m0,BIG} > H_{m0,TIG}$, but the water elevation signal does not show a similar burst as depicted in Figure 4.4. As a consequence, the wave spectrum plot does not show the large peak in the IG range and the bispectrum does not show the distinct horizontal line at the low frequency. In fact, Figure 4.5 exhibits a notable similarity to Figure 4.6, where $H_{m0,BIG}$ does not exceed $H_{m0,TIG}$. It is possible that a similar burst is present in the wave elevation signal with a lower intensity, but that is hard to prove as it cannot be concluded from a visible

inspection.

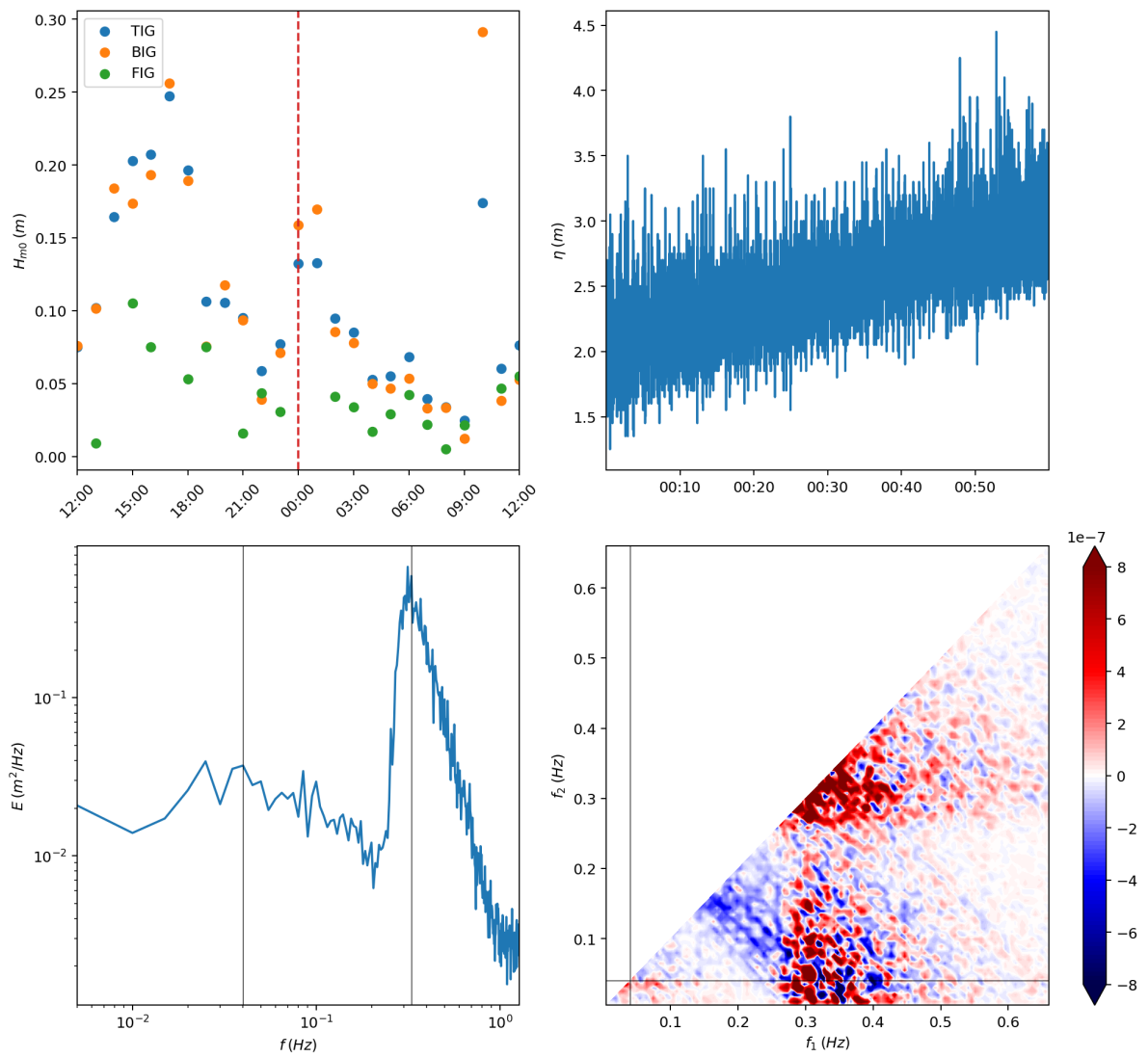


Figure 4.5: Upper left: hourly $H_{m0,TIG}$, $H_{m0,BIG}$ and $H_{m0,FIG}$ values at 011 during storm Eunice. Upper right: water elevation plot of the 19th of February, 2022 at 00:00 CET. Lower left: wave spectrum of the 19th of February, 2022 at 00:00 CET. Upper right: bispectrum of the 19th of February, 2022 at 00:00 CET

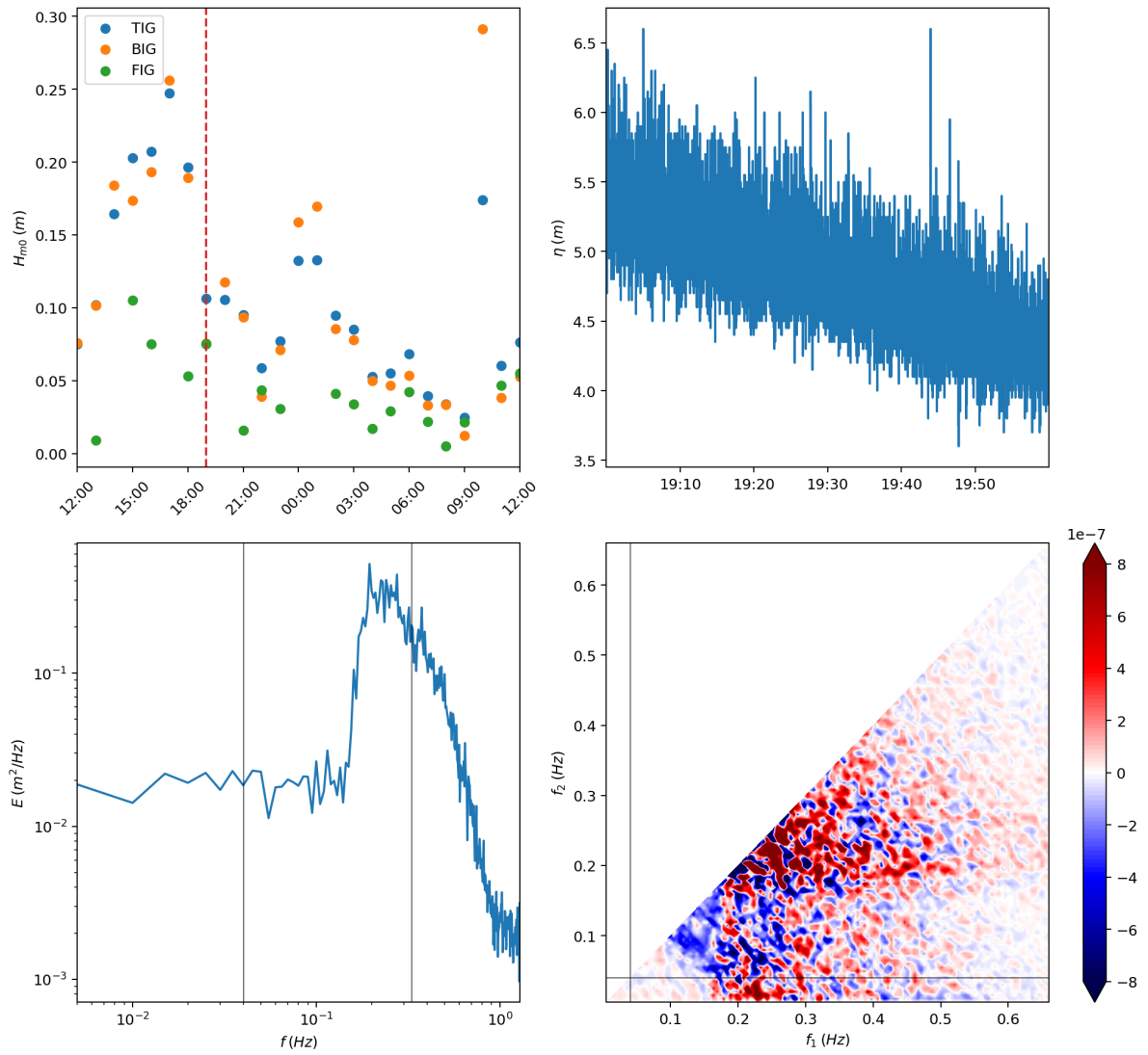


Figure 4.6: Upper left: hourly $H_{m0,TIG}$, $H_{m0,BIG}$ and $H_{m0,FIG}$ values at 011 during storm Eunice. Upper right: water elevation plot of the 19th of February, 2022 at 19:00 CET. Lower left: wave spectrum of the 19th of February, 2022 at 19:00 CET. Upper right: bispectrum of the 19th of February, 2022 at 19:00 CET

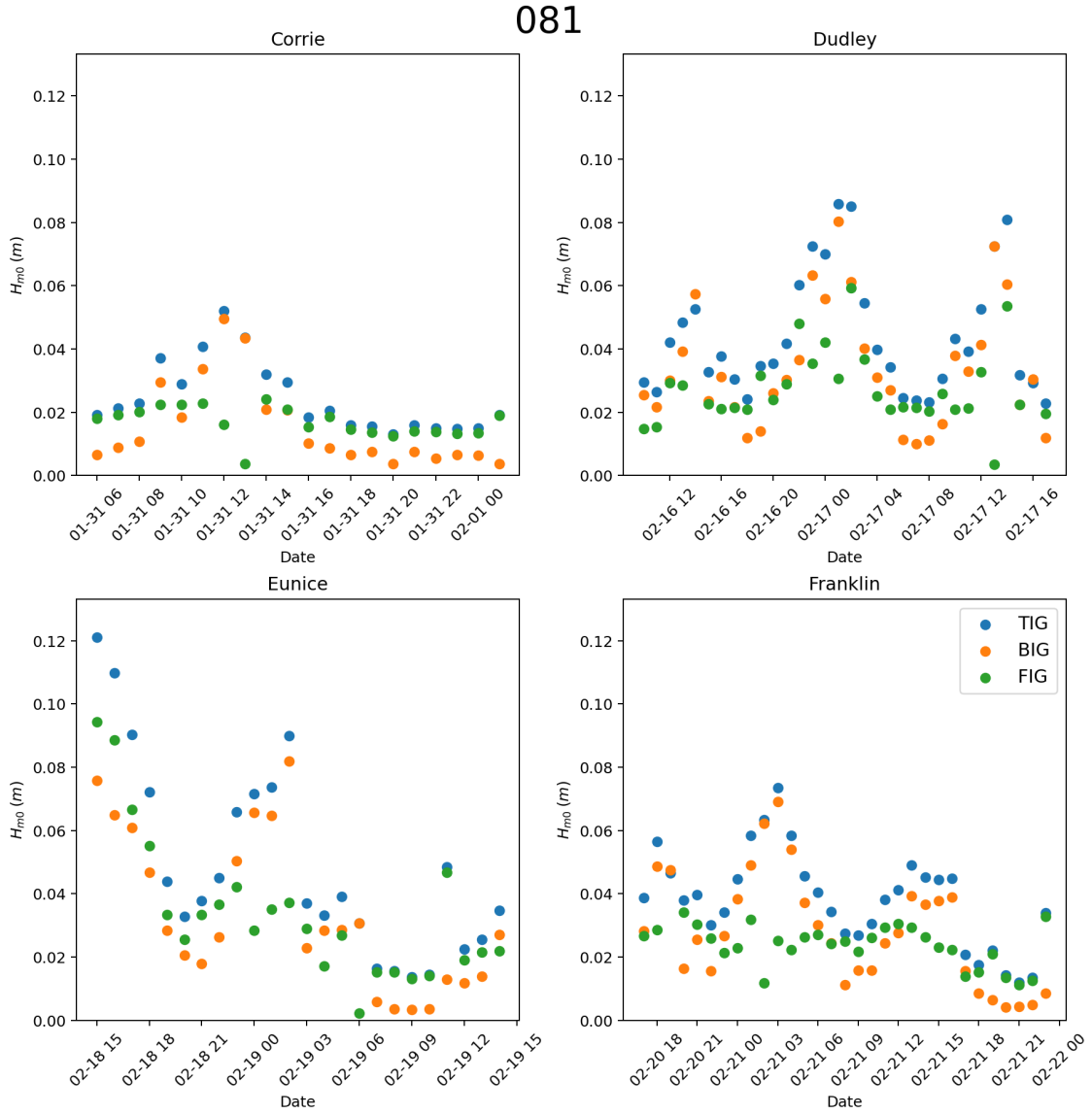


Figure 4.7: Hourly $H_{m0,TIG}$, $H_{m0,BIG}$ and $H_{m0,FIG}$ measurements at 081 during all storms

081, Hansweert

Figure 4.7 appears to show more accurate results than the findings of the bispectral analysis employed on the measurement device near Bath. Apart from 3 measurements during storm Dudley and Franklin combined, there are no occurrences where $H_{m0,TIG} < H_{m0,BIG}$. The plots are still quite erratic and it appears that the BIG wave component is more dominant than the FIG wave component. This is less of a surprise as it was when this was apparent at measurement device 011, but still noteworthy for the same reasons. It appears that most of the high energetic periods are forced by a strong BIG component, as $H_{m0,FIG} < H_{m0,BIG}$ for most of the local maxima of $H_{m0,TIG}$, except for the first local maxima during Eunice. Excluding this occurrence, it can be concluded that $H_{m0,FIG} > H_{m0,BIG}$ generally only occurs during less energetic wave events. This particularly shows during storm Dudley and Franklin. Both plots contain 3 local maxima and 3 local minima where $H_{m0,FIG} > H_{m0,BIG}$ during the local minima, but $H_{m0,FIG} < H_{m0,BIG}$ during the local maxima. It should be noted that the derived $H_{m0,IG}$ values are relatively small at 081 during all storms, compared to the measured values at the other measurement devices.

The similarity between Figure 4.3 and Figure 4.7 is significant. The magnitude of the measurements at 011 are approximately twice as large as the measurement at 081, but the shape is similar. The $H_{m0,SS}$

values at these measurement devices have a similar shape as well, which hints at a correlation. This can be seen in Figure 4.2.



Figure 4.8: Hourly $H_{m0,TIG}$, $H_{m0,BIG}$ and $H_{m0,FIG}$ measurements at 031 during all storms

031, Brouwershavense Gat 2

Figure 4.8 is the first measurement device that will be elaborated on that is not located in the Western Scheldt and that is illustrated by the magnitude of the significant wave heights. The largest $H_{m0,TIG}$ value was during storm Corrie and has a value of 0.388 m. Some data appears to be missing during storm Corrie, during which potentially higher significant IG wave heights could have been measured. This supports the hypothesis that the sheltered position of measurement devices 011 and 081 result in a lower $H_{m0,TIG}$.

It is evident that the FIG wave component is more dominant at 031 than the BIG wave component. Apparently, most of the BIG waves have dissipated through one of the dissipation mechanisms before arriving at measurement device 031.

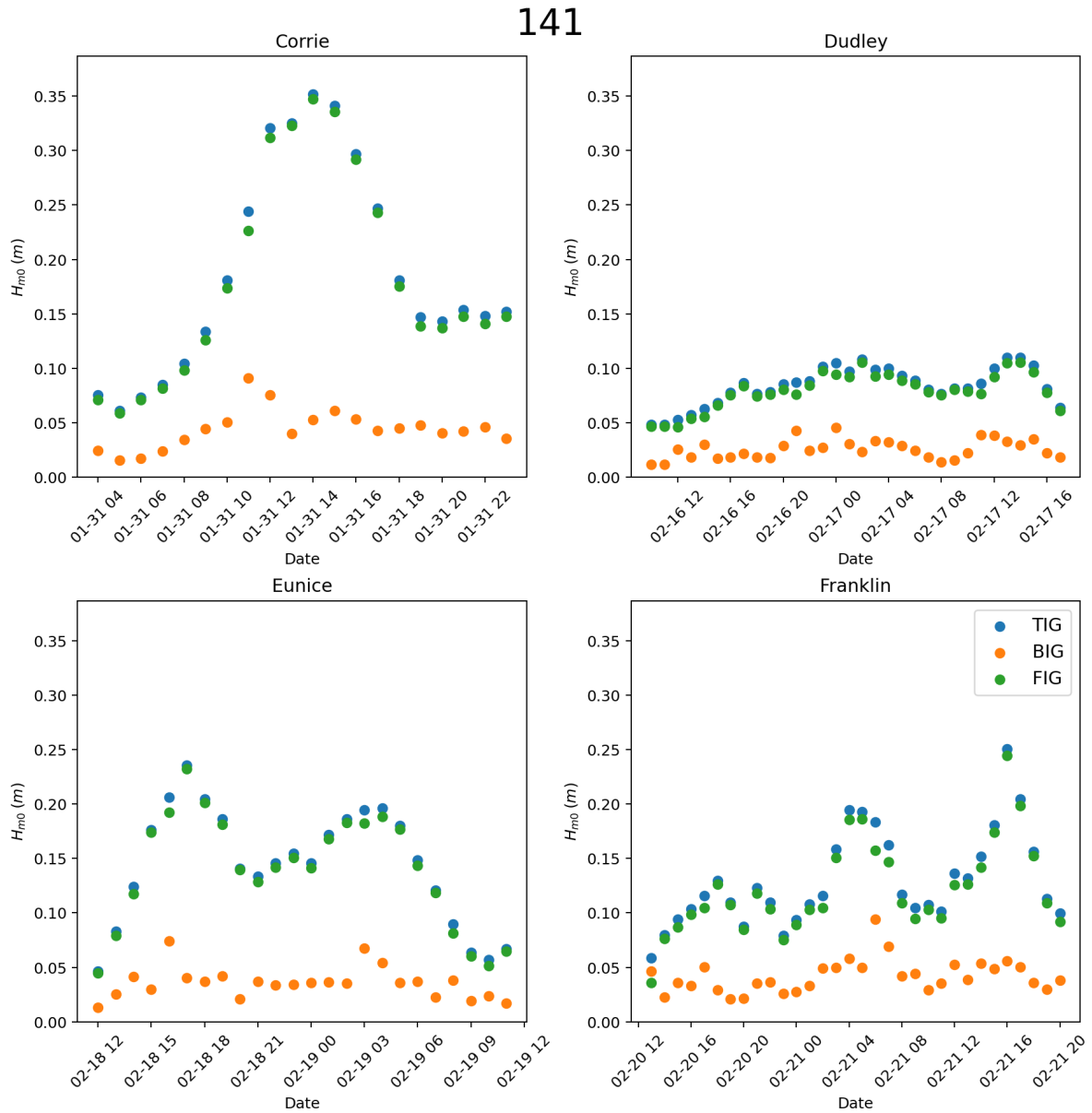


Figure 4.9: Hourly $H_{m0,TIG}$, $H_{m0,BIG}$ and $H_{m0,FIG}$ measurements at 141 during all storms

141, OS4

Figure 4.9 shows similar results as Figure 4.8. It shows that nearly all of the TIG wave energy can be attributed to the FIG wave energy. The magnitudes of the significant wave heights are all very similar. Measurement device 141 is the only measurement device that achieved a large $H_{m0,TIG}$ during storm Franklin than during storm Eunice, albeit the difference is small.

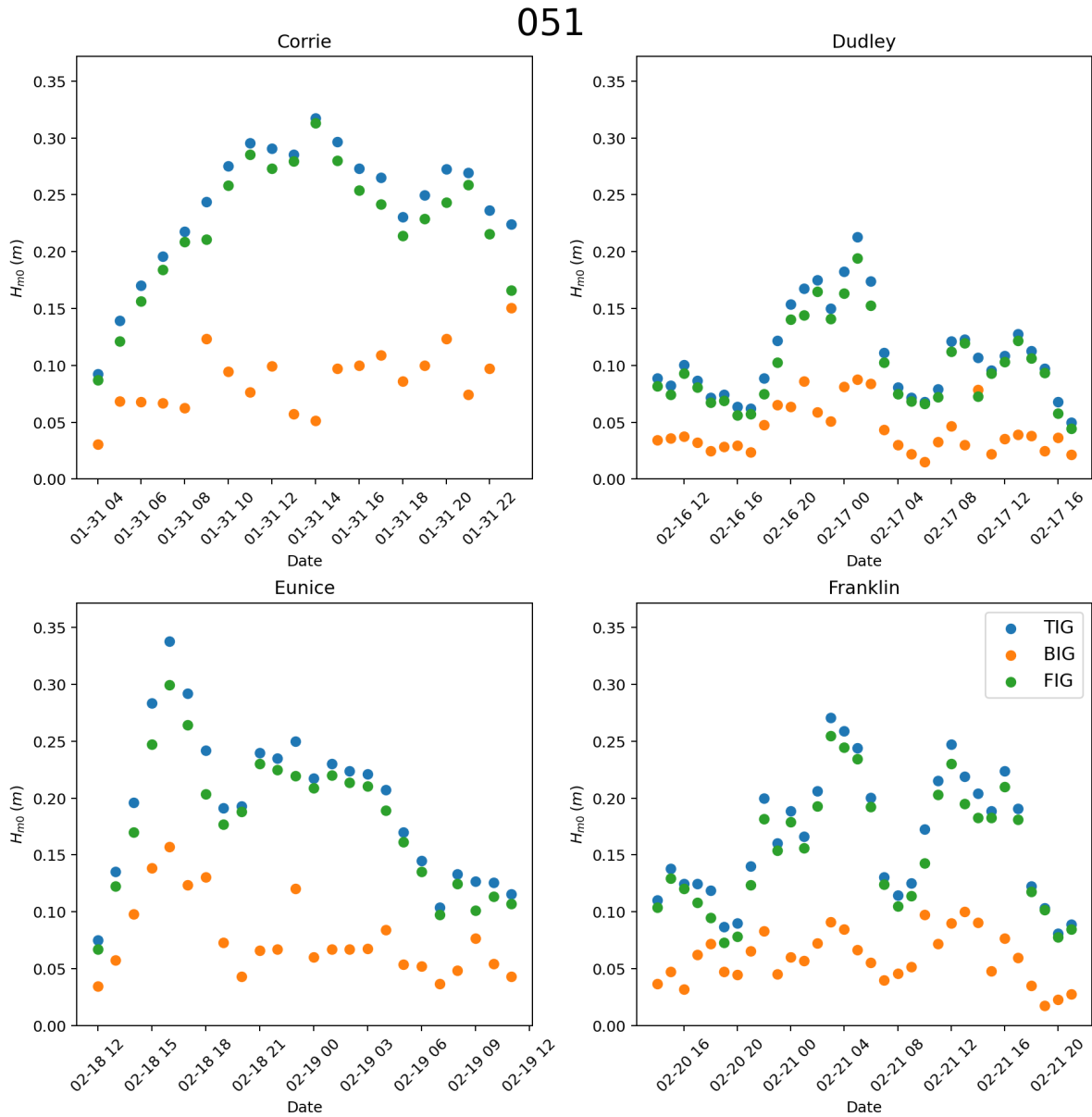


Figure 4.10: Hourly $H_{m0,TIG}$, $H_{m0,BIG}$ and $H_{m0,FIG}$ measurements at 051 during all storms

051, Cadzand

The measurement device at Cadzand registered relatively high $H_{m0,TIG}$ -values, where values of 0.25 m are exceeded during all storm except Franklin. Similar to the bispectral results of measurement devices 141 and 031, $H_{m0,FIG}$ is larger than $H_{m0,BIG}$ during all storms. Judging by the $H_{m0,BIG}$ values in relation to the $H_{m0,TIG}$ values, it appears that the BIG component contributed more towards $H_{m0,TIG}$ at 051 compared to the findings at 031 and 141.

4.1.3. Relative contribution

The relative contribution of the FIG variance to the TIG variance, thus the ratio of the FIG energy to the TIG energy, can be determined with the squared ratio of the FIG wave height over the TIG wave height, R_{FIG}^2 . This relation can be seen in Equation 4.2 and Figure 4.11 depicts the ratio during all storms at each measurement device. The dot depicts the end of a time period for the accompanying storm.

$$R_{FIG}^2 = \left(\frac{H_{m0,FIG}}{H_{m0,TIG}} \right)^2 \quad (4.2)$$

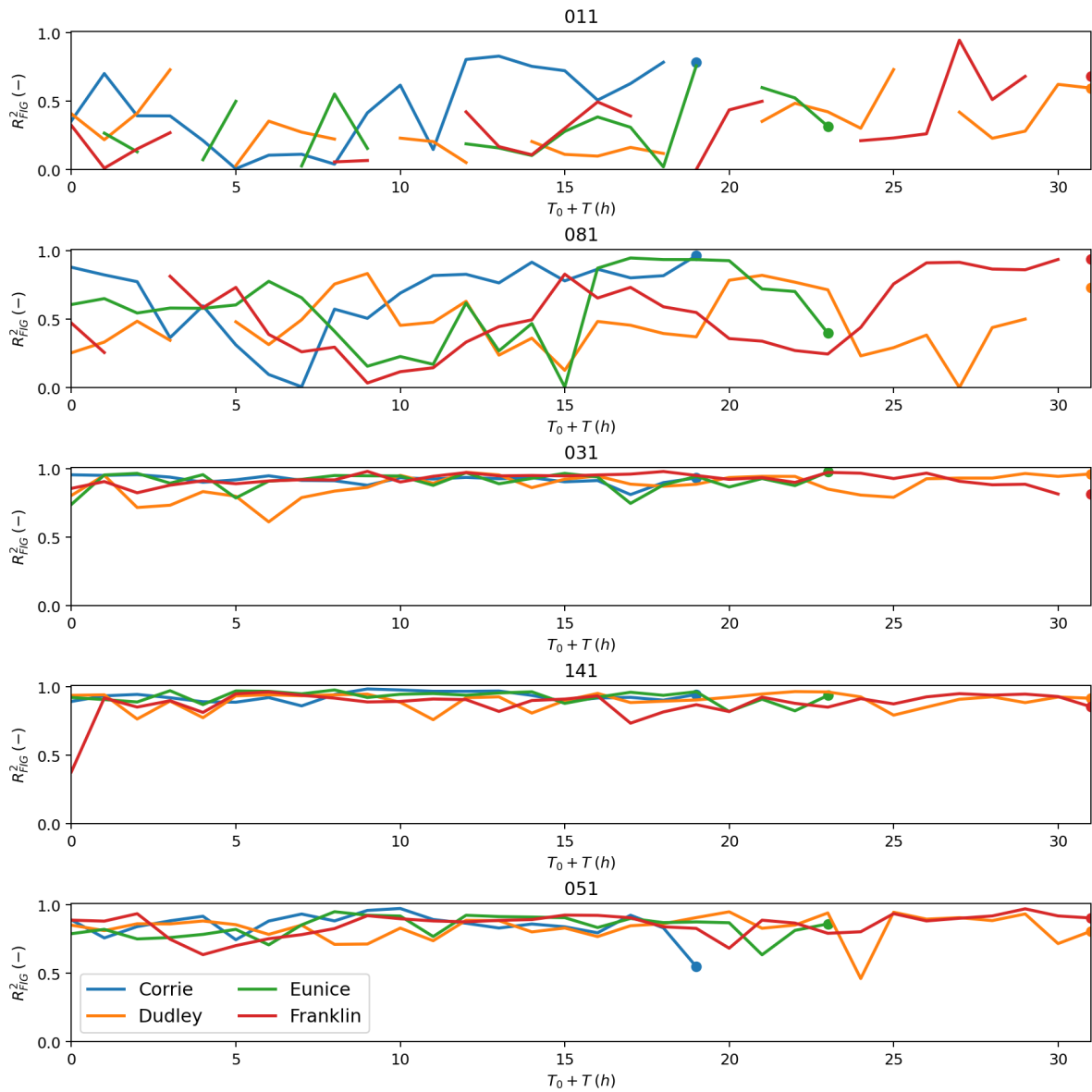


Figure 4.11: R_{FIG}^2 for each measurement during all storms, where T_0 is defined as the first hour of a storm.

Figure 4.11 shows that the FIG contribution at the measurement devices in the North Sea is dominant, while for the two sheltered measurement devices, it is mixed. In addition, the R_{FIG}^2 values of measurement device 051 are indeed slightly less than the R_{FIG}^2 values of 031 and 141, as has earlier been suggested.

4.2. SWAN results

This section contains the SWAN results. To this extent, the observed FIG wave height will be compared to the SWAN results with the use of the predictive skill. The SWAN model proved to generally under predict. This led to the implementation of reflective lines in the Western Scheldt and the outcomes were subsequently compared with the predictive skill. Finally, another perspective to assess the implementation of the reflective lines has been explored. To this extent, the Western Scheldt as a whole is plotted.

4.2.1. Devices

This section contains the SWAN results at the five output locations in the computational domain. Here, the output locations resemble the measurement locations in and around the Western Scheldt.

Default run

The model was first run without any modifications to the FIG source lines to establish a default simulation. The results of the default simulation are consequently compared to the results of the bispectral analysis, which can be seen in Figure 4.12. The plot shows the FIG wave height at each time step for all 5 locations in the Scheldt region during storm Corrie. The bispectral analysis results are shown in blue and the results of SWAN are shown in orange. It appears that SWAN generally not only underpredicts the measurements during storm Corrie, but also during the other storms. This can be concluded from Appendix E.1, which features the figures comparing the bispectral analysis results to the SWAN results of all storms.

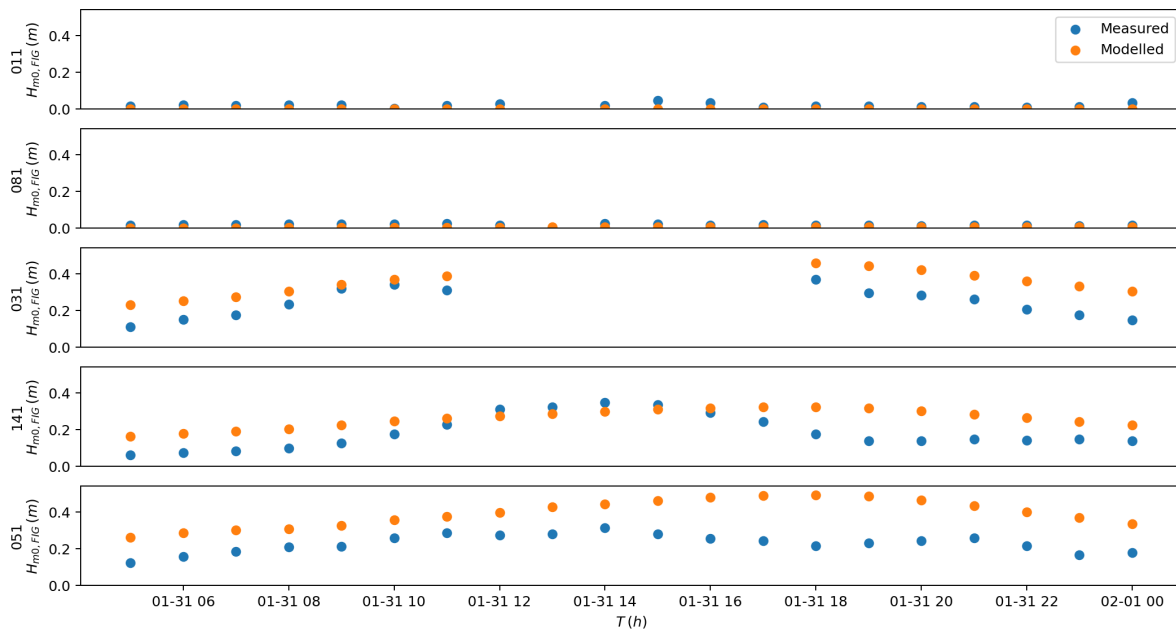


Figure 4.12: Modelling and measuring results during storm Corrie of the default run

The predictive skill can be used to investigate to what extent a model is able to reproduce measurements (Reniers et al., 2002). In this case, it will be used to quantify to what degree the SWAN model is able to replicate the findings of the bispectral analysis. Here, the predictive skill is defined as in Equation 4.3. As can be concluded from the equation, a low skill can refer to two aspects. If the model is poor, it will result in a low skill value and it appears to indicate a bad model. On the contrary, if the bispectral analysis is performed on a poor signal, the skill will be low even if the model is able to replicate reality perfectly. The predictive skill values for each measurement device during all storms can be observed in Table 4.7. The skill values for the measurement stations in the Western Scheldt, 081 and 011, are low.

$$skill = 1 - \frac{\sqrt{\frac{1}{N} \sum_{i=1}^N (H_{FIG,B}^i - H_{FIG,S}^i)^2}}{\sqrt{\frac{1}{N} \sum_{i=1}^N (H_{FIG,B}^i)^2}} \quad (4.3)$$

	051	081	011	031	141
Corrie	0.6466	0.0009	0.0	0.5044	0.3327
Dudley	0.7510	0.0004	0.0	0.6565	0.4293
Eunice	0.6762	0.0003	0.0	0.5171	0.3497
Franklin	0.6530	0.0006	0.0	0.5394	0.3408

Table 4.7: Predictive skill values during different storms for different output locations excluding the reflection lines

Inclusion of a reflective line

In an attempt to ensure that more FIG wave energy propagates into the Western Scheldt, a practical approach will be used. In SWAN, a line can be specified with is able to reflect incoming waves. To accommodate this, a reflection coefficient is used, where $R = 1$ equals full reflection. These lines are implemented into the model along the coastline of the Western Scheldt at a distance of a few grid cells. Similar to the FIG source lines, the reflective lines are also non-transmissible. To account for this, two openings are created to interrupt the reflection line, in order to allow FIG energy to reach the locations of the measurement devices. The configuration of these lines can be seen in Figure 4.13. The depth of the Western Scheldt is also shown in this figure. The reflective lines are placed at depths ranging from approximately 0 m to 20 m. The wide range is a result of the distance to the coast being deemed more important than the depth in which the lines are placed. The predictive skill values for the SWAN simulation with reflective lines can be found in Table 4.8.

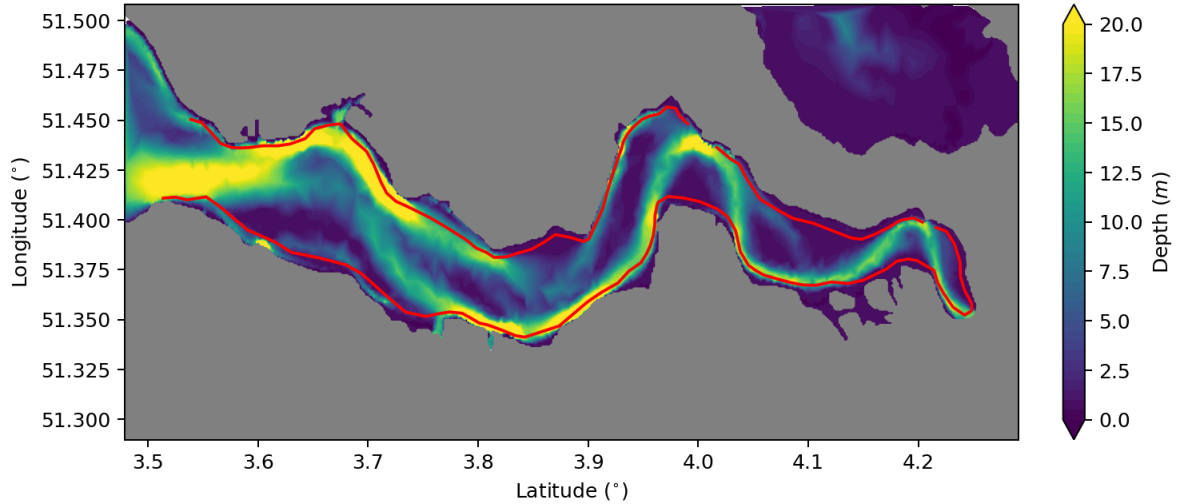


Figure 4.13: Reflective lines configuration in the Western Scheldt

	051	081	011	031	141
Corrie	0.6469	0.0037	0.0	0.5044	0.3327
Dudley	0.7513	0.0016	0.0	0.6566	0.4293
Eunice	0.6769	0.0013	0.0	0.5172	0.3497
Franklin	0.6535	0.0022	0.0	0.5394	0.3409

Table 4.8: Predictive skill values during different storms for different output locations including the reflection lines

No increase can be found for the skill at the most eastern location, 011. This can be attributed to FIG wave heights of 0 m for all time steps due to the nature of Equation 4.3. Additionally, very little change

has been detected for the skill for the two locations located near the Eastern Scheldt Storm Surge Barrier, 141 and 031 and Cadzand, 051. The only increase of skill that is moderately substantial is the remaining location, 081. Here, the skill for the simulations with the reflective lines is approximately 4 times as high compared to the simulations without the reflective lines. The skill is, however, still insignificant.

4.2.2. Spatial

Another way of looking at the FIG propagation in the Western Scheldt is by plotting it in the estuary directly. This has been facilitated by the creation of a rectangular grid in the Western Scheldt where a variance density spectrum is requested at each grid node. The FIG wave height in the Western Scheldt can then be obtained by double integrating the wave spectra for each node.

This has been done for the simulations with and without the reflective lines. The difference proves to be small, thus it is thought to be more clear to include the difference ($\Delta H_{m0,FIG} = H_{m0,FIG,Inc} - H_{m0,FIG,Exc}$) between the simulation results. These can be seen in Figure Figure 4.14, Figure 4.15, Figure 4.16 and Figure 4.17. Depicted is the Western Scheldt for the hour in which the largest $\Delta H_{m0,FIG}$ value has been documented for each storm. Table 4.9 shows the hour and the magnitude of the maximum difference for each storm. For the figures depicting the $H_{m0,FIG}$ values of the simulations including and excluding the reflective lines, please refer to Appendix F.

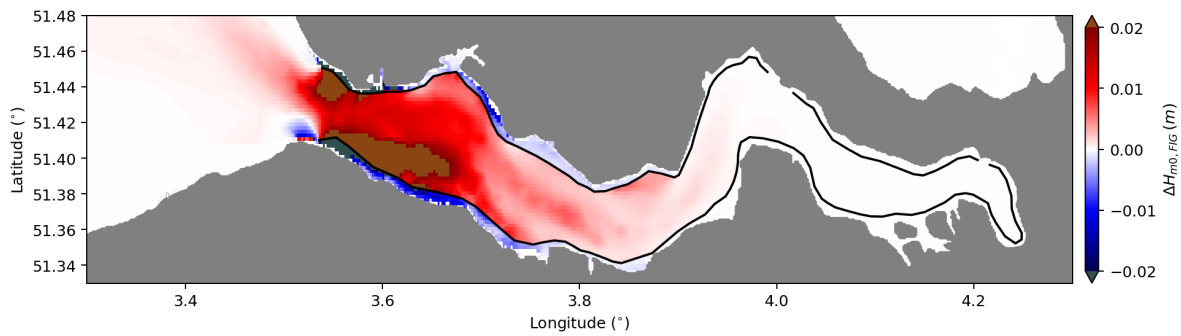


Figure 4.14: Snapshot of the hour where the largest $\Delta H_{m0,FIG}$ value is found during storm Corrie

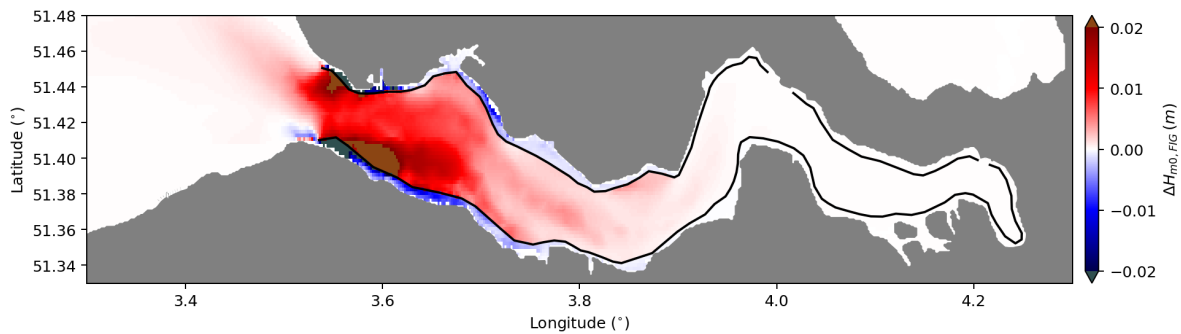


Figure 4.15: Snapshot of the hour where the largest $\Delta H_{m0,FIG}$ value is found during storm Dudley

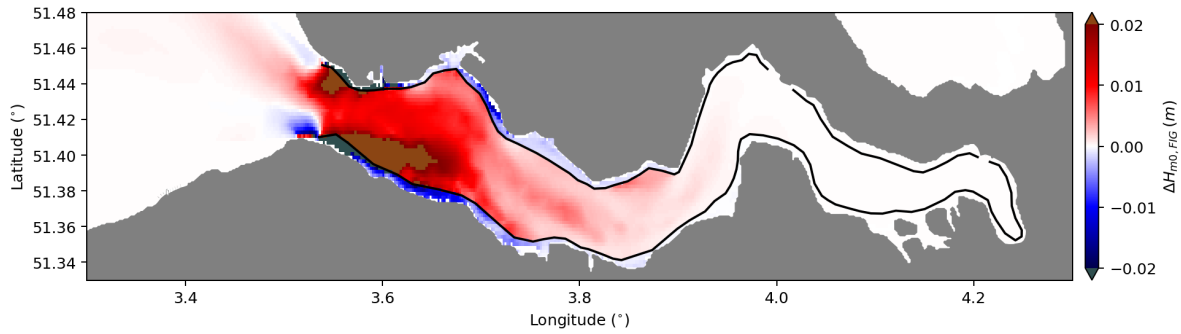


Figure 4.16: Snapshot of the hour where the largest $\Delta H_{m0,FIG}$ value is found during storm Eunice

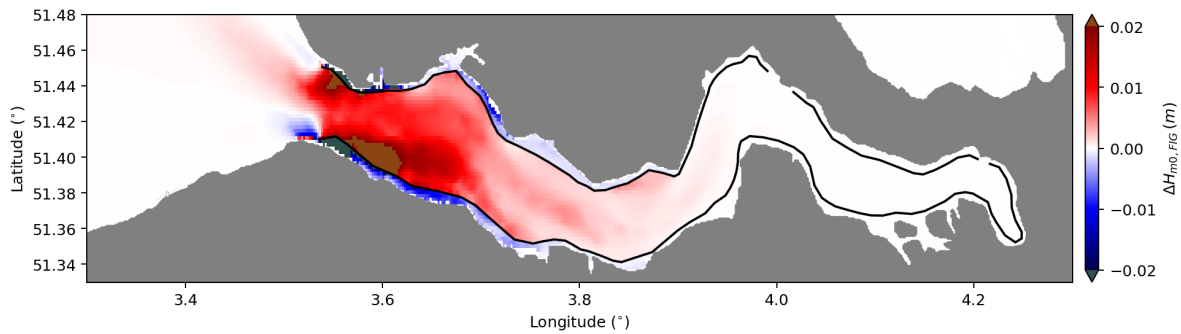


Figure 4.17: Snapshot of the hour where the largest $\Delta H_{m0,FIG}$ value is found during storm Franklin

Positive values indicate instances where the inclusion of the reflective lines results in larger FIG wave heights in the Western Scheldt. Storm Corrie and storm Eunice contain the largest difference between the simulations with and without the reflective lines, according to Table 4.9. This is suggested by the figures as well, as the total area that is brown is the largest in Figure 4.14 and Figure 4.16. The areas where the $\Delta H_{m0,FIG}$ values exceed 0.02 m are located in front of the municipalities Sluis and Vlissingen for all storms

Storm	Absolute	
	Hour	Magnitude
Corrie	15 th	0.065 m
Dudley	14 th	0.044 m
Eunice	8 th	0.058 m
Franklin	10 th	0.046 m

Table 4.9: Summary of $\Delta H_{m0,FIG}$ values

The figures also contains pixel representing a negative change. Most of the pixels representing a decrease of the FIG wave height are located on the shoreward side of the reflective lines. This can be attributed to the non-transmissible property of the reflective lines as defined in SWAN. The only exception is at Schoneveld, near the mouth of the Western Scheldt.

The relative change ($H_{m0,FIG,Inc}/H_{m0,FIG,Exc}$) as a consequence of the reflective lines will be used to investigate the significance of the implementation. These plots look similar to the plots depicting the absolute change. Next to the plots showing the relative change instead of the absolute change, there is one additional alteration implemented here. The relative change in a cell is only plotted if the $H_{m0,FIG}$ value in the cell is larger than 0.01 m for the simulation without the reflective lines. The rationale behind this is that a small absolute increase of $H_{m0,FIG}$ at these cells can quickly result to large relative

changes, thus skewing the perception of the spatial plot. Figure 4.18, Figure 4.19, Figure 4.20 and Figure 4.21 depict the relative change for the hour during which the maximum absolute change has been documented for each storm. The plots show a similarity to Figure 4.14, 4.15, 4.16 and 4.17. The yellow cells in the plot show that there are locations in the Western Scheldt where the $H_{m0,FIG}$ values have doubled due to the implementation of the reflective lines, thus proving that the implementation is significant at certain locations.

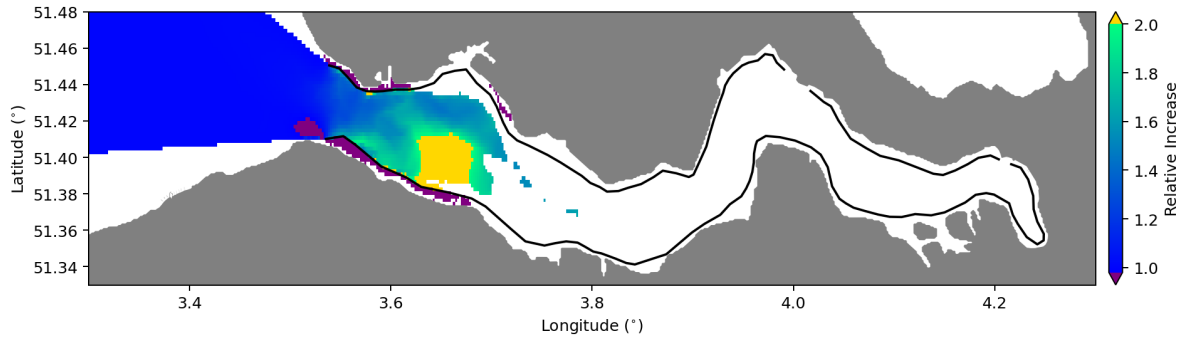


Figure 4.18: Snapshot of the relative change of the hour where the largest $\Delta H_{m0,FIG}$ value is found during storm Corrie

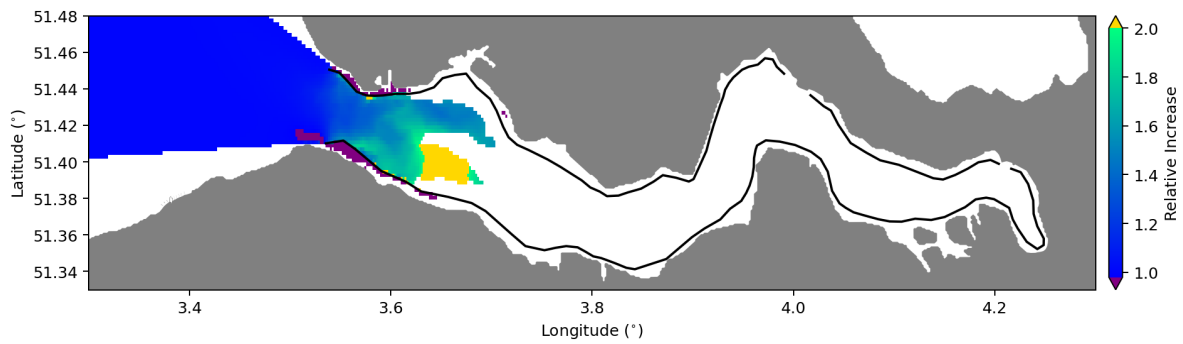


Figure 4.19: Snapshot of the relative change of the hour where the largest $\Delta H_{m0,FIG}$ value is found during storm Dudley

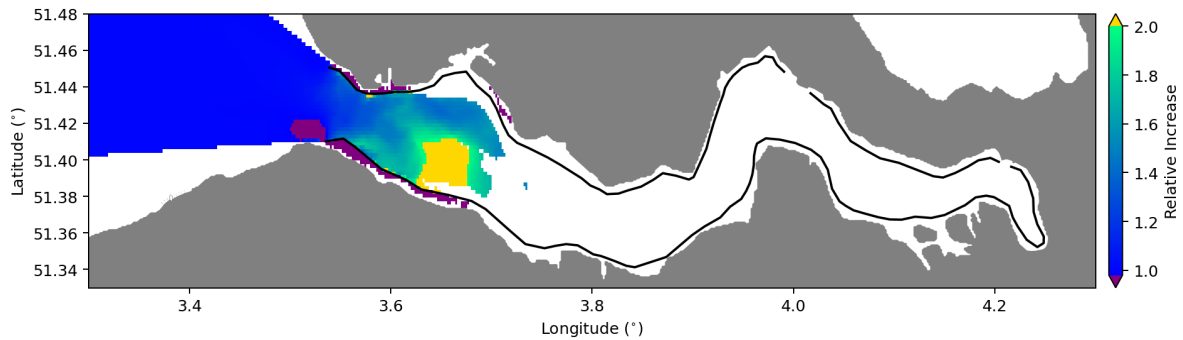


Figure 4.20: Snapshot of the relative change of the hour where the largest $\Delta H_{m0,FIG}$ value is found during storm Eunice

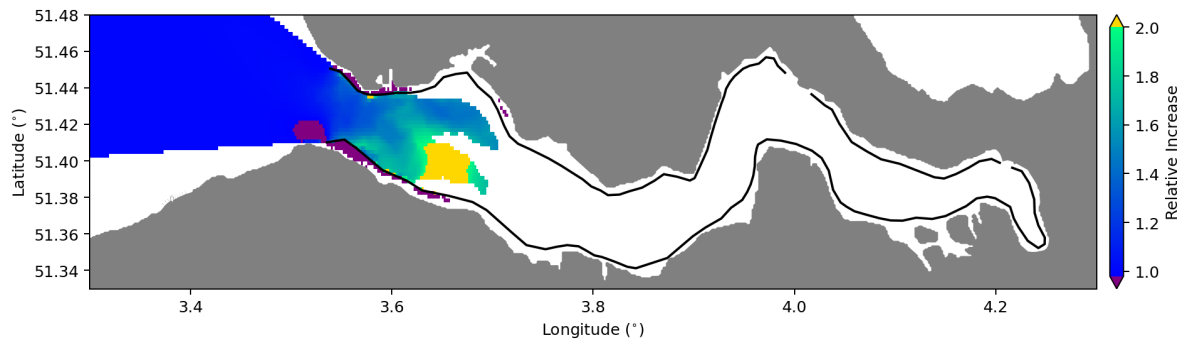


Figure 4.21: Snapshot of the relative change of the hour where the largest $\Delta H_{m0,FIG}$ value is found during storm Franklin

5

Discussion

The model used in this study provides insight into the propagation of FIG wave in the Western Scheldt. The physics encompassed in the model are a simplified version of reality. This allows the model to run in a more efficient manner as it used less computational resources. This inherently lead to inaccuracies between model results and measurements. Similarly, the limitations of the measurement devices are a potential source of discrepancies between the model results and the measurements.

5.1. Model limitations

5.1.1. α_1 value

The α_1 value is the dimensional coefficient that relates the incident SS waves to the reflected FIG waves and it varies from one site to another (Ardhuin, Rawat, & Aucan, 2014). The α_1 values used in this study originate from a calibration performed on measurement results of the Zandmotor. Although close on a global scale, the distance between the Zandmotor and the closest measurement device, 031, is still approximately 50 km. Better skill values are expected if α_1 values were calibrated on the measurement devices used in this study. Given the general under prediction in the of the measurement result, larger α_1 values are suggested for most of the FIG source lines.

5.1.2. Friction coefficient

The orbital motions of the water particles are capable to reaching the bottom of the seafloor in shallow waters. This links the friction encountered at the seafloor to the surface waves. The friction coefficient used in this study, χ , is constant for the entire computational domain. The actual bottom friction is based various physical processes and properties such as the grain size and the dynamic shape of the bottom. This allows SWAN to run in a more efficient manner, but might leads to some inaccuracies.

5.1.3. Reflection lines

The reflection lines in the Western Scheldt were implemented to ensure that more IG energy is able to propagate into the Western Scheldt, as the model under predicts the bispectral analysis results. The implementation implied full reflection ($R = 1$) and no FIG generation according to the Ardhuin, Rawat, and Aucan (2014) parametrization ($\alpha_1 = 0$). This was justified by assuming that the amount of BIG energy that is capable of propagating that far up the Western Scheldt is insignificant. The bispectral analysis results, in particular the figure displaying the FIG to TIG ratio, Figure 4.11, suggests that this assumption is invalid. Consequently, it could be beneficial to investigate if a nonzero α_1 value results in better skill values for measurement device 011 and 081.

5.1.4. Other FIG sources

The FIG source used in this model is based on the findings of Ardhuin, Rawat, and Aucan (2014). It symbolizes the exchange of wave energy from the incident SS waves to the reflected FIG waves. In reality, there are other FIG wave generation mechanics, such as distantly reflected FIG waves entering the Scheldt region. These can be reflected at one of the coasts included in the model or even coasts that are not included in the model. For both cases stands that these FIG waves are not included in the model, while they are in the measurements. This could be a contribution to the general under prediction of the FIG wave height my the model, compared to the measurement results.

5.1.5. Positioning of Cadzand

The actual location of the measurement device at Cadzand is located at a point where significant shoaling has occurred. The parametrization of (Ardhuin, Rawat, & Aucan, 2014) works best sites where no wave dissipation has occurred, thus outside the surfzone. This translates to an FIG source line in the model located seaward of the output location of Cadzand, thus not at a location receptive to FIG wave energy. The change of the location of Cadzand was therefore mandatory as the alternative was modifying the FIG source line. The latter can lead to two consequences. The FIG source line could be redrawn near Cadzand in such a way that the output location of Cadzand is on the seaward side of the FIG source line. This would lead to the undesired effect where nearly no FIG wave energy is radiated outward for this section, as a significant segment of the waves in the SS frequency band is expected have been dissipated at this point. The other option is leaving out the section of the FIG source line where Cadzand is located, but this modification was also dismissed as it is expected to result in less FIG energy at all other locations, as this section could be a significant FIG energy source due to its proximity to the output locations. While close on a global scale, this change of location is expected to result in some inaccuracies between the bispectral analysis results and the SWAN model output.

5.2. Measurement limitations

5.2.1. Locations of measurement devices

The 5 measurement devices are spaced around the Scheldt region. The skill values of the 5 measurement devices can be divided in 2 groups. The devices located in the North Sea show a skill value of moderate significance. The devices in the Western Scheldt show a skill value of (almost) no significance. It would have been useful if a measurement device was located more towards the mouth of the Western Scheldt. The measurements of this fictional device and the accompanying skill value would provide context regarding the poor skill values at the back of the Western Scheldt.

The magnitude of the skill values of the hypothetical measurement device could have a magnitude between the skill values of the 2 groups. This could hint at the bottom friction being too strong, as too much dissipation has occurred. If the skill value is similar to either one of the two groups, it could hint at an area in the Western Scheldt where more dissipation occurs than expected.

5.2.2. Bispectral analysis

The bispectral analysis is a method used on a time signal to investigate the coupling of frequencies. In this study it has been used to calculate the ratio of the BIG waves to the TIG waves. The ratio was used to calculate the FIG wave height at the measurement devices. A bispectral analysis is susceptible to by factors such as noise, non-stationarity and the presence of outliers. Steps were performed in this study to minimize the effects of these phenomena, but fully removing them is hard to achieve.

The dominant source of errors in the bispectral estimates is the statistical uncertainty. In particular, the statistical uncertainty in bispectral estimates is relatively large when the nonlinearity is weak. In other words, estimates of $E_{bound}(\Delta f)$ based on Equation 2.17 are expected to be inaccurate if free waves dominate the IG spectrum (Herbers, Elgar, & Guza, 1994). This complicates the findings of the bispectral analysis. The discrepancies in the bispectral analysis results for measurement device 011 during storm Dudley, Eunice and Franklin could be attributed to a large FIG dominance at this location. The FIG dominance is not measured, but suspected, as has already been elaborated. Similarly, the bispectral analysis results for measurement device 031, 141 and 051 show a large FIG dominance. This would mean an inaccurate result, given the statement by Herbers, Elgar, and Guza (1994).

6

Conclusion

Infragravity waves are a section in the total wave spectrum that could provide a significant contribution towards the wave field. The objective of this study was to provide insight into their characteristics in the Scheldt region and to assess to what extent they can be modelled with SWAN. To achieve this, measurements at 5 locations around the Scheldt region were compared to the results of a SWAN model. The wave data was provided by Rijkswaterstaat and the time periods are derived from 4 storms named Corrie, Dudley, Eunice and Franklin, that occurred during January and February in 2022.

6.1. IG wave characteristics in the Scheldt region

The 5 measurement devices are located near the Eastern Scheldt Storm Surge Barrier (031 and 141), Cadzand (051), Hansweert (051) and Bath (011). The data was provided by Rijkswaterstaat and underwent a bispectral analysis in hourly records. Using the infragravity boundary bands of 0.005 Hz and 0.04 Hz, this resulted in a bound IG (BIG) wave height to total IG (TIG) wave height ratio, facilitating the derivation of free IG (FIG) wave height.

The 5 measurement devices can be divided in 2 groups based on their location. Measurement devices 031, 141, and 051 are located in the North Sea. The remaining two measurement devices, 081 and 011, are located in the Western Scheldt. One key difference between the groups is that the former group contains measurement devices that are relatively exposed while the measurement devices in the latter group are more sheltered. This shows when looking at the results of the bispectral analysis.

The result of the bispectral analysis for measurement device 011 are questionable for storm Dudley, Eunice and Franklin as there are a significant amount of data points where $H_{m0,BIG}$ exceeds $H_{m0,TIG}$, which is physically impossible. The bispectral results of storm Corrie at measurement device 011 and all storms at measurement device 081 register not a single $H_{m0,TIG}$ -value larger than 0.12 m. In contrast, during all storms measurement device 031, 141 and 051 register at least one $H_{m0,TIG}$ value larger than 0.10 m, and all but two contain a data point surpassing 0.20 m. Thus showing that the more sheltered locations in the Western Scheldt measurement devices indeed measure in lower TIG wave heights. This would be invalidated if storm Dudley, Eunice and Franklin at measurement device 011 were taken into account, but the authenticity of the bispectral analysis results is uncertain. However, the IG frequency range of the energy density plots derived from a regular spectral analysis show that the energy density at 011 is close to the energy density at measurement device 141, especially during storm Dudley and Eunice. This could be a sign that the instances where $H_{m0,TIG} > H_{m0,BIG}$ are valid measurements, even if the occasions where $H_{m0,TIG} < H_{m0,BIG}$ are not.

The energy ratio of FIG waves to TIG waves is remarkable. The funnel like shape and the bathymetry of the Western Scheldt suggest that the dominant IG wave energy would be FIG. The BIG energy is expected to have dissipated or transferred into FIG energy before reaching the measurement devices. However, this cannot be concluded from the findings. Figure 4.11 shows erratic lines in the plot resembling the R_{FIG}^2 values for measurement device 011 and 081, suggesting that the origin of the IG wave contributions at these locations fluctuate rapidly. For the measurement devices located in the North Sea, it appears that the FIG contribution towards the TIG wave energy is very dominant. The R_{FIG}^2 values exceed 0.8 for most of the data points for these measurement devices, especially at 031 and 141.

6.2. FIG wave modelling in the Scheldt region

The SWAN model used an unstructured grid and simulated waves in the frequency range from 0.005 Hz to 0.04 Hz, similar to the boundaries used for the bispectral analysis. The spectral directions cover a full circle, in bins of 5° and as input data for the parametrization by [Ardhuin, Rawat, and Aucan \(2014\)](#), H_{m0} and T_{m-10} were used, which were retrieved from [European Union-Copernicus Marine Service \(2019\)](#). The SWAN outputs are 2D frequency-direction spectra. These were integrated twice to calculate the variance, which was consequently used to compute the FIG wave height.

The SWAN results were first analysed with the use of the predictive skill and subsequently a spatial perspective was added. The predictive skill provided mixed results. The values of the skill of the three measurement devices located in the North Sea are moderate to satisfactory. The measurement device with the largest skill values is 051, which corresponds to the output located that was moved due to the limitations of the FIG source line. It should be noted that the relatively large skill value can be attributed to the output location, as it was moved to a location where more wave energy can be expected. The consecutive output locations based on the skill values are 031 and 141. The skill values for these three devices, during all storms range between 0.7510 to 0.3327.

The remaining two output locations, resembling 081 and 011, show less promising results. The former shows skill values ranging between 0.0003 to 0.0009, which is insignificant. This is even less for the latter, as the skill values during all storms for 011 are equivalent to 0. It appears that nearly all FIG wave energy that travels into the Western Scheldt is dissipated according to the SWAN results, which is a remarkable mismatch.

Reflective lines were implemented along the coast of the Western Scheldt in an attempt to artificially force more FIG energy into the Western Scheldt. It proved effective, albeit not to the desired degree. It appears that the skill value for the output location of measurement device 081 during all storms increased by a factor of approximately 4. While this appears significant, it means that the skill at this location is still smaller than 0.004 for all storms. In addition, the skill value of the output location representing measurement device 011 did not increase, thus stayed 0 for all storms. The reflective lines were not implemented to increase the skill of the remaining measurement device. Yet, improvements occurred in certain instances, albeit the increase is still $\mathcal{O}(0.0001)$. It turns out that the inclusion of the reflective lines is not a fitting method for increasing the skill of the SWAN model significantly. The spatial perspective was subsequently used to investigate to what extent the inclusion of the reflective lines resulted in an increase of $H_{m0,FIG}$ in the entire Western Scheldt. The added value of the reflective lines appears to be mostly for the most western part of the Western Scheldt, near the mouth. The inclusion of the reflective lines at this location results in an increase of $\mathcal{O}(0.01\text{ m})$.

7

Recommendations

The contribution of the FIG source lines along the North Sea basin are likely of different magnitudes. It would be useful to investigate which FIG source line contributes to what extent to the FIG wave energy in the Western Scheldt.

The direction of the FIG wave energy can also be examined using SWAN. Equation 7.1 can be used to make a distinction between remotely and locally reflected FIG waves. Here, θ_p represents the angle perpendicular to the nearby FIG source line. This would provide insight into whether the FIG energy at an output location is generated locally or remotely.

$$H_{FIG}^+ = 4 \sqrt{\int_{0.005}^{0.04} \int_{\theta_p-90^\circ}^{\theta_p+90^\circ} E_{FIG}(f, \theta) d\theta df} \quad (7.1)$$

All measurement devices used in this study are stepping gauges. These devices are limited to measuring water level elevations. Consequently, the origin of the measured IG waves cannot be derived from the measurements. Using a device that is able to determine the direction could therefore be used to correctly quantify peak directions. The advantage of the directional information is that the SWAN model can then be evaluated on that aspect as well. This can lead to a more accurate SWAN model.

The shortcomings of the SWAN model used in this study can partially be attributed to the α_1 values of the FIG source lines. The upside of the relatively low skill values is that there is substantial potential for improvement. This can be achieved by performing a calibration procedure on these parameters in the Scheldt region, instead. Similarly, the friction value χ can be modified in a calibration procedure. Now, this has been taken as a constant, but it could be useful to investigate the implementation of a grid representing the local χ values. It might be difficult to obtain such a grid for the North Sea basin due to its size. For the Western Scheldt, this appears more feasible. Deducing the friction coefficient based on the local bottom characteristics can lead to a better SWAN model, especially as this is close to the output locations used in this study.

This study did not go into the validation of the SWAN model, but this would be a sensible next step to perform in obtaining a SWAN model representing the FIG wave propagation near the Scheldt region. This requires an independent dataset. In addition, the number of storms used for this study is thought to be too small to perform a meaningful validation of the SWAN model.

A more in depth study regarding IG waves in the Scheldt region is warranted. This study mainly entailed the hydrodynamic aspect of these long waves in the estuarine environment. To this extent, no assessment has been done on the impact of these waves on the flood defences in the area. The measurement stations at the back of the Western Scheldt registered small IG wave heights. These limited IG waves ($\mathcal{O}(0.1\text{ m})$) are unlikely to pose any significant threat to the dikes. The largest IG waves measured near the Eastern Scheldt Storm Surge Barrier are more significant ($\mathcal{O}(0.3\text{ m})$). An assessment of their influence on the morphodynamics in the region could prove to be very insightful. IG waves are able to propagate further onshore compared to SS waves and are therefore able to cause slumping of a dune front (Roelvink et al., 2009). The measurement device near Cadzand, 051, is located close to shore and the dunes in the area are susceptible to this mechanism given that $H_{m0,IG}$ values exceeding 0.3 m are recorded. Similar findings can be expected for the dunes on the eastern coast of Walcheren

as it is located between the measurement devices documenting the relatively high (> 0.3 m) $H_{m0,IG}$ values, but it cannot be confirmed by this study given the absence of a measurement device at this coast.

A

Data selection

A.1. Storm selection

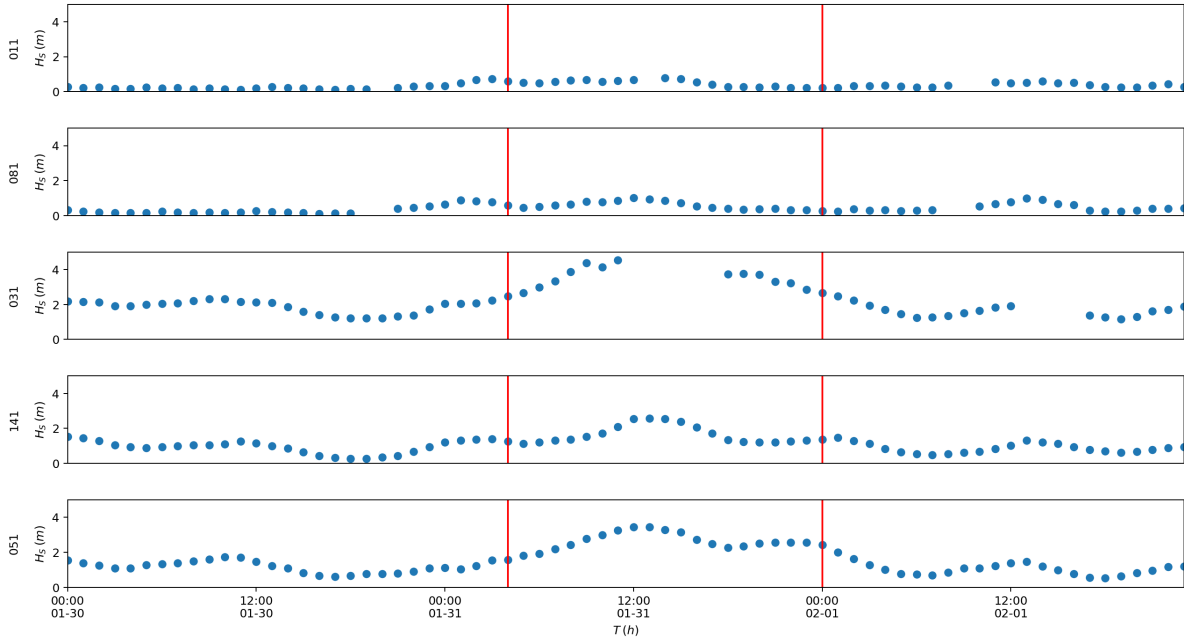


Figure A.1: Significant wave height plot during storm Corrie

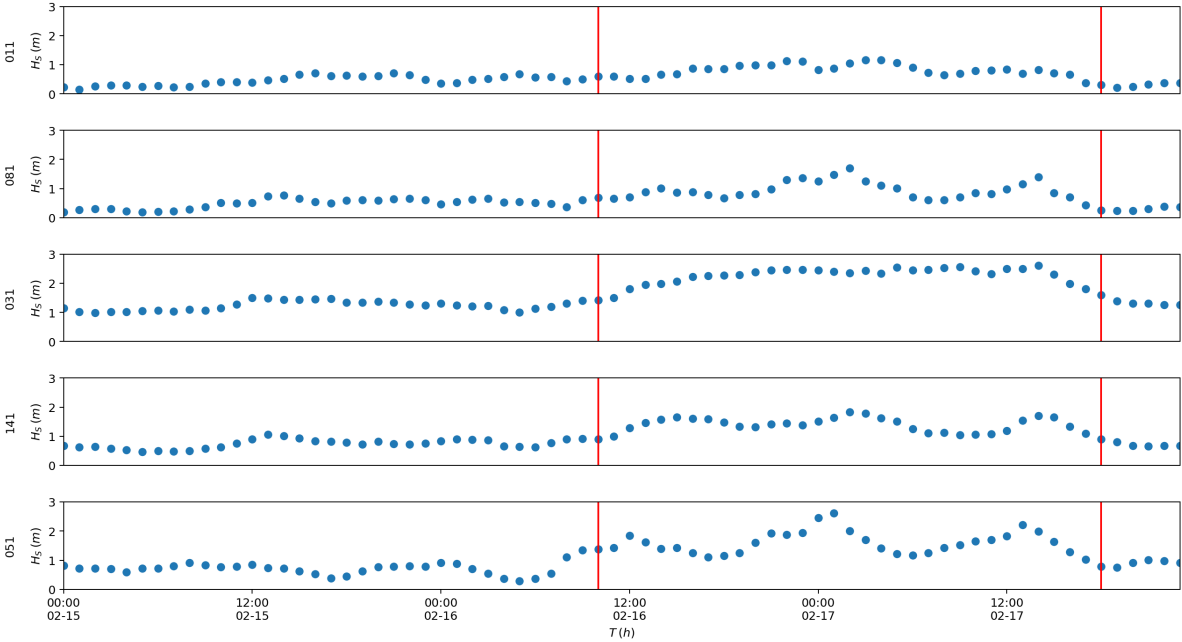


Figure A.2: Significant wave height plot during storm Dudley

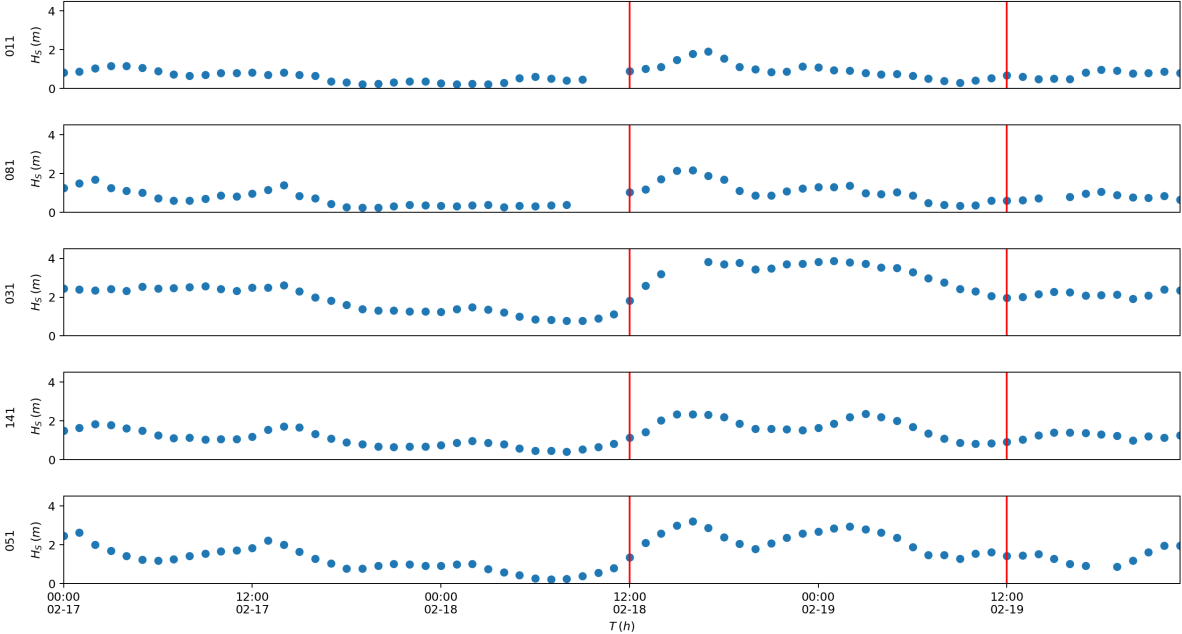


Figure A.3: Significant wave height plot during storm Eunice

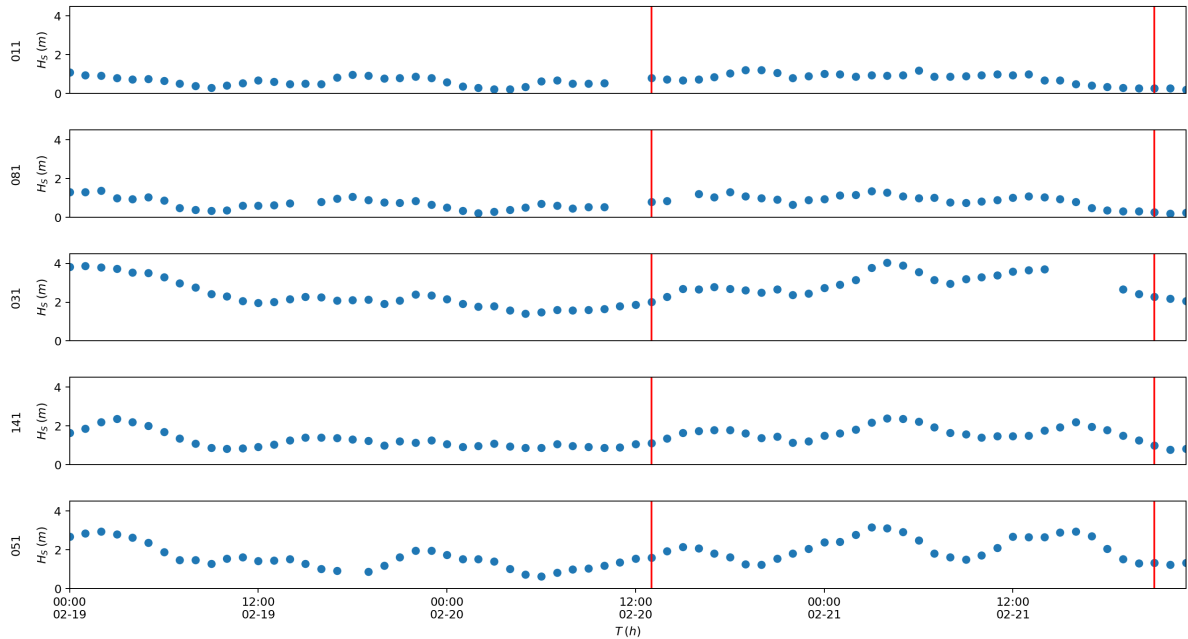


Figure A.4: Significant wave height plot during storm Franklin

A.2. Measurement errors

A.2.1. Corrie

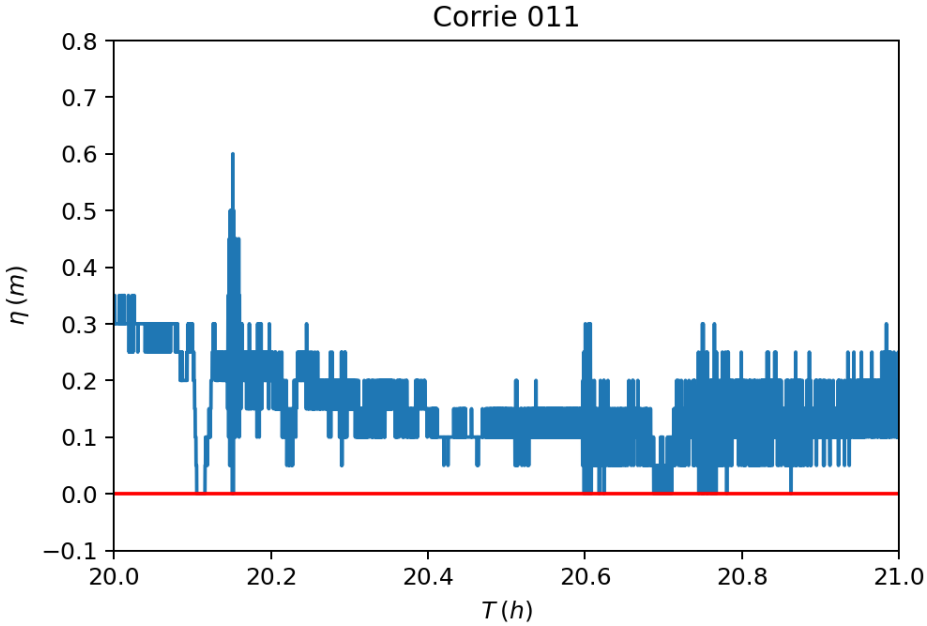


Figure A.5: Water level elevation during storm Corrie at 011 that are labeled as erroneous

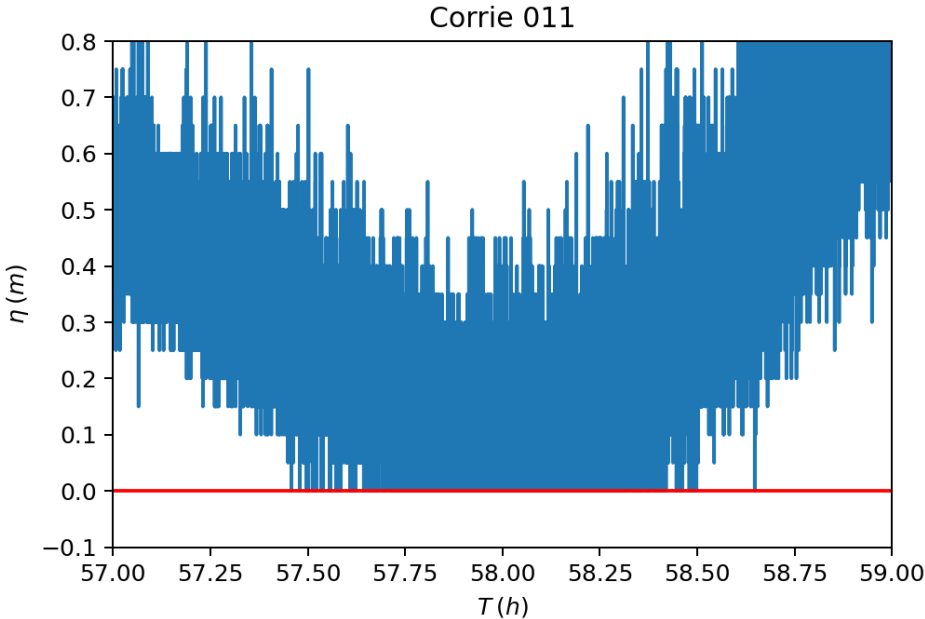


Figure A.6: Water level elevation during storm Corrie at 011 that are labeled as erroneous

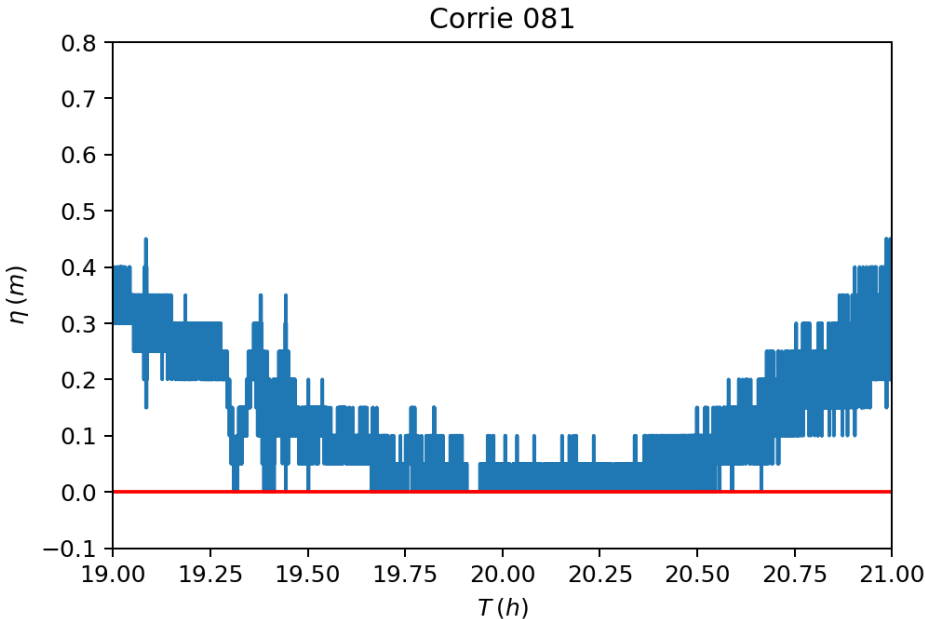


Figure A.7: Water level elevation during storm Corrie at 081 that are labeled as erroneous

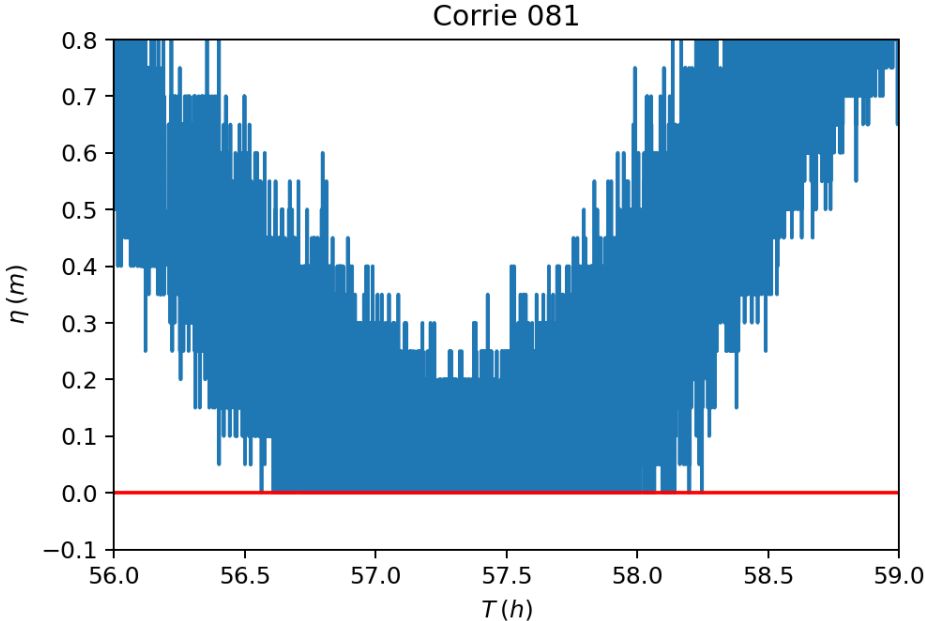


Figure A.8: Water level elevation during storm Corrie at 081 that are labeled as erroneous

A.2.2. Eunice

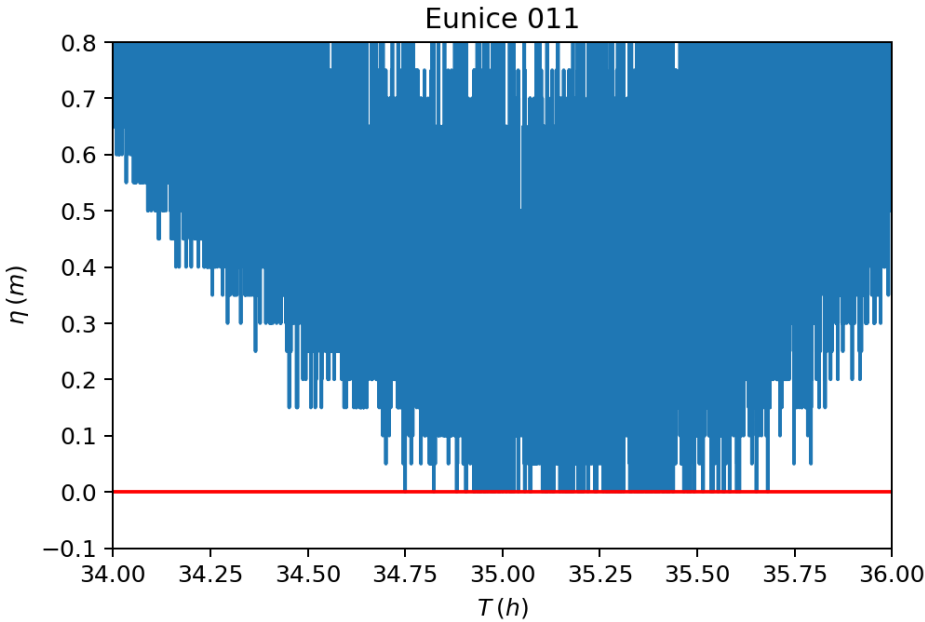


Figure A.9: Water level elevation during storm Eunice at 011 that are labeled as erroneous

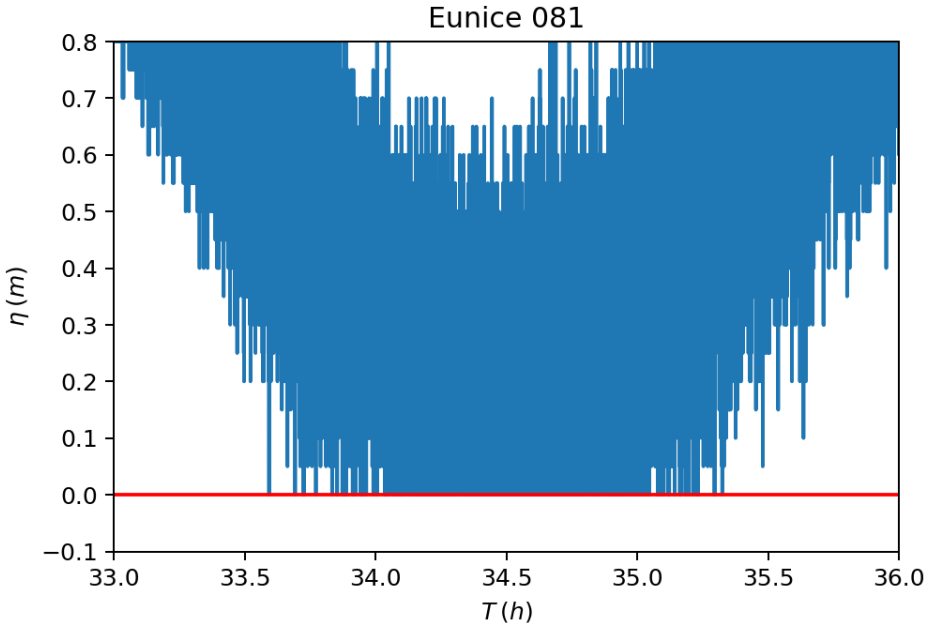


Figure A.10: Water level elevation during storm Eunice at 081 that are labeled as erroneous

A.2.3. Franklin

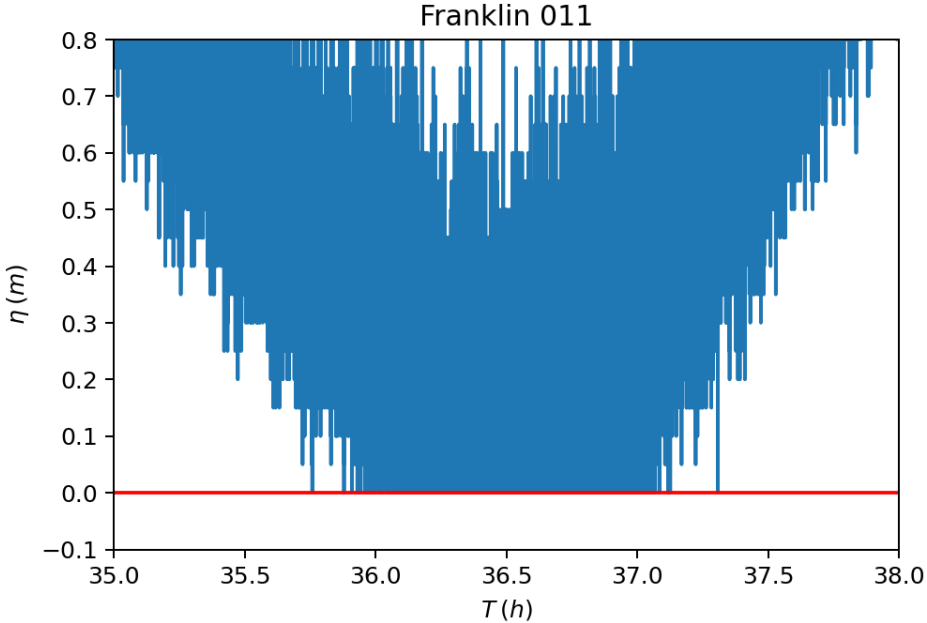


Figure A.11: Water level elevation during storm Franklin at 011 that are labeled as erroneous

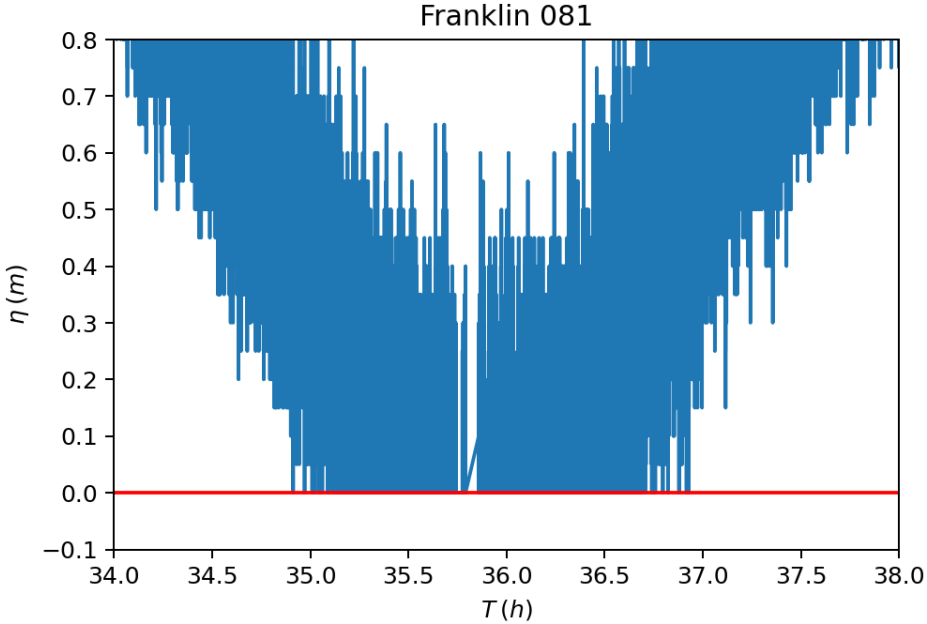


Figure A.12: Water level elevation during storm Franklin at 081 that are labeled as erroneous

B

Default SWAN file

```
1 $***** START-UP COMMANDS *****
2 PROJECT 'FIG_unst' 'RND'
3 SET NAUTICAL
4 MODE NONSTAT
5 COORDINATES SPHERICAL CCM
6
7 $***** COMPUTATIONAL GRID *****
8 CGRID UNSTRUCTURED CIRCLE 72 0.005 0.04
9 READ UNSTRUCTURED
10
11 $***** BATHYMETRY, CURRENT, WIND, HS, TM *****
12 INPGRID HSS REG -4 50 0 429 888 0.030303001 0.013511658 EXC -99.0 NONSTAT
13   ↳ 20220131.030000 1. HR 20220201.000000
14 READINP HSS 1 'Hm0_Corrie.inp' 3 0 FREE
15
16 INPGRID TSS REG -4 50 0 429 888 0.030303001 0.013511658 EXC -99.0 NONSTAT
17   ↳ 20220131.030000 1. HR 20220201.000000
18 READINP TSS 1 'Tm10_Corrie.inp' 3 0 FREE
19
20 $***** BOUNDARY CONDITIONS *****
21 include 'IGsource.inp'
22
23 $***** PHYSICS *****
24 FRIC JON 0.01
25 OFF QUAD
26 OFF BREA
27 OFF WCAP
28
29 $***** NUMERICAL PARAMETERS *****
30 PROP BSBT
31 NUM ACCUR NONSTAT mxitns=100
32
33 $***** OUTPUT REQUESTS *****
34 POINTS 'RIG' FILE 'NSP_IG.txt'
35 SPEC 'RIG' SPEC2D 'Corrie.spec2D' OUTP 20220131.040000 1. HR
36
37 $***** CLOSING COMMANDS *****
38 COMPUTE NONSTAT 20220131.030000 1. HR 20220201.000000
39 STOP
```

C

Number of Iterations

Performing a non-stationary results in the model using different boundary values for each iterative step. SWAN moves on to the next step if one of two conditions is met. The first condition to be met is an accuracy conditions, where the requirement is a sufficient accuracy in 99.5 % of the wet grid points. The second condition is based on the maximum number of iterations, given as an input in SWAN. Here, this value has been set to 100. The number of iterations for each iterative step can be seen in Table C.1.

	Hour																																		
Storm	1	2	3	4	5	6	7	8	9	10	11	12	13	14	15	16	17	18	19	20	21	22	23	24	25	26	27	28	29	30	31	32	33	34	
Corrie	0	22	5	4	4	4	3	3	3	3	3	3	3	3	3	3	3	3	3	3	3	3	3	3	3	3	3	3	3	3	3	3	3	3	3
Dudley	0	22	5	4	4	3	3	3	3	3	3	3	3	3	3	3	3	3	3	2	2	2	2	2	2	3	3	3	3	3	3	3	3	3	3
Emice	0	29	6	4	4	3	3	3	3	3	3	3	3	3	3	3	3	3	3	3	3	3	3	3	3	3	3	3	3	3	3	3	3	3	3
Franklin	0	22	6	4	4	3	3	3	3	3	3	3	3	3	3	3	3	3	3	3	3	3	3	3	3	3	3	3	3	3	3	3	3	3	3

Table C.1: Iterations required before the accuracy is sufficient in 99.5% of the wet grid points

D

Grid generation enhancements

D.1. Modification of the GSHHS data

The default version of the shapefile representing the coastline proved to be inaccurate. Figure D.1 shows the unmodified GSHHS shapefile. If inserted into Oceanmesh2D, it produces a grid where the measurement device at Hansweert is located on land. In reality, it is located at approximately 200 m from the crest of the dike. The coastlines near the measurement devices were modified using QGIS in such a way that it accurately represents the coastline near each measurement device. Figure D.2 provides the new configuration of the coastline near Hansweert. As the figure shows, it is now located in the Western Scheldt. Including the entry channel to the locks of Hansweert has been omitted for the sake of simplicity.

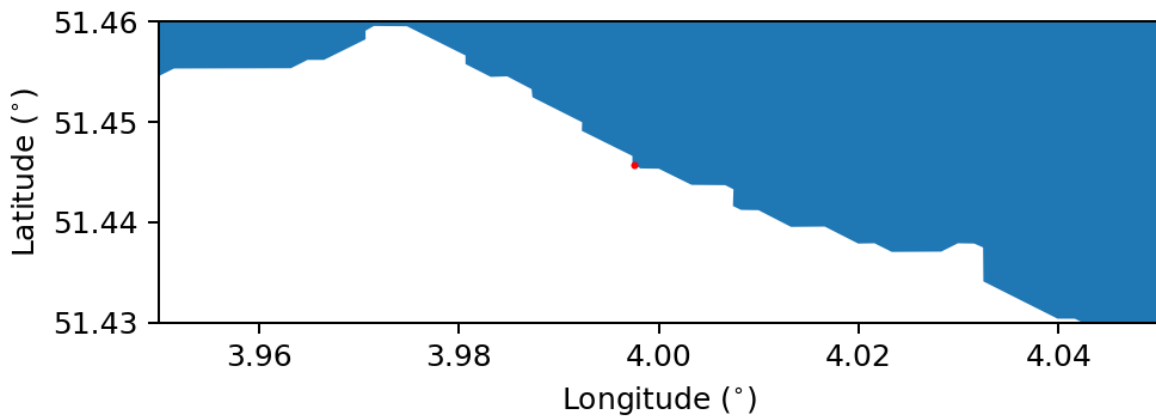


Figure D.1: Default GSHHS shapefile near Hansweert

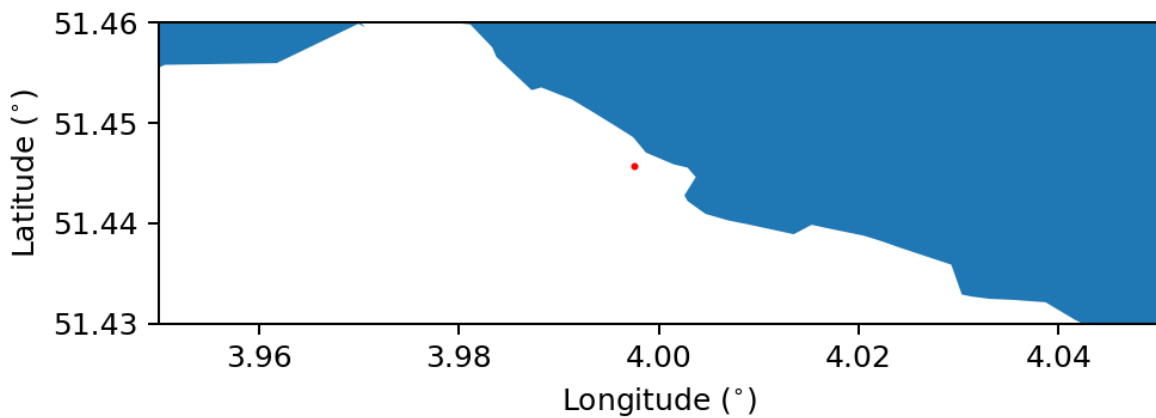


Figure D.2: Adapted GSHHS shapefile near Hansweert

D.2. Modifications on the EMODnet data

Figure D.3 shows the unstructured grid of the computational domain. Each dot represents a NaN value and this occurs 4819 times, all very close to the shoreline. This is a consequence of Oceanmesh2D defining a grid point based on the shapefile, but failing to match it with an elevation value from the bathymetry data. This mismatch can be seen in Figure D.4, where the black ellipsis envelops an area where bathymetry values are expected based on the shapefile. Another, perhaps more concerning, mismatch can be seen on the right side of Figure D.4. It appears that the EMODnet data does not reach far enough into the Western Scheldt, as data is missing. Unluckily, this is where the measurement device in Bath is located, which is depicted with an orange dot.

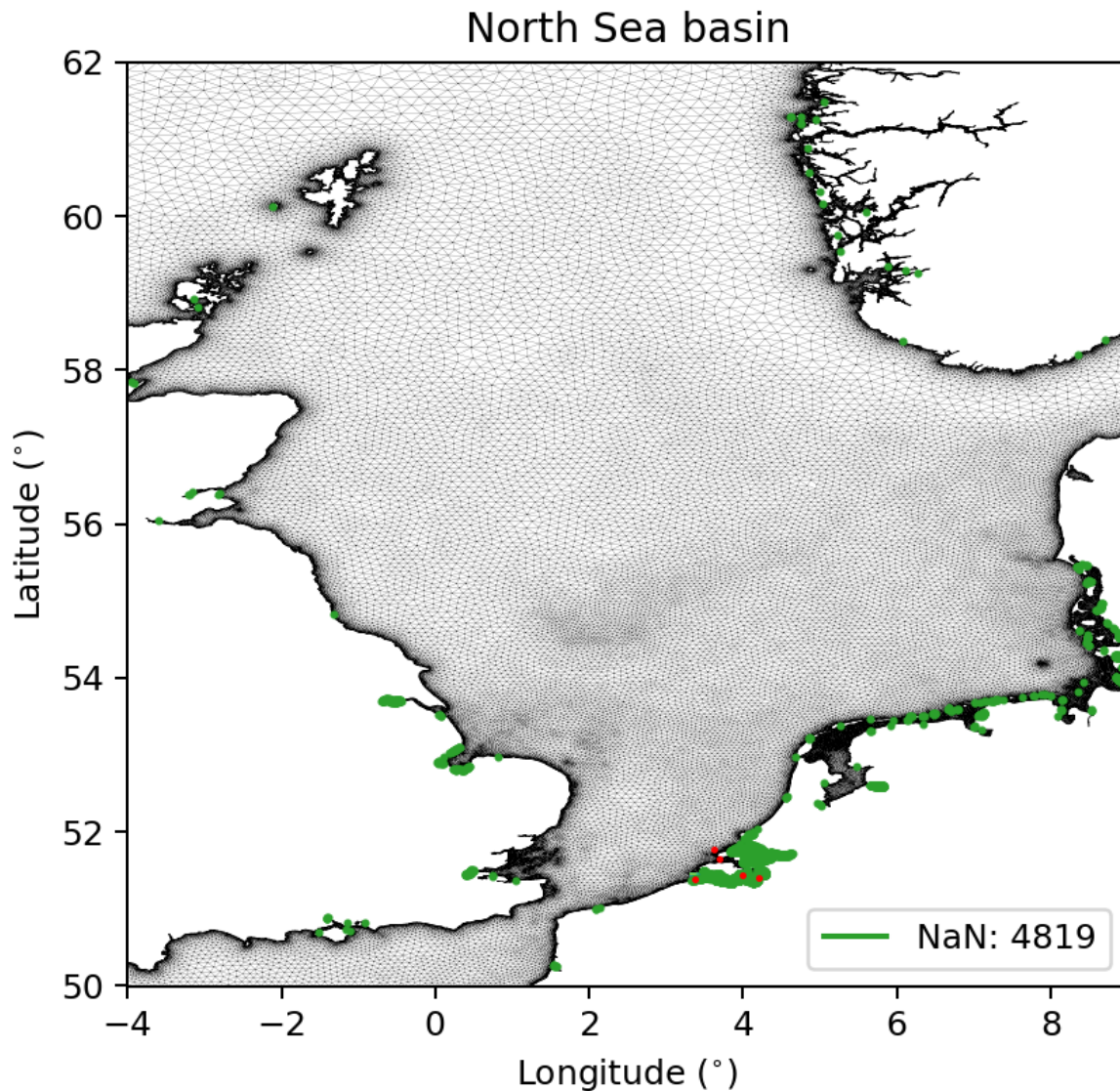


Figure D.3: North Sea basin with the Oceanmesh2D grid. Green values are marked grid points that are associated with NaN values in computational domain.

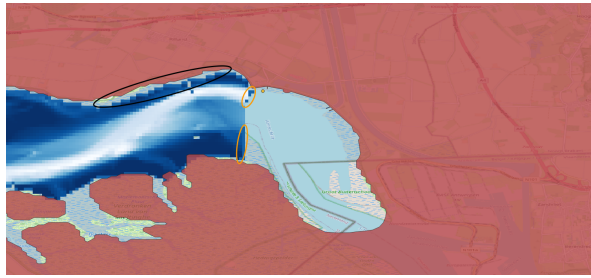


Figure D.4: Western Scheldt near Bath of EMODnet netCDF4 file prior to adaptations

This has been fixed with the use of another dataset, which describes the bathymetry in the Western Scheldt and is provided by Rijkswaterstaat. Python was used to transform the `ascii`-files of the Rijkswaterstaat dataset into a netCDF4 file, which was thereafter merged with the existing EMODnet dataset. A visual inspection concluded that there was a mismatch in the elevation values of the two netCDF4 files, which can be seen in Figure D.5. It proved that an additional 3.49 m on top of the elevation values of the Rijkswaterstaat data was required. This number is the mean of the the overlapping pixels which are deemed valid. Figure D.4 depicts two orange ellipses. The colors of the pixels insinuate a measurement error, as there would be a very large gradient in the bathymetry values if they were not. These values are ignored in the calculation of the additional 3.49 m. The final bathymetry can be found in Figure D.6. It should be noted that a small mismatch can still be present in the resulting bathymetry, with a step-like shift at the location of the seam.

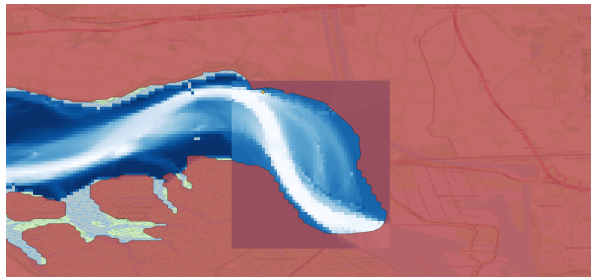


Figure D.5: Western Scheldt near Bath with a mismatch in bottom elevation

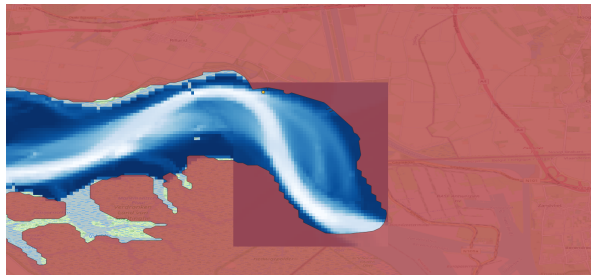


Figure D.6: Western Scheldt near Bath with a fixed bottom elevation transition

A considerable number of nodes along the coastlines of the computational domain contain NaN values. The average of the elevation values of surrounding nodes are used account for these missing values. Figure D.7 depicts a fictional situation and will be used for illustration. Here, the red node is the node with a non-existing elevation value. Its surrounding nodes have elevation values of 1 m, 1 m, 2 m, 2 m and NaN. The averaged value that will be assigned to the red node is 1.5 m. There are occurrences where all neighbouring nodes of a node with a NaN value, have NaN elevation values. In this case, the minimum elevation value of 0.5 m is assigned.

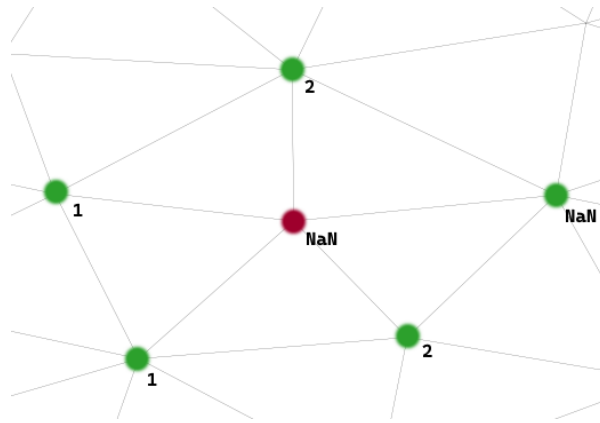


Figure D.7: A fictional location in a triangular grid

The biggest difference between these two methods lies within the step in the grid generation sequence where the modifications are done. The former is a modification on the netCDF4 data, thus the input data of Oceanmesh2D. The latter is a modification on the fort.14 file, thus the output of Oceanmesh2D. The biggest similarity between the two methods is that they are both used to deal with NaN values.

E

SWAN Assessment

E.1. Default

The plots below show a comparison of the FIG wave heights, obtained through bispectral analysis and the SWAN simulation without reflection lines.

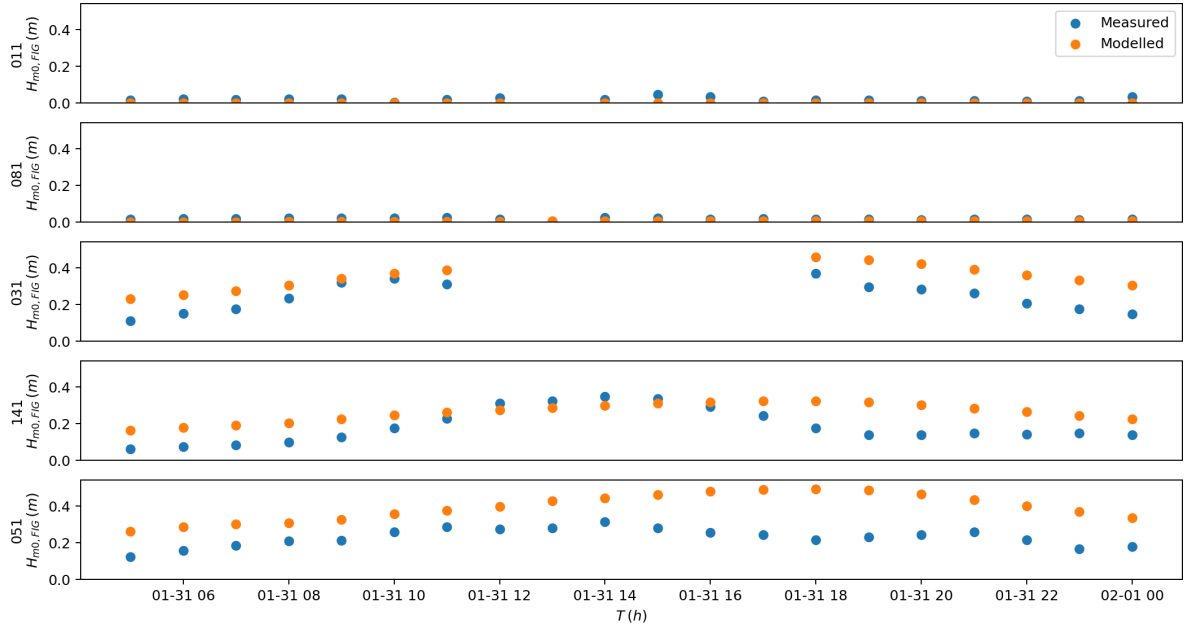


Figure E.1: Modelling and measuring results during storm Corrie

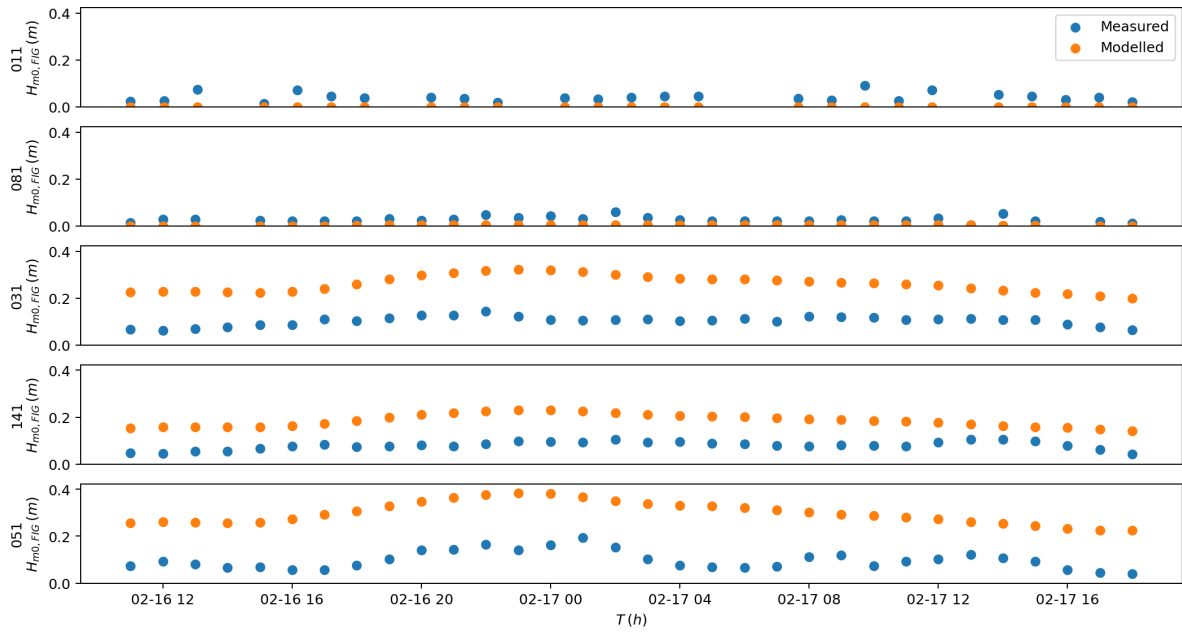


Figure E.2: Modelling and measuring results during storm Dudley

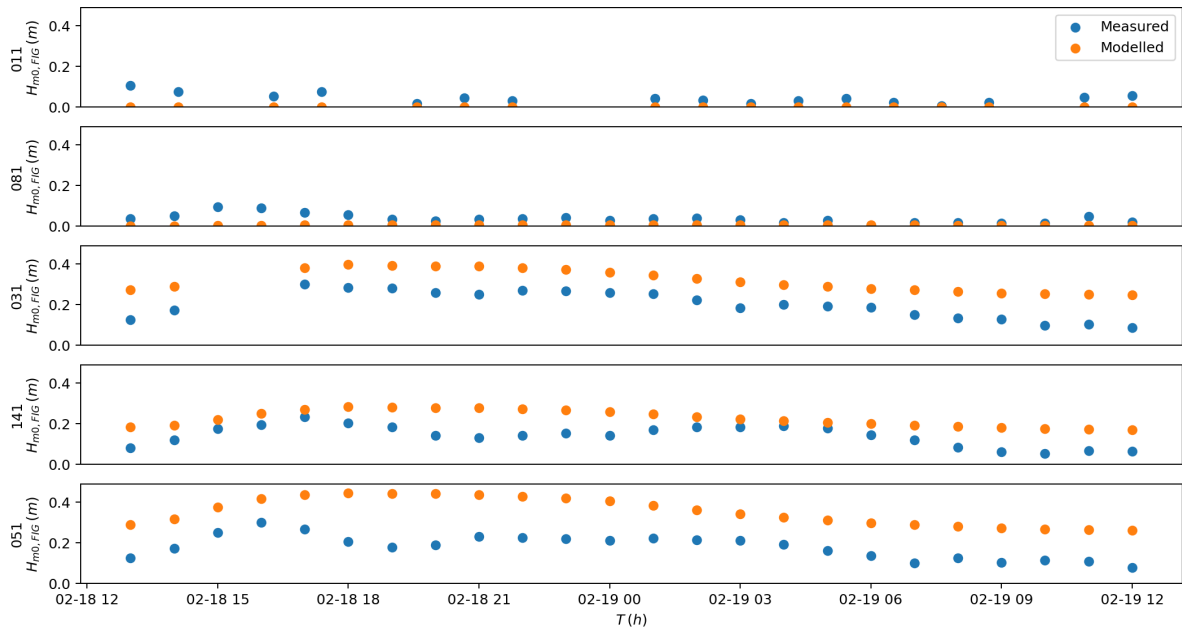


Figure E.3: Modelling and measuring results during storm Eunice

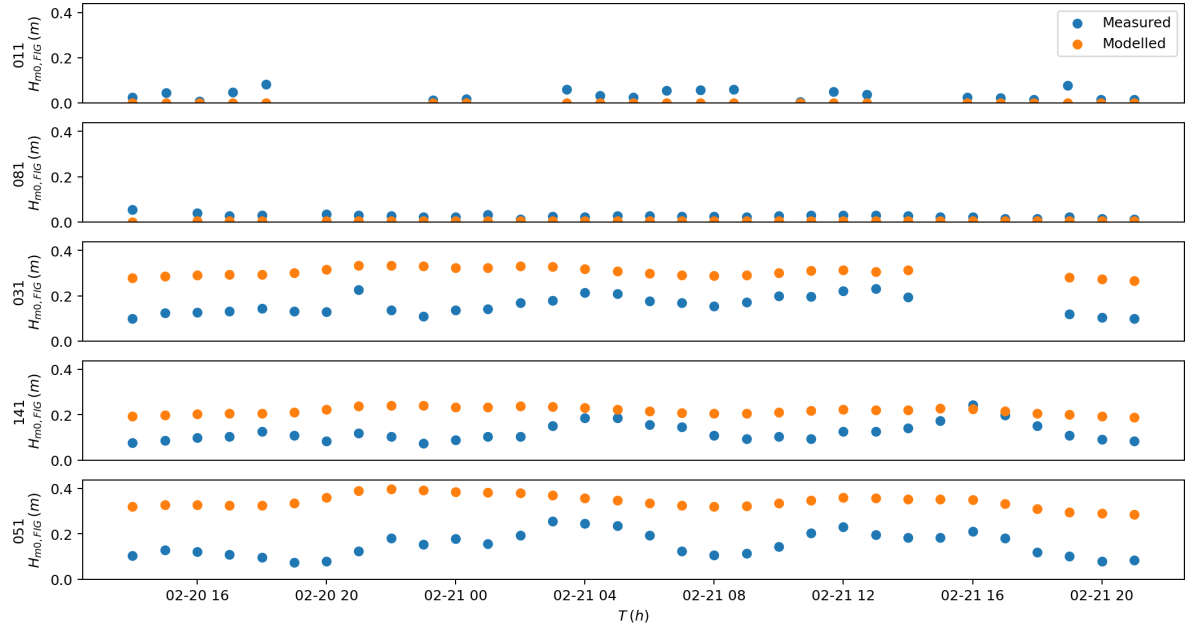


Figure E.4: Modelling and measuring results during storm Franklin

E.2. Comparison of the inclusion and exclusion of the reflective lines (Absolute)

To assess the effect of the reflection lines, two SWAN models were ran per storm. One of these models contains the reflection lines. As the difference proved to be small, the choice was made to plot the change between the two models according to Equation E.1, where the subscript implies whether the reflection lines is included or excluded.

These plots contain dots of different colors. A red dot means that the FIG wave height for both simulations was 0 m. An orange dot means that the simulation with with the reflective lines included leads to a nonzero FIG wave height, while the simulation without the reflective lines were 0 m. The green dots depict that both simulations registered a nonzero FIG wave height.

$$\Delta H_{m0,FIG} = H_{m0,FIG,Inc} - H_{m0,FIG,Exc} \quad (\text{E.1})$$

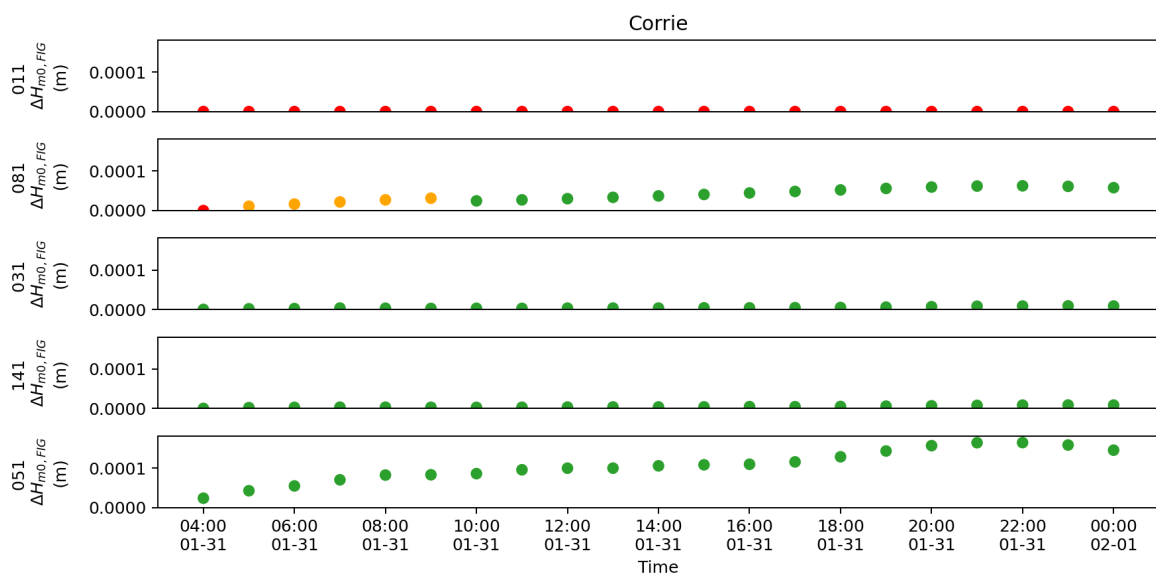


Figure E.5: Absolute difference between SWAN simulations including and excluding the reflection lines during storm Corrie

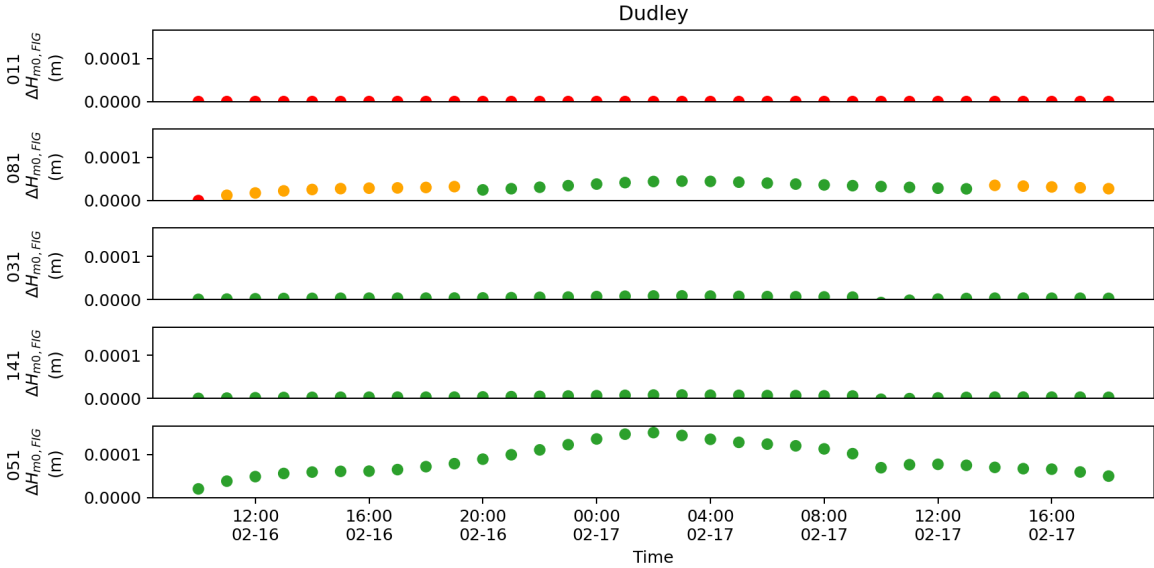


Figure E.6: Absolute difference between SWAN simulations including and excluding the reflection lines during storm Dudley

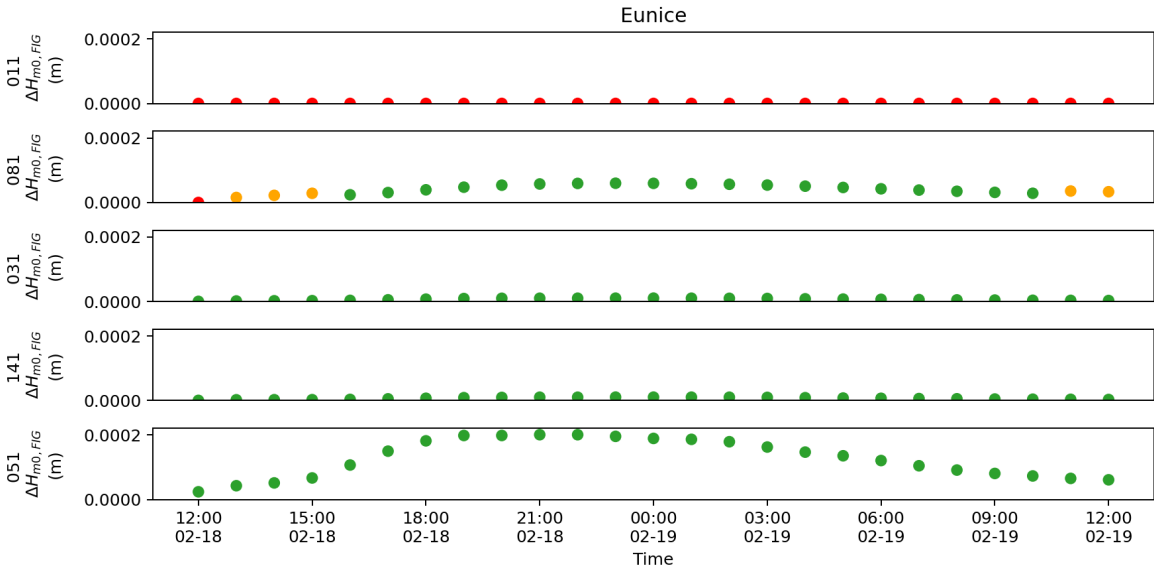


Figure E.7: Absolute difference between SWAN simulations including and excluding the reflection lines during storm Eunice

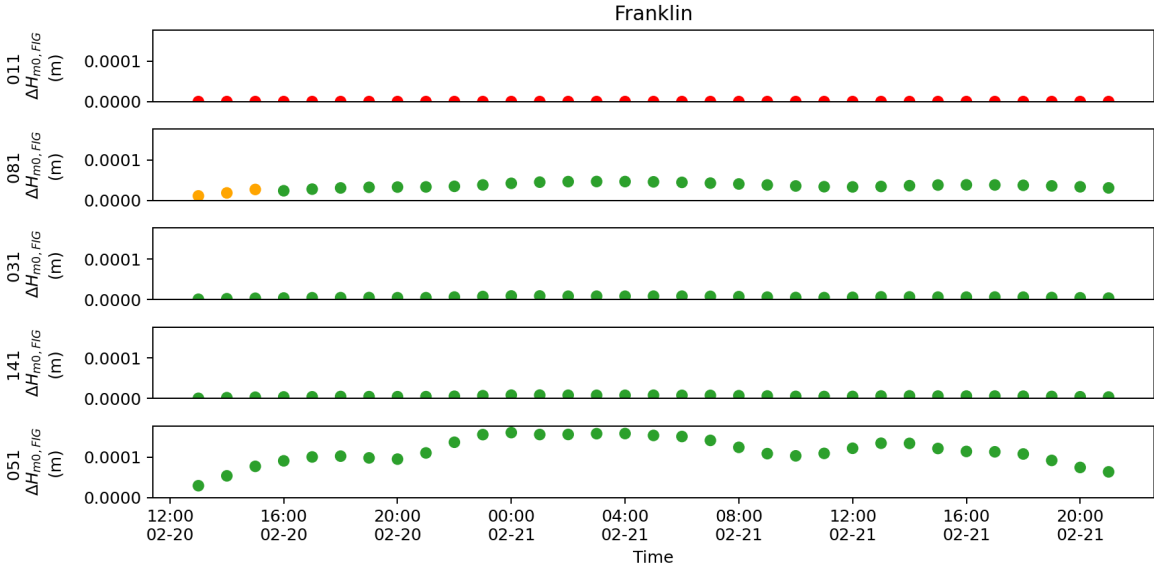


Figure E.8: Absolute difference between SWAN simulations including and excluding the reflection lines during storm Franklin

F

Western Scheldt Reflection Lines

This appendix contains the figures for all storms, with and without reflective lines along the Western Scheldt coast.

F.1. Corrie

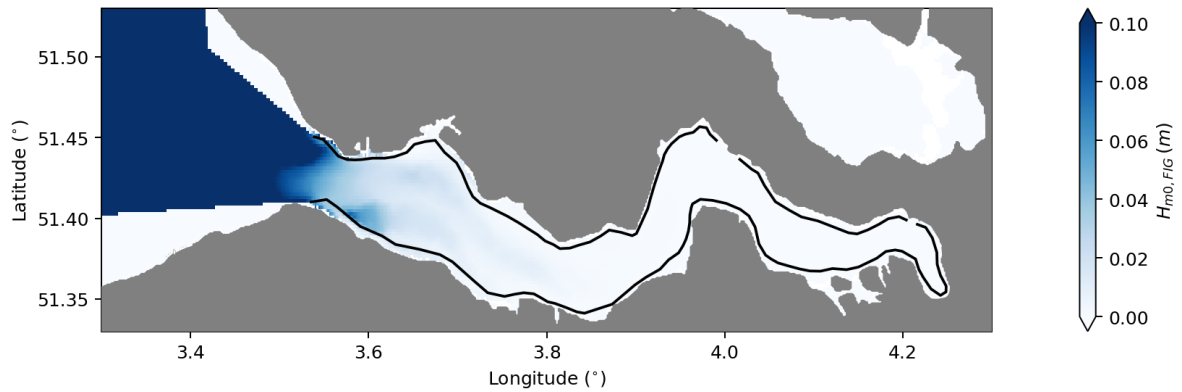


Figure F.1: Maximum $H_{m0,FIG}$ during storm Corrie without the reflective lines

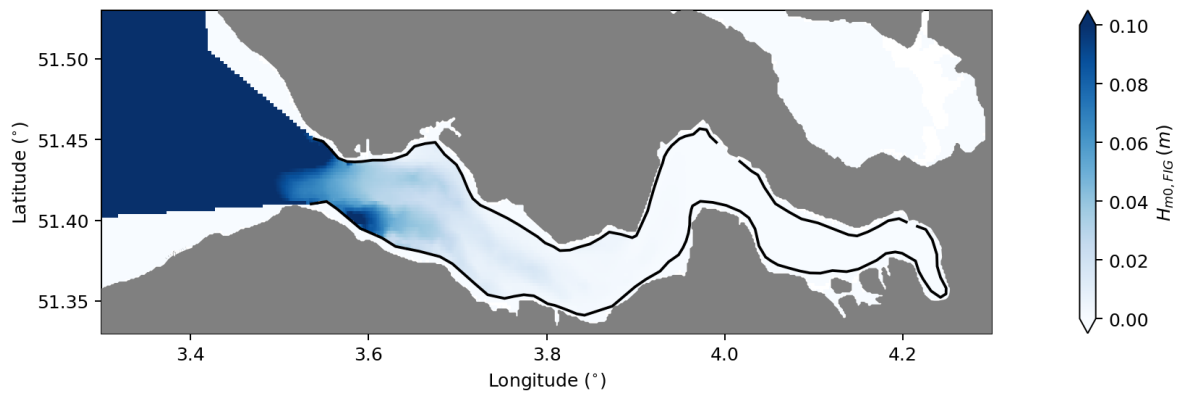


Figure F.2: Maximum $H_{m0,FIG}$ during storm Corrie with the reflective lines

F.2. Dudley

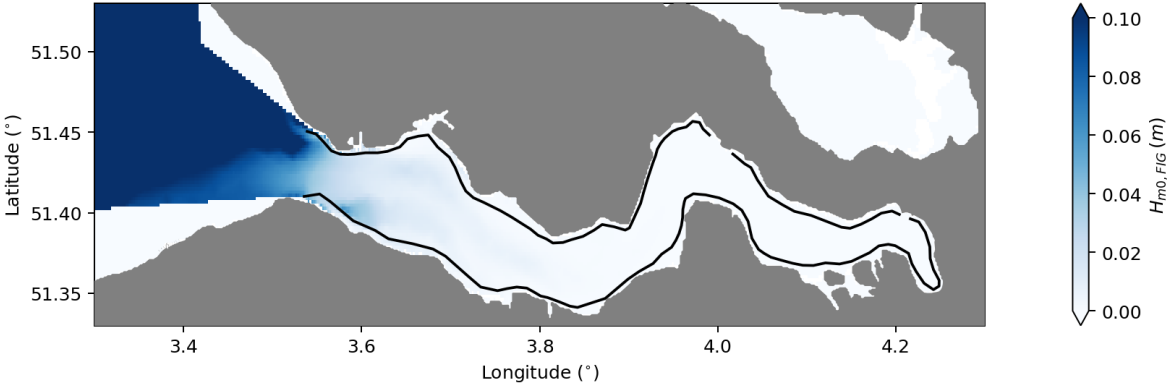


Figure F.3: Maximum $H_{m0,FIG}$ during storm Dudley without the reflective lines

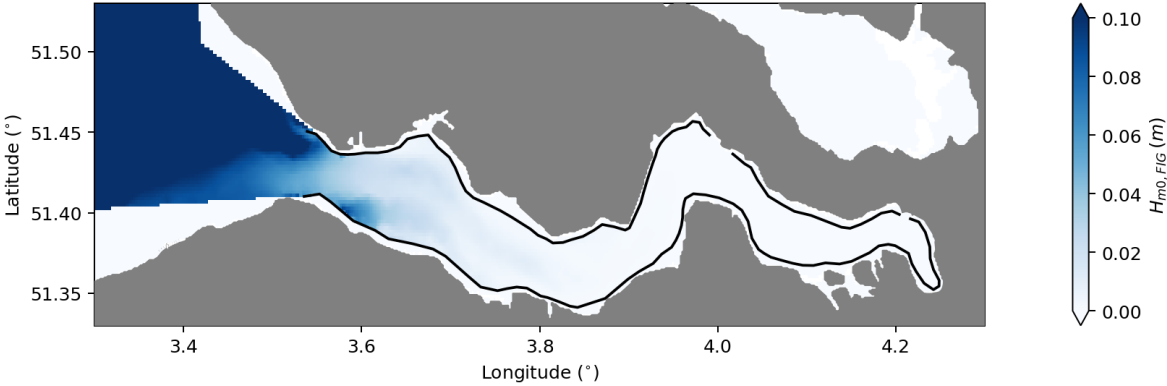


Figure F.4: Maximum $H_{m0,FIG}$ during storm Dudley with the reflective lines

F.3. Eunice

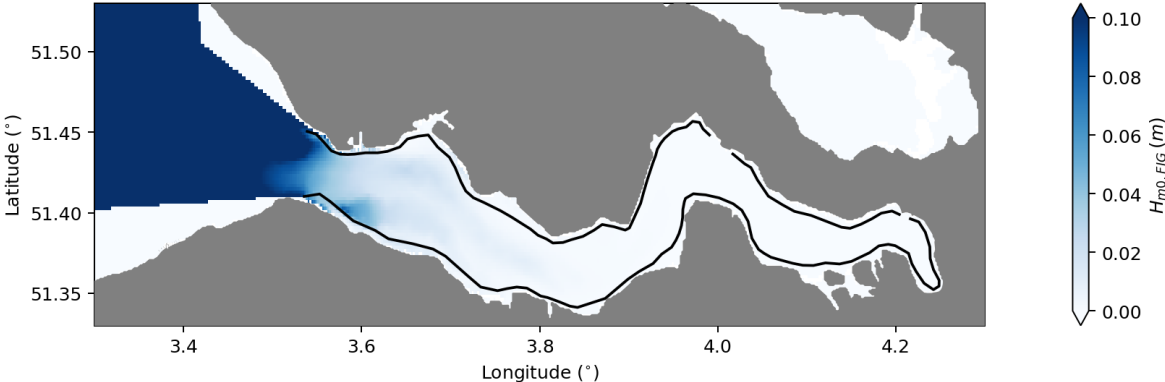


Figure F.5: Maximum $H_{m0,FIG}$ during storm Eunice without the reflective lines

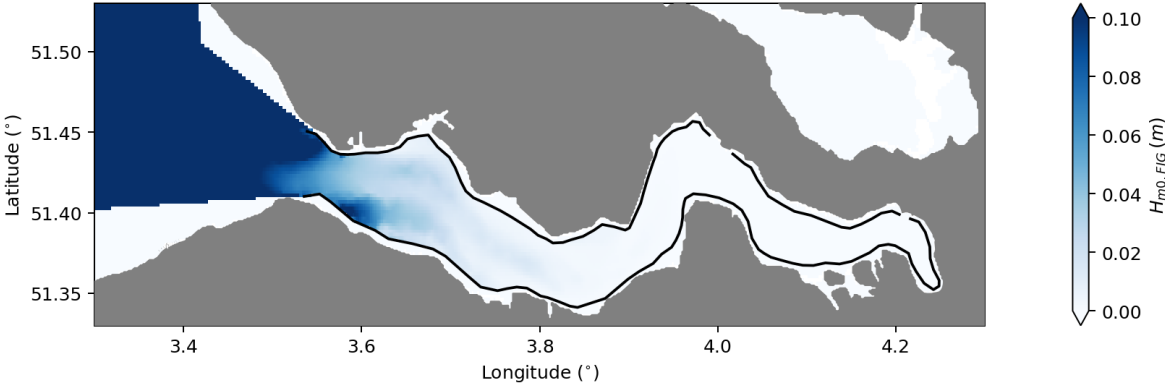


Figure F.6: Maximum $H_{m0,FIG}$ during storm Eunice with the reflective lines

F.4. Franklin

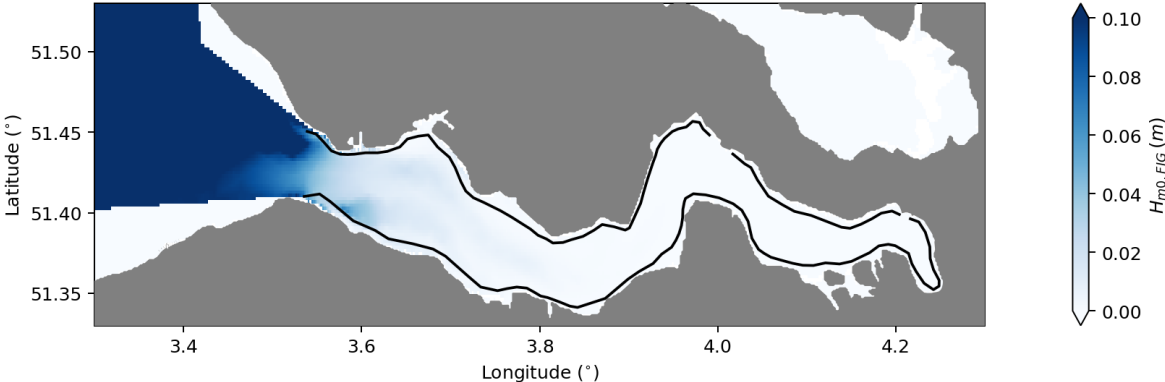


Figure F.7: Maximum $H_{m0,FIG}$ during storm Franklin without the reflective lines

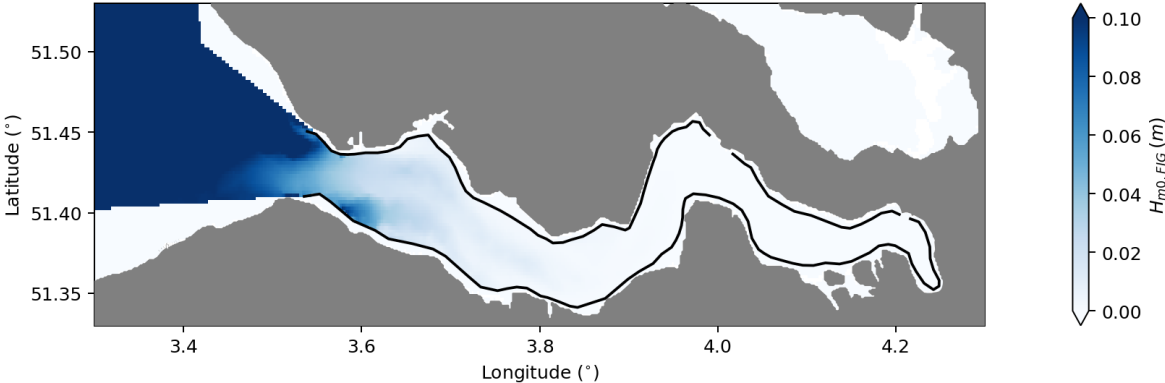


Figure F.8: Maximum $H_{m0,FIG}$ during storm Franklin with the reflective lines

References

- Ardhuin, Fabrice, Arshad Rawat, and Jerome Aucan (May 2014). “A numerical model for free infragravity waves: Definition and validation at regional and global scales”. In: *Ocean Modelling* 77, pp. 20–32. DOI: 10.1016/j.ocemod.2014.02.006. URL: <https://doi.org/10.1016/j.ocemod.2014.02.006>.
- Bertin, Xavier and Maitane Olabarrieta (Aug. 2016). “Relevance of infragravity waves in a wave-dominated inlet”. In: *Journal of Geophysical Research: Oceans* 121.8, pp. 5418–5435. DOI: 10.1002/2015jc011444. URL: <https://doi.org/10.1002/2015jc011444>.
- Bertin, Xavier et al. (2018). “Infragravity waves: From driving mechanisms to impacts”. In: *Earth-Science Reviews* 177, pp. 774–799. ISSN: 0012-8252. DOI: <https://doi.org/10.1016/j.earscirev.2018.01.002>. URL: <https://www.sciencedirect.com/science/article/pii/S0012825217303239>.
- Bosboom, Judith and Marcel J.F. Stive (2023). *Coastal Dynamics*. 1.2. Delft: TU Delft Open. DOI: 10.5074/T.2021.001.
- Bradshaw, Mark P. (Mar. 1980). “Topographic Control of Run-Up Variability”. In: *Coastal Engineering 1980*. American Society of Civil Engineers. DOI: 10.1061/9780872622647.067. URL: <https://doi.org/10.1061/9780872622647.067>.
- de Bakker, A T M, M F S Tissier, and B G Ruessink (Jan. 2016). “Beach steepness effects on nonlinear infragravity-wave interactions: A numerical study”. en. In: *J. Geophys. Res. Oceans* 121.1, pp. 554–570.
- (Jan. 2014). “Shoreline dissipation of infragravity waves”. In: *Continental Shelf Research* 72, pp. 73–82. DOI: 10.1016/j.csr.2013.11.013. URL: <https://doi.org/10.1016/j.csr.2013.11.013>.
- EMODnet Bathymetry Consortium (2018). *EMODnet Digital Bathymetry (DTM 2018)*. DOI: 10.12770/18FF0D48-B203-4A65-94A9-5FD8B0EC35F6. URL: <https://sextant.ifremer.fr/record/18ff0d48-b203-4a65-94a9-5fd8b0ec35f6/>.
- European Union-Copernicus Marine Service (2019). *Atlantic - European North West Shelf - Ocean Wave Analysis and Forecast*. en. DOI: 10.48670/MOI-00055. URL: https://data.marine.copernicus.eu/product/NWSHELF_ANALYSISFORECAST_WAV_004_014/description.
- Hasselmann, K. (1962). “On the non-linear energy transfer in a gravity-wave spectrum Part 1. General theory”. In: *Journal of Fluid Mechanics* 12.4, pp. 481–500. DOI: 10.1017/S0022112062000373. URL: <https://doi.org/10.1017/S0022112062000373>.
- Herbers, T. H. C., Steve Elgar, and R. T. Guza (May 1994). “Infragravity-Frequency (0.005–0.05 Hz) Motions on the Shelf. Part I: Forced Waves”. In: *Journal of Physical Oceanography* 24.5, pp. 917–927. DOI: 10.1175/1520-0485(1994)024<0917:ifhmot>2.0.co;2. URL: [https://doi.org/10.1175/1520-0485\(1994\)024%3C0917:ifhmot%3E2.0.co;2](https://doi.org/10.1175/1520-0485(1994)024%3C0917:ifhmot%3E2.0.co;2).
- (Dec. 1995). “Generation and propagation of infragravity waves”. In: *Journal of Geophysical Research: Oceans* 100.C12, pp. 24863–24872. DOI: 10.1029/95jc02680. URL: <https://doi.org/10.1029/95jc02680>.
- Holthuijsen, Leo H. (Jan. 2007). *Waves in Oceanic and Coastal Waters*. Cambridge University Press. ISBN: 9780521129954. DOI: 10.1017/cbo9780511618536. URL: <http://dx.doi.org/10.1017/CB09780511618536>.
- Inch, Kris et al. (Apr. 2017). “Observations of nearshore infragravity wave dynamics under high energy swell and wind-wave conditions”. In: *Continental Shelf Research* 138, pp. 19–31. DOI: 10.1016/j.csr.2017.02.010. URL: <https://doi.org/10.1016/j.csr.2017.02.010>.
- Jacobusse, C. and M. Decler (2003). *Het Verdronken Land van Saeftinghe en de Westerschelde*. Leuven: Davidsfonds/De Koperen Tuin, p. 100. ISBN: ISBN 90-807995-1-3.
- Kuijper, K. (2013). *Instandhouding vaarpassen Schelde Milieuvergunningen terugstorten baggerspecie*.
- Kuipers, J.J.B. et al. (2004). *Sluimerend in Slik*. Den Boer / De Ruiter.
- Longuet-Higgins, M. S. and R. W. Stewart (1960). “Changes in the form of short gravity waves on long waves and tidal currents”. In: *Journal of Fluid Mechanics* 8.4, pp. 565–583. DOI: 10.1017/S0022112060000803.
- (1962). “Radiation stress and mass transport in gravity waves, with application to ‘surf beats’”. In: *Journal of Fluid Mechanics* 13, pp. 481–504.

- Naporowski, R. (2020). *Long waves in the North Sea: Distribution, generation and measurement methods*.
- Plouvier, Noé (2022). *The influence of infra-gravity waves on dike overtopping for shallow foreshores*.
- Pomeroy, Andrew W M et al. (Apr. 2015). “Spectral wave-driven sediment transport across a fringing reef”. en. In: *Coast. Eng.* 98, pp. 78–94.
- Reniers, A. J. H. M. et al. (Oct. 2002). “Linear modeling of infragravity waves during Delilah”. In: *Journal of Geophysical Research: Oceans* 107.C10. DOI: 10.1029/2001jc001083. URL: <https://doi.org/10.1029/2001jc001083>.
- Reniers, Ad J.H.M. et al. (Jan. 2021). “North Sea Infragravity Wave Observations”. In: *Journal of Marine Science and Engineering* 9.2, p. 141. ISSN: 2077-1312. DOI: 10.3390/jmse9020141. URL: <http://dx.doi.org/10.3390/jmse9020141>.
- Roberts, Keith J., William J. Pringle, and Joannes J. Westerink (May 2019). “OceanMesh2D 1.0: MATLAB-based software for two-dimensional unstructured mesh generation in coastal ocean modeling”. In: *Geoscientific Model Development* 12.5, pp. 1847–1868. ISSN: 1991-9603. DOI: 10.5194/gmd-12-1847-2019. URL: <http://dx.doi.org/10.5194/gmd-12-1847-2019>.
- Roelvink, Dano et al. (Nov. 2009). “Modelling storm impacts on beaches, dunes and barrier islands”. In: *Coastal Engineering* 56.11–12, pp. 1133–1152. ISSN: 0378-3839. DOI: 10.1016/j.coastaleng.2009.08.006. URL: <http://dx.doi.org/10.1016/j.coastaleng.2009.08.006>.
- Smits, S. B. M. (2023). *The influence of infragravity waves on wave runup against dikes during storms*.
- Symonds, G., David Huntley, and Anthony Bowen (Jan. 1982). “Two-Dimensional Surf Beat: Long Wave Generation by a Time-Varying Breakpoint”. In: *Journal of Geophysical Research* 87, pp. 492–498. DOI: 10.1029/JC087iC01p00492.
- TAW (2002). *Technical Report Wave Run-up and Wave Overtopping at Dikes*. Tech. rep. Technical Advisory Committee on Flood Defence.
- The SWAN Team (2023). *SWAN USER MANUAL*.
- van Dijk, W. M. et al. (Jan. 2019). “Effects of Shoal Margin Collapses on the Morphodynamics of a Sandy Estuary”. In: *Journal of Geophysical Research: Earth Surface* 124.1, pp. 195–215. DOI: 10.1029/2018jf004763. URL: <https://doi.org/10.1029/2018jf004763>.
- van Dongeren, A et al. (Feb. 2007a). “Shoaling and shoreline dissipation of low-frequency waves”. en. In: *J. Geophys. Res.* 112.C2.
- (Feb. 2007b). “Shoaling and shoreline dissipation of low-frequency waves”. In: *Journal of Geophysical Research* 112.C2. DOI: 10.1029/2006jc003701. URL: <https://doi.org/10.1029/2006jc003701>.
- Vrećica, T, R Soffer, and Y Toledo (Aug. 2019). “Infragravity wave generation by wind gusts”. en. In: *Geophys. Res. Lett.* 46.16, pp. 9728–9738.
- Weisscher, Steven A.H. et al. (Dec. 2022). “Transitional polders along estuaries: Driving land-level rise and reducing flood propagation”. In: *Nature-Based Solutions* 2, p. 100022. DOI: 10.1016/j.nbsj.2022.100022. URL: <https://doi.org/10.1016/j.nbsj.2022.100022>.
- Wessel, Pál and Walter H. F. Smith (Apr. 1996). “A global, self-consistent, hierarchical, high-resolution shoreline database”. In: *Journal of Geophysical Research: Solid Earth* 101.B4, pp. 8741–8743. ISSN: 0148-0227. DOI: 10.1029/96jb00104. URL: <http://dx.doi.org/10.1029/96JB00104>.
- Zijderveld, A. et al. (2022a). *Stormvloedrapport SR100*. Tech. rep. Rijkswaterstaat.
- Zijderveld, A. et al. (2022b). *Stormvloedrapport SR99*. Tech. rep. Rijkswaterstaat.